Atomic-level structure determination of organic assemblies by dynamic nuclear polarization enhanced solid-state NMR

Katharina Märker

To cite this version:

Katharina Märker. Atomic-level structure determination of organic assemblies by dynamic nuclear polarization enhanced solid-state NMR. Physics [physics]. Université Grenoble Alpes, 2017. English. NNT : 2017GREAV082 . tel-01961480

HAL Id: tel-01961480
https://theses.hal.science/tel-01961480v1

Submitted on 20 Dec 2018

Communauté
UNIVERSITÉ Grenoble Alpes

THÈSE

Pour obtenir le grade de

DOCTEUR DE LA COMMUNAUTE UNIVERSITE GRENOBLE ALPES

Spécialité : **Chimie Physique Moléculaire et Structurale**

Arrêté ministériel : 25 mai 2016

Présentée par

Katharina MÄRKER

Thèse dirigée par **Gaël DE PAEPE**, **Jean-Marie MOUESCA** et **Sabine HEDIGER**

préparée au sein du **Laboratoire Modélisation et Exploration des Matériaux**
dans **l'École Doctorale Chimie et Science du Vivant**

Détermination structurale de systèmes organiques par polarisation dynamique nucléaire et RMN solide

Atomic-level structure determination of organic assemblies by dynamic nuclear polarization enhanced solid-state NMR

Thèse soutenue publiquement le **19 décembre 2017**
devant le jury composé de :

Dr Dominique MASSIOT
Directeur de Recherche, CEMHTI-CNRS UPR3079, Président
Dr Paul HODGKINSON
Reader, Durham University (UK), Rapporteur
Dr Thibault CHARPENTIER
Chercheur CEA, IRAMIS/NIMBE, CEA Saclay, Rapporteur
Pr Christian BONHOMME
Professeur, LCMCP, UPMC-Paris 6, Examinateur
Dr Paul SCHANDA
Chercheur CEA, IBS, CEA Grenoble, Examinateur
Dr Laurent HEUX
Directeur de Recherche, CERMAV-CNRS, Examinateur

Acknowledgements

I spent over three exciting years in Grenoble in which I learnt a lot about NMR and truly enjoyed doing interesting science as well as exploring amazing places in the mountains. I will keep great memories of this time and am very grateful to the people without whom this would not have been possible.

First of all, I would like to thank my advisors, Gaël De Paëpe, Jean-Marie Mouesca, and Sabine Hediger. They gave me the freedom to follow my interests and tackle problems the way I like, while always being available for helpful and inspiring discussions. I greatly appreciate the freedom and trust I have been given, and all that I was able to learn from them.

Moreover, I want to thank Paul Hodgkinson and Thibault Charpentier for agreeing to be “rapporteurs” for this thesis, as well as Dominique Massiot, Christian Bonhomme, Paul Schanda, and Laurent Heux for accepting to be members of my PhD jury. I am looking forward to their feedback and interesting discussions.

I thank Daniel Lee for teaching me the practical aspects of solid-state NMR and DNP and how to make things work. I am also grateful to him for many interesting discussions and for always creating a positive atmosphere in the lab.

Several other people have made important contributions to this work for which I want to thank them: Subhradip Paul has worked hard on the acquisition and analysis of the carbon-carbon 2D experiments on cyclo-FF. Jean-Marie Mouesca has written a Fortran code for structure determination. Morgane Pingret and Didier Gasparutto synthesized several guanosine derivatives for us, Carlos Fernández-de-Alba has prepared the cyclo-FF sample used in this thesis, and Sachin Chaudhari prepared the ampicillin sample. I also acknowledge Bruker Biospin for giving us measurement time in Wissembourg, and Fabien Aussenac for his support there.

I thank all other colleagues I’ve had over the time: Nghia Tuan Duong, Subhradip Paul, Fred Mentink-Vigier, Carlos Fernández-de-Alba, Adam Smith, Ildefonso Marin-Montesinos, and Sachin Chaudhari. Coffee break discussions from serious

science to absurd Friday topics were always a joy.

Last but not least, I want to thank some special people: Jvles for spending the last three years flooding my apartment with postcards and visiting Grenoble many times, without even liking mountains or cheese. Paul for filling my life with happiness, laughter and so many weird ideas. And of course my parents for their constant support and belief in me.

Abstract

Supramolecular structure determination of organic solids is of utter importance for understanding their properties and function. Structural insights at the atomic level can be provided by magic-angle spinning (MAS) solid-state nuclear magnetic resonance (NMR) spectroscopy. However, this technique faces strong limitations in sensitivity due to the low natural isotopic abundance (NA) of the key nuclei ^{13}C and ^{15}N (1.1 % and 0.37 %, respectively). Sensitivity enhancement by several orders of magnitude can be achieved with dynamic nuclear polarization (DNP) which is based on polarization transfer from electron to nuclear spins. The recent progress in the practical implementation of DNP opens up new and exciting possibilities for structure determination of organic solids which are explored in this thesis.

The first step for structural studies with NMR is resonance assignment. The complete assignment of ^{13}C and ^{15}N resonances at NA is demonstrated here to be feasible based on DNP-enhanced $^{13}\text{C}-^{13}\text{C}$ and, for the first time, $^{13}\text{C}-^{15}\text{N}$ correlation spectra.

The focus is then laid on obtaining structural information in the form of carbon-carbon and carbon-nitrogen distances from the buildup of polarization in dipolar recoupling experiments. Several strategies are discussed for recording such polarization buildup curves at NA. A decisive advantage of these measurements is that dipolar truncation is reduced to a great extent, enabling undisturbed polarization transfer over long distances and a simple description of the spin dynamics by numerical simulations. This is demonstrated experimentally on the self-assembled cyclic diphenylalanine peptide (cyclo-FF). The $^{13}\text{C}-^{13}\text{C}$ and $^{13}\text{C}-^{15}\text{N}$ buildup curves obtained are indeed sensitive to long distances (up to ≈ 7 Å) and are in excellent agreement with the crystal structure of cyclo-FF. Moreover, each buildup curve represents a superposition of multiple intra- and intermolecular distance contributions and can therefore provide a wealth of structural information.

It is subsequently shown that the high information content and the simple theoretical description of such polarization buildup curves enables determination of both the molecular and the supramolecular structure of cyclo-FF. This is achieved with the help of a dedicated computational code which creates structural models based on a systematic grid-search and ranks them according to their agreement with the experimental data.

The thesis concludes by presenting improvements for the homonuclear dipolar recoupling pulse sequence SR26 which is a powerful sequence for use in NA samples. These improvements enable increased recoupling efficiency and the acquisition of 2D correlation spectra with large spectral widths.

Overall, this thesis demonstrates that clear advantages lie in the use of NA samples for structural studies of organic solids, and that MAS-DNP enables structure determination which is mainly based on distance information from NMR data.

Résumé

La détermination structurale supramoléculaire de solides organiques est d'une importance capitale pour la compréhension de leurs propriétés et de leur fonction. Des informations structurales à l'échelle atomique peuvent en principe être obtenues pour des composés en phase solide par la spectroscopie RMN (résonance magnétique nucléaire) combinée à la rotation de l'échantillon à l'angle magique (MAS). Cette technique est cependant confrontée à de fortes limitations de sensibilité, notamment en raison de la faible abondance isotopique naturelle (AN) d'isotopes clés, comme le carbone-13 et l'azote-15 (respectivement 1.1 % et 0,37 %).

Une amplification de la sensibilité de plusieurs ordres de grandeur peut être obtenue avec la polarisation nucléaire dynamique (DNP), technique basée sur le transfert de polarisation des spins électroniques aux spins nucléaires. Les progrès récents dans la mise en œuvre pratique de la DNP ouvrent de nouvelles voies passionnantes, explorées dans cette thèse, pour la détermination de la structure des solides organiques.

La première étape d'une étude structurale par RMN consiste en l'attribution spectrale des résonances. Malgré la faible AN des isotopes ^{13}C et ^{15}N nous montrons dans ce travail que l'attribution complète de ces résonances pour un assemblage à base d'un dérivé de Guanosine est possible, grâce à l'utilisation d'expérience de corrélation multidimensionnelle $^{13}\text{C}-^{13}\text{C}$ et, pour la première fois, de spectre de corrélation $^{13}\text{C}-^{15}\text{N}$.

L'accent est alors mis sur l'obtention d'information structurale sous la forme de distances carbone-carbone et carbone-azote à partir d'expériences de transfert d'aimantation (expériences dites de "recouplage dipolaire"). Plusieurs stratégies sont discutées pour l'obtention de courbes de transfert d'aimantation sur des échantillons en AN. La dilution naturelle des isotopes ^{13}C et ^{15}N présente ici un avantage décisif pour ces mesures en réduisant de manière importante la troncature dipolaire, ce qui permet un transfert de polarisation sur de longues distances sans perturbation engendrée par la présence d'un troisième spin. Il en découle une description simplifiée de la dynamique de spin qui peut ainsi être facilement reproduite par des simulations numériques. Cette approche est démontrée expérimentalement sur des nanotubes du peptide diphénylalanine cyclique auto-assemblé (cyclo-FF). Les courbes de transfert d'aimantation^{13}C$-^{13}$C et ^{13}C$-^{15}$N obtenues sont effectivement sensibles à de longues distances allant jusqu'à $\approx 7\,\text{Å}$, et sont en excellent accord avec les simulations basées sur la structure cristalline du cyclo-FF. De plus, chaque courbe de transfert d'aimantation est constituée d'une superposition de contributions multiples intra et intermoléculaires, et contiennent donc une information structurale très riche.

Il est ensuite montré que le contenu élevé de l'information contenu dans ces courbes de transfert d'aimantation et leur description théorique simple permettent de déterminer à la fois la structure moléculaire et la structure supramoléculaire du cyclo-FF. Ceci est réalisé à l'aide d'un code de calcul dédié qui crée de manière systématique des modèles structuraux par translation/rotation moléculaire et différentes symétries possible de la maille cristalline. Ces modèles sont ensuite classés en fonction de leur accord avec les données expérimentales.

La thèse conclut en présentant des améliorations méthodologiques pour la séquence d'impulsions de recouplage dipolaire homonucléaire SR26. Cette séquence est particulièrement puissante pour une utilisation sur des échantillons en AN. Ces améliorations permettent une augmentation de l'efficacité du recouplage et l'acquisition de spectres de corrélation 2D avec de larges fenêtres spectrales.

En résumé, cette thèse démontre que l'utilisation d'échantillons organiques en AN présente d'importants avantages pour leur étude structurale par RMN en phase solide qui devient possible avec la technique de DNP sous MAS.

List of publications

Parts of this thesis are based on the following publications:

- Chapter 2:
  K. Märker, M. Pingret, J.-M. Mouesca, D. Gasparutto, S. Hediger, G. De Paëpe, "A new tool for NMR crystallography: Complete $^{13}C/^{15}N$ assignment of organic molecules at natural isotopic abundance using DNP-enhanced solid-state NMR", J. Am. Chem. Soc. 137 (2015) 13796−13799.

- Chapter 3 (except sections 3.4 and 3.6) and chapter 4.2:
  K. Märker, S. Paul, C. Fernández-de-Alba, D. Lee, J.-M. Mouesca, S. Hediger, G. De Paëpe, "Welcoming natural isotopic abundance in solid-state NMR: Probing π-stacking and supramolecular structure of organic nanoassemblies using DNP", Chem. Sci. 8 (2017) 974−987.

- Chapter 5.2:
  K. Märker, S. Hediger, G. De Paëpe, "Efficient 2D double-quantum solid-state NMR spectroscopy with large spectral widths", Chem. Commun. 53 (2017) 9155−9158.

Contents

Chapter 1

Introduction

1.1 Principles of solid-state NMR

1.1.1 Solid-state NMR of organic compounds

Solid-state nuclear magnetic resonance (ssNMR) spectroscopy is a powerful analytical technique used to study structure and dynamics of a wide range of samples. It can provide insights at the atomic level and is in principle not restricted by sample size or crystallinity. Applications of ssNMR span a wide range from biomolecules[1–3] over hybrid compounds[4,5] to inorganic materials.[6–8] This thesis will focus on structure determination of organic assemblies by dynamic nuclear polarization (DNP, see section 1.2) enhanced ssNMR.

NMR is based on the interaction of the nuclear spin magnetic moment with magnetic fields. In the presence of a magnetic field, the energy levels of a spin-$^1/_2$ nucleus split into two spin states. This effect is called the Zeeman interaction. The energy difference between the two energy levels is given by

$$\Delta E = \hbar\gamma B_0 = -\hbar\omega_0, \tag{1.1}$$

where $\hbar$ is the reduced Planck constant, γ is the gyromagnetic ratio, and B_0 the magnetic field strength. ω_0 is the nuclear Larmor frequency in angular frequency units at which nuclear spins precess around the direction of the magnetic field.

The populations of the two energy levels at thermal equilibrium are determined by the Boltzmann population. The resulting population difference - the nuclear spin polarization P - is therefore

$$P = \tanh\left(\frac{\Delta E}{2k_BT}\right), \tag{1.2}$$

where k_B is the Boltzmann constant and T the absolute temperature. This spin polarization produces a macroscopic spin magnetic moment which is the subject of NMR.

The energy difference between the Zeeman states (equation 1.1) and therefore also the spin polarization (equation 1.2) are usually very small, meaning that NMR experiments have an inherently low sensitivity. In addition, their sensitivity strongly depends on the isotope investigated, more precisely on its gyromagnetic ratio γ, its natural isotopic abundance (NA), and its spin. Table 1.1 lists these parameters for some NMR-active isotopes which are found in organic molecules.

Table 1.1: Spin, gyromagnetic ratio γ with respect to γ_H, and natural isotopic abundance (NA) of the main NMR-active isotopes in organic samples.

Nucleus	Spin	NA	$\lvert\gamma/\gamma_\mathrm{H}\rvert$
^{1}H	$^1/_2$	99.98 %	1
^{2}H	1	0.02 %	0.15
^{13}C	$^1/_2$	1.1 %	0.25
^{14}N	1	99.6 %	0.07
^{15}N	$^1/_2$	0.37 %	0.10
^{17}O	$^5/_2$	0.04 %	0.14

Several of these isotopes have a spin greater than $^1/_2$, meaning that they are quadrupolar. The large size of quadrupolar interactions poses additional challenges for NMR spectroscopy, but will not be discussed further here, as this thesis will focus on spin-$^1/_2$ nuclei. Among the spin-$^1/_2$ nuclei in Table 1.1 (^{1}H, ^{13}C, ^{15}N), protons appear as the best target for NMR owing to their high NA and gyromagnetic ratio. However, this also gives rise to very strong homonuclear dipolar interactions (see section 1.1.2) which greatly impair the resolution of proton spectra in ssNMR. Experiments on ^{13}C and/or ^{15}N usually provide spectra of much better resolution, making them the best target nuclei for studying organic samples. Due to their lower NA and gyromagnetic ratios, such experiments are rather limited in sensitivity if no isotopic enrichment or hyperpolarization methods are applied.

1.1.2 Spin-$1/2$ interactions in solids

In NMR experiments, nuclear spins experience a multitude of interactions which can be classified as external spin interactions with the experimental apparatus and internal spin interactions with the sample itself (Figure 1.1).[9,10] The external spin interactions are the Zeeman interaction with the static magnetic field and the interaction with radiofrequency (RF) pulses. The internal interactions are the chemical shift interaction, the dipole-dipole coupling, and the J-coupling. Another internal spin interaction is the quadrupolar interaction which only occurs for nuclei with a spin greater than $1/2$ and will therefore be ignored in the following. The spin Hamiltonian of a spin-$1/2$ nucleus can be expressed as a sum of all interactions:

$$\mathcal{H} = \mathcal{H}_{\mathrm{Z}} + \mathcal{H}_{\mathrm{RF}} + \mathcal{H}_{\mathrm{CS}} + \mathcal{H}_{J} + \mathcal{H}_{\mathrm{DD}}. \tag{1.3}$$

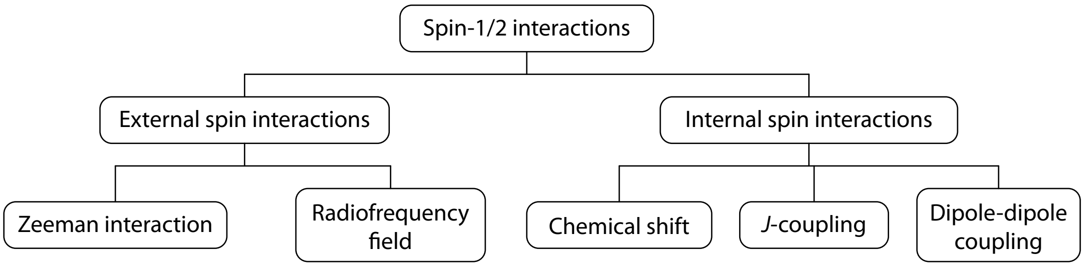

Figure 1.1: Overview of spin interactions for spin-$1/2$ nuclei.

The Zeeman interaction represents the interaction with the external magnetic field, leading to splitting of the nuclear spin energy levels as described in section 1.1.1. It is far greater than any of the other interactions described here and can be written under the secular approximation as

$$\mathcal{H}_{\mathrm{Z}} = -\gamma \hbar B_0 I_z, \tag{1.4}$$

where I_z is the component of the spin angular momentum vector which is parallel to B_0.

For an NMR experiment, RF pulses are applied at the nuclear Larmor frequency. They create an oscillating magnetic field perpendicular to B_0, which is used to manipulate the nuclear spins. Their interaction with this field of field strength B_1

and frequency ω_{RF} can be written as

$$\mathcal{H}_{\mathrm{RF}}(t) = -\gamma\hbar B_1 \cos(\omega_{\mathrm{RF}} t) I_x, \tag{1.5}$$

where I_x is the spin angular momentum perpendicular to B_0.

The chemical shift interaction is an indirect interaction of nuclear spins with B_0, caused by electrons. The external magnetic field induces currents in the electron cloud of the sample which in turn generates an induced magnetic field. This induced field in- or decreases the local magnetic field at the site of the nucleus, causing its resonance frequency to shift away from its Larmor frequency. This is called the chemical shift interaction which, under the secular approximation, can be expressed as

$$\mathcal{H}_{\mathrm{CS}} = -\gamma\hbar\sigma B_0 I_z, \tag{1.6}$$

where σB_0 describes the induced field. The electron cloud in a molecule is usually not isotropic due to chemical bonding and electronegativity effects. Therefore, the chemical shift interaction has an anisotropic component and is described by the second-rank tensor σ, which is called the chemical shielding tensor. Its principal values (σ_{xx}, σ_{yy}, σ_{zz}) are used to describe the chemical shift anisotropy (CSA) of a nucleus based on three parameters: The isotropic chemical shielding σ_{iso}, the anisotropy σ_{aniso}, and the asymmetry η.

The isotropic chemical shielding σ_{iso} is defined as the mean of the principal values of σ:

$$\sigma_{\mathrm{iso}} = \frac{1}{3}(\sigma_{xx} + \sigma_{yy} + \sigma_{zz}). \tag{1.7}$$

Normally, the isotropic chemical shift δ_{iso} is reported instead of σ_{iso}, and is determined with respect to a reference compound (e.g., tetramethylsilane at $\delta_{\mathrm{iso}} = 0$ for ^{13}C). Based on the isotropic chemical shielding of both compounds, it can be defined as

$$\delta_{\mathrm{iso}} = \sigma_{\mathrm{iso,ref}} - \sigma_{\mathrm{iso}}. \tag{1.8}$$

Several conventions exist for describing the chemical shift anisotropy. This thesis will use the Haeberlen convention[11] which defines the principal values as

$$|\sigma_{zz} - \sigma_{\mathrm{iso}}| \geq |\sigma_{xx} - \sigma_{\mathrm{iso}}| \geq |\sigma_{yy} - \sigma_{\mathrm{iso}}|, \tag{1.9}$$

and accordingly the anisotropy σ_{aniso} and the asymmetry η as

$$\sigma_{\text{aniso}} = \sigma_{zz} - \sigma_{\text{iso}}, \tag{1.10}$$

$$\eta = \frac{\sigma_{yy} - \sigma_{xx}}{\sigma_{\text{aniso}}}. \tag{1.11}$$

Due to this anisotropy, the chemical shift depends on the orientation of the chemical shielding tensor with respect to B_0. In a powdered solid, all possible orientations are present and give rise to a so-called powder pattern which is illustrated in Figure 1.2a. The shape of a powder pattern arises from the superposition of signals from different crystallite orientations. The three principal values of the chemical shielding tensor can be determined from the singularities in the powder pattern, and the isotropic chemical shift lies in its center of mass (see Figure 1.2a).

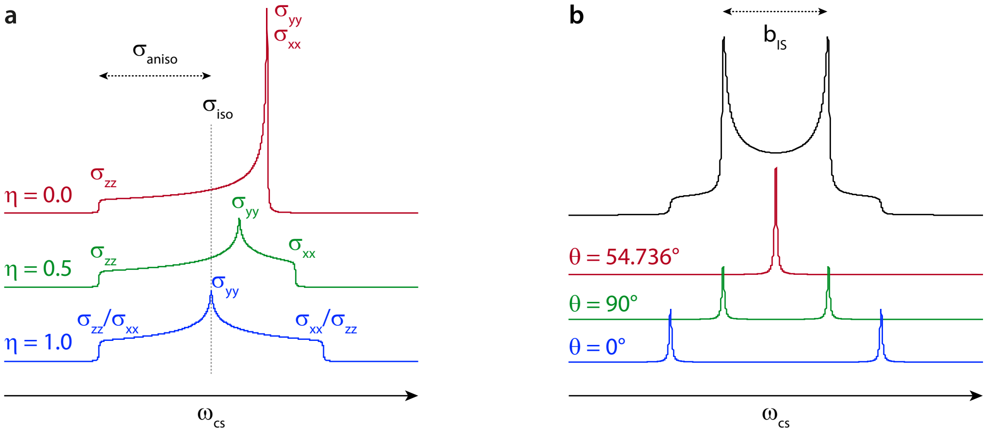

Figure 1.2: Effects of CSA (a) and heteronuclear dipole-dipole coupling interactions (b) on the appearance of the spectrum of a static sample. (a) Powder patterns of nuclei with the same isotropic chemical shielding and anisotropy, but different asymmetries η. (b) Pake pattern for a heteronuclear spin pair (black), and contributing spectra for different orientations of the dipolar vector with respect to B_0, described by the angle θ.

The dipole-dipole (or dipolar) coupling is a direct coupling between two nuclear spins which proceeds through space. It is caused by small magnetic fields created by the two spin magnetic moments. The dipolar coupling is purely anisotropic and depends on the angle θ between the internuclear vector and B_0. One can distinguish between the homo- and the heteronuclear dipolar coupling, i.e. couplings between two spins of the same or of different isotopic species, respectively. Under the secular approximation, their Hamiltonians are given as

$$\mathcal{H}_{\mathrm{DD}}^{\mathrm{homo}} = -\frac{1}{2} b_{IS} (3\cos^2\theta - 1)\left[3 I_z S_z - I \cdot S\right], \tag{1.12}$$

$$\mathcal{H}_{\mathrm{DD}}^{\mathrm{hetero}} = -b_{IS} (3\cos^2\theta - 1) I_z S_z, \tag{1.13}$$

where I and S are the angular momentum operators of the two spins, and b_{IS} is the dipolar coupling constant between them, defined as

$$b_{IS} = \frac{\hbar \mu_0 \gamma_I \gamma_S}{4\pi r_{IS}^3}, \tag{1.14}$$

with μ_0 being the vacuum permeability and r_{IS} the internuclear distance. The dependence of the dipolar coupling on r_{IS} makes its measurement of a very useful approach for structural studies, because it directly allows the determination of internuclear distances.

The dipolar coupling splits the NMR signals of both nuclei involved into a doublet. Since the extent of the splitting depends on θ, a superposition of doublets for different crystallite orientations is observed for a spin pair in a powdered solid (Figure 1.2b). The resulting lineshape is called a Pake pattern and can be understood as two overlapping powder patterns with $\eta = 0$ and opposite signs of σ_{aniso}. The "horns" of the Pake pattern represent orientations in which the internuclear vector is perpendicular to B_0 ($\theta = 90°$) and their spacing corresponds to b_{IS} (in a heteronuclear spin pair). The left- and rightmost ends of the pattern correspond to orientations in which the internuclear vector is parallel to B_0 ($\theta = 0°$), and the center of the powder pattern corresponds to $\theta \approx 54.736°$. This is the so-called magic angle θ_{MA}, corresponding to the angle between the diagonal of a cube and one of its sides which is parallel to B_0. In this case, the $(3\cos^2\theta - 1)$ term in equations 1.12 and 1.13 is zero which means that also the dipolar coupling Hamiltonian is zero and only one line at δ_{iso} is observed. This phenomenon is utilized in magic-angle spinning which will be described in more detail in the following section.

Similar to the dipolar coupling, the J-coupling (also called scalar coupling) arises from the interaction of the magnetic moments of two spins, but it is an indirect through-bond coupling which is mediated by the bonding electrons. Although it is in principle an anisotropic interaction, the consideration of its isotropic part, given by

$$\mathcal{H}_J = \hbar J_{IS} I \cdot S, \tag{1.15}$$

is usually sufficient. J_{12} is the J-coupling constant and rather small compared to other interactions in solids. For instance, a ^{13}C-^{13}C one-bond J-coupling is usually not larger than 100 Hz.[12] Line splitting due to J-couplings in solids can therefore only be observed when comparably narrow linewidths are present, but can still lead to broadening of ^{13}C signals in uniformly ^{13}C-labeled solids.[13]

1.1.3 Common experimental techniques

Due to the inherently low sensitivity of NMR and the presence of anisotropic interactions, achieving good sensitivity and resolution is a great challenge for ssNMR. In the last few decades, several ground-breaking techniques for enhancing sensitivity and/or resolution were developed, among them magic-angle spinning (MAS),[14,15] heteronuclear decoupling,[16] and cross polarization (CP).[17,18] MAS and decoupling lead to narrower lines and therefore improved resolution and sensitivity. CP can provide additional sensitivity enhancement by transferring polarization from a high-γ spin species to a lower-γ one.

The concept of magic-angle spinning was first proposed and demonstrated independently by Andrew *et al.*[14] and Lowe.[15] It involves spinning the sample around an axis which is at the magic angle ($\theta_{\mathrm{MA}} = \arctan\sqrt{2} \approx 54.736°$) with respect to B_0 (Figure 1.3a). This causes averaging of the CSA and dipolar coupling interaction to zero (to first order) due to their $(3\cos^2\theta - 1)$ dependence. In order for this averaging to be efficient, the spinning frequency should be at least as high as the magnitude of the anisotropic interactions.

In spectra recorded under MAS, spinning sidebands are observed which are spaced from the central peak at integer multiples of the spinning frequency. Their number and intensity depend on the size of the spinning frequency compared to the magnitude of the interaction, which is illustrated in Figure 1.3b. While MAS frequencies of more than 100 kHz can now be achieved,[19] MAS frequencies in DNP applications presented in this thesis are limited to ≤ 14 kHz owing to the low temperature of the spinning gas (typically ≈ 100 K) and the associated challenges in probe design.

MAS is however not sufficient to remove the effects of dipolar interactions involving protons because of the homogeneous nature of the proton-proton dipolar couplings in the large proton spin bath. This results for example in severe line broadening in ^{13}C spectra caused by heteronuclear dipolar couplings to the proton network. In this context, heteronuclear decoupling is an invaluable technique

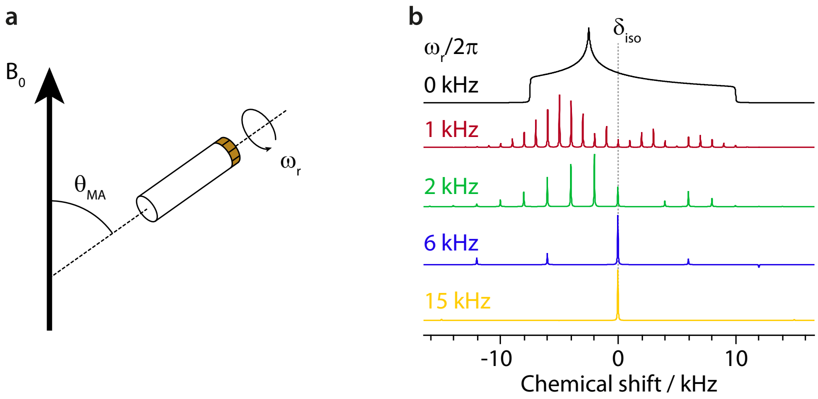

Figure 1.3: (a) Schematic representation of magic-angle spinning at an angular spinning frequency ω_r, with $\theta_{\mathrm{MA}} = \arctan\sqrt{2} \approx 54.736°$. (b) Effect of increasing MAS frequency on the appearance of a powder pattern ($\sigma_{\mathrm{aniso}} = 10$ kHz, $\eta = 0.5$).

which aims at removing the effects of heteronuclear dipolar interactions through the application of RF pulse sequences on the protons.[20] Among the most powerful heteronuclear decoupling sequences today are phase-modulated sequences like SPINAL-64[21] and SW$_f$-TPPM.[22]

Since proton spectra are often poorly resolved in ssNMR, nuclei with lower gyromagnetic ratio are usually detected which unfortunately have lower polarization. The CP technique aims at enhancing the sensitivity of such experiments by utilizing the larger proton polarization. Transfer of polarization from protons to another spin species X can be achieved by simultaneous irradiation of both spins with spin-locking fields at a CP matching condition.[17,18,23] The CP matching condition under MAS is fulfilled when the amplitudes of the two RF fields differ by integer multiples of the spinning frequency, i.e. $\omega_{\mathrm{H}} - \omega_{\mathrm{X}} = \pm z\omega_r$ with $z = 1, 2$.[24] In practice, one of the RF fields is usually ramped around the matching condition in order to improve its efficiency.[25] A theoretical maximum sensitivity enhancement of $|\gamma_{\mathrm{H}}/\gamma_{\mathrm{X}}|$ for nucleus X can be achieved, being ≈ 4 for ^{13}C and ≈ 10 for ^{15}N.

MAS, heteronuclear decoupling, and CP are standard techniques for acquiring high-resolution spectra of ^{13}C or ^{15}N spins. Figure 1.4a shows the basic CPMAS pulse sequence incorporating these techniques. It starts with a 90° pulse on protons which is followed by polarization transfer to X by CP, here with a ramp on the proton channel. During the following detection of the free induction decay (FID), heteronuclear decoupling is applied on the proton channel to counteract the dipolar interactions between ^{1}H and X. Another practical advantage of the CPMAS sequence is that the experiment starts from proton magnetization, meaning that the optimal recycle delay depends on the longitudinal relaxation rate (T_1) of protons and not on the T_1 of X which is usually considerably longer. This allows faster repetition rates of the experiment, providing an additional increase in sensitivity.

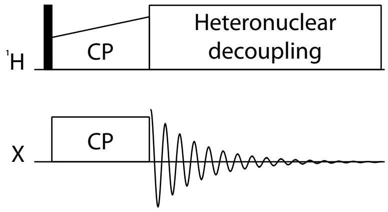

Figure 1.4: Basic pulse sequence of a CPMAS experiment.

1.2 Magic-angle spinning dynamic nuclear polarization

1.2.1 The concept of DNP

Even with the experimental methods described in the previous section, sensitivity still remains a strong limiting factor in ssNMR. Dynamic nuclear polarization is a technique for further sensitivity enhancement, aiming at transferring electron polarization to atomic nuclei. With the gyromagnetic ratio of an electron spin being ≈ 660 times larger than that of a proton spin, sensitivity enhancements by several orders of magnitude can in theory be achieved.

The idea of DNP was first proposed by Overhauser in 1953 for experiments in metals,[26] and demonstrated experimentally in the same year by Carver and Slichter.[27] However, the use of DNP in high-field MAS ssNMR experiments has only recently emerged as a true experimental alternative, with commercial 400 MHz, 600 MHz, and 800 MHz (^{1}H Larmor frequency) MAS-DNP systems being available today.[28,29] This development was pioneered by Griffin and co-workers who worked for example on the use of gyrotrons as high-power high-frequency microwave sources[30–32] and the development of powerful polarizing agents.[33,34] In recent years, MAS-DNP has enabled numerous experiments that were unfeasible with standard high-field NMR systems, such as the rapid acquisition of signals from diluted species as well as nuclei with low gyromagnetic ratio and/or low NA.[35–37] In addition, advanced experiments on organic solids at NA are possible, such as probing ^{13}C$-$^{13}C proximities through two-dimensional (2D) correlation spectra.[38–41]

Today, a standard MAS-DNP experiment is conducted on a sample which is doped with an organic biradical. A gyrotron source supplies continuous-wave microwave irradiation to the sample which is spun with cold nitrogen gas at $\approx 100\,\mathrm{K}$. Polarization is continuously transferred from the paramagnetic dopant to surrounding nuclei and distributed in the sample via spin diffusion. The theoretical and practical aspects of MAS-DNP will be described in more detail in the following sections.

1.2.2 Mechanisms for polarization transfer

Three main mechanisms can drive polarization transfer from unpaired electron spins to nuclear spins in MAS-DNP:[37] The cross effect (CE), the solid effect (SE), and the Overhauser effect (OE). Under the experimental conditions used in most MAS-DNP applications today, the CE[42,43] is the most efficient transfer mechanism. It is caused by mutual spin flips of an electron-electron-nuclear spin system and requires a biradical with a large electron-electron coupling and a broad electron paramagnetic resonance (EPR) line due to large g-anisotropy (TOTAPOL, AMUPol, TEKPol, see section 1.2.6). The SE[44] relies on irradiation of (forbidden) electron-nuclear zero-quantum (ZQ) or double-quantum (DQ) transitions and works best with narrow-line radicals such as BDPA or Trityl. The OE[26] requires irradiation of (allowed) electron single-quantum (SQ) transitions. Hyperpolarization of nuclear spins is then induced by differences in ZQ and DQ relaxation rates. This effect is very prominent in systems with mobile electrons such as metals and liquids, and was recently shown to also occur in insulating solids, induced by radicals with high electron mobility and a large number of hyperfine couplings (e.g., BDPA).[45]

The theoretical background of these effects has first been described in static samples and can be understood based on four and eight energy level diagrams for electron-nuclear (SE, OE) and electron-electron-nuclear (CE) spin systems, respectively.[46] However, these models do not explain certain experimental observations in MAS-DNP, such as a spinning dependency of the signal enhancement.[28] In 2012, Thurber and Tycko[47] as well as Mentink-Vigier *et al.*[48] demonstrated with the help of numerical simulations that the hyperpolarization mechanisms for SE-DNP and CE-DNP under MAS are distinct from those in a static sample. They have to be regarded as a series of avoided energy-level crossings (see section 1.2.3) which occur periodically during each rotor period. This analysis can be performed for each of the three DNP mechanisms, but will be restricted here to the CE as it is currently the most powerful polarization transfer mechanism and the only one which has been exploited in this thesis.

1.2.3 Cross effect DNP under MAS

As mentioned above, the CE requires (at least) two dipolar coupled electrons (e1 and e2) and one nucleus (n) with a hyperfine coupling to one electron (for simplicity, only the n-e1 coupling is considered here, see Figure 1.5a). They form an eight energy level system (Figure 1.5b) whose energies are determined by the Zeeman interaction and hence the Larmor frequencies (ω_{e1}, ω_{e2}, ω_{n}), the dipolar coupling between the two electrons with coupling constant $D_{\text{e1-e2}}$, and the hyperfine coupling between the nucleus and electron 1 with coupling constant $H_{\text{n-e1}}$. Weaker interactions will be ignored here.

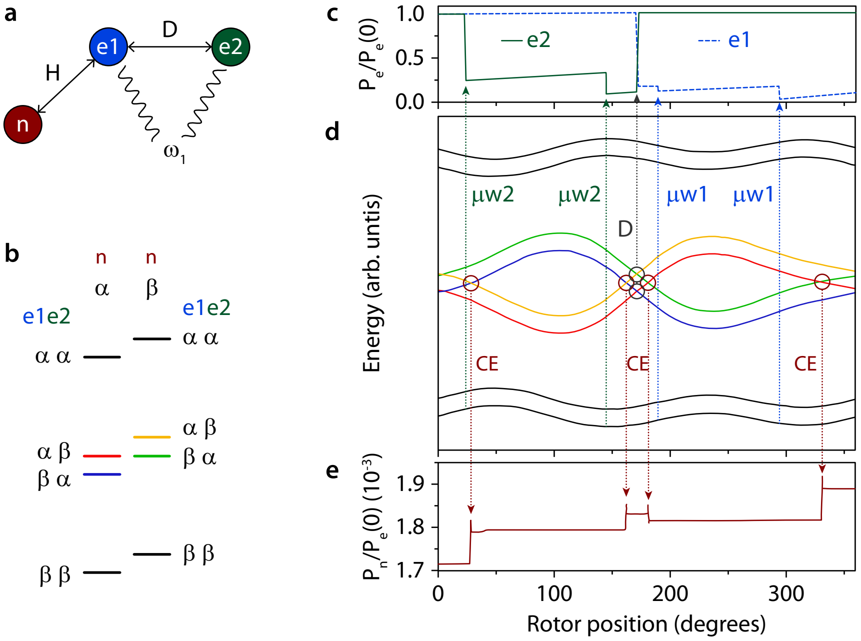

Figure 1.5: (a) Illustration of the electron-electron-nuclear spin system considered for CE-DNP and the important interactions: hyperfine coupling with coupling constant $H_{\text{n-e1}}$, dipolar coupling with coupling constant $D_{\text{e1-e2}}$, microwave irradiation with field strength ω_1. (b) Energy level diagram for the three spin system in (a). Because of the opposite signs of the gyromagnetic ratio of electron and proton spins, the lower energy levels are labeled opposite (α for n and β for e1 and e2). (c-e) Evolution of energy levels (d) and electron (c) and nuclear (e) polarization over one rotor period, based on numerical simulations in ref. 48. Microwave (µw1/µw2), dipolar (D), and cross effect (CE) rotor events are indicated by circles and vertical dotted lines and labeled in the same color. Figure adapted from ref. 49.

During sample rotation, these energy levels are modulated periodically due do the anisotropy of the aforementioned interactions.[47,48] The evolution of energy levels during one rotor period is illustrated for one crystallite orientation in Figure 1.5d.

As it can be seen, a number of different energy level crossings occurs which have to be treated as avoided level crossings (anticrossings). In avoided crossings, the energy levels never become exactly the same due to non-zero off-diagonal terms in the related Hamiltonians. If these anticrossings occur slowly enough and if the off-diagonal terms are large enough, they approach adiabaticity and the populations of the two energy levels are exchanged. This is the crucial process which drives MAS-DNP.

Three important anticrossings, termed rotor events by Mentink-Vigier *et al.*,[50] have to be distinguished in the case of CE-DNP. As summarized in Table 1.2, they can be characterized by the nature of spins involved, the frequency matching condition, and the main interactions that are responsible for their anticrossing nature as they appear in the off-diagonal terms. Note that the fourth anticrossing in Table 1.2, the SE rotor event, is crucial for SE-DNP, but not very influential for CE-DNP and shall therefore be ignored here for simplicity.

Table 1.2: Characterization of the rotor events occurring during CE-DNP under MAS with respect to the spins involved, the frequency matching condition, and the major mediating interaction(s) which are defined here by their interaction strength (ω_1: microwave field strength, $D_{\text{e1-e2}}$: electron-electron dipolar coupling, $H_{\text{n-e1}}$: electron-nuclear hyperfine coupling).

Rotor event	Spins involved	Matching condition	Mediating interaction
Microwave	e1 or e2	$\omega_\text{e} \approx \omega_{\mu\text{w}}$	ω_1
Dipolar	e1+e2	$\omega_\text{e1} \approx \omega_\text{e2}$	$D_{\text{e1-e2}}$
CE	e1+e2+n	$\lvert\omega_\text{e1} - \omega_\text{e2}\rvert \approx \omega_\text{n}$	$D_{\text{e1-e2}}$, $H_{\text{n-e1}}$
SE	e1+n	$\omega_\text{e1} \pm \omega_\text{n} \approx \omega_{\mu\text{w}}$	ω_1, $H_{\text{n-e1}}$

The interplay of the main three rotor events and their impact on electron and nuclear polarization over multiple rotor periods is a very complex process and has therefore been simulated numerically.[47,48] The outcome of such a simulation for one crystallite orientation is represented in Figure 1.5c-e. It shows the fluctuations of energy levels over one rotor period at steady-state (d) as well as the development of electron (c) and nuclear polarizations (e) during the first rotor period after the beginning of microwave irradiation. Rotor events are indicated by vertical dotted lines.

Following this process over one rotor period highlights the nature of rotor events and their impact on electron and nuclear polarization. The first rotor event is a microwave event (labeled as μw2) for electron 2. It decreases this electron's polarization, consequently increasing the population difference to electron 1. Next, a CE event occurs near the degeneracy of the two levels $|\alpha_{\mathrm{e1}}\beta_{\mathrm{e2}}\beta_{\mathrm{n}}\rangle \leftrightarrow |\beta_{\mathrm{e1}}\alpha_{\mathrm{e2}}\alpha_{\mathrm{n}}\rangle$. Because of the polarization difference between e1 and e2 created before, the population exchange at this anticrossing increases the nuclear polarization. The series of these two events (μw2 event, CE event) repeats another time which further increases the nuclear polarization. Next, a dipolar rotor event (labeled as D) occurs near the degeneracies of $|\alpha_{\mathrm{e1}}\beta_{\mathrm{e2}}\alpha_{\mathrm{n}}\rangle \leftrightarrow |\beta_{\mathrm{e1}}\alpha_{\mathrm{e2}}\alpha_{\mathrm{n}}\rangle$ and $|\alpha_{\mathrm{e1}}\beta_{\mathrm{e2}}\beta_{\mathrm{n}}\rangle \leftrightarrow |\beta_{\mathrm{e1}}\alpha_{\mathrm{e2}}\beta_{\mathrm{n}}\rangle$. This event is usually very efficient (highly adiabatic) and induces an almost complete polarization exchange between the two electrons, maintaining their large population difference. This polarization exchange means that the following two μw1 rotor events further increase the electron polarization difference and that the two CE rotor events, now occurring near the degeneracy $|\beta_{\mathrm{e1}}\alpha_{\mathrm{e2}}\beta_{\mathrm{n}}\rangle \leftrightarrow |\alpha_{\mathrm{e1}}\beta_{\mathrm{e2}}\alpha_{\mathrm{n}}\rangle$, can further increase the nuclear polarization.

The electron and nuclear longitudinal relaxation times (T_{1e} and T_{1n}) play an important role in this process. Since the changes in polarization during one rotor event are usually not very big, many consecutive events have to occur and add up to create substantial nuclear hyperpolarization. Sufficiently long T_{1n} is therefore required to allow buildup of the nuclear polarization over several rotor periods. A long T_{1e} is important for maintaining a large polarization difference between the two electrons as electron relaxation constantly decreases this difference. This is one of the main reasons why DNP experiments are conducted at low temperatures. The effect of T_{1e} on electron polarization is also visible in Figure 1.5c.

In a powdered solid, not only one crystallite orientation is present as shown in Figure 1.5, but a mixture of all possible orientations. For each orientation, the hyperfine and dipolar couplings are different, and the modulation of energy levels with spinning differs. In consequence, the rotor events occur at different points in time, and overall, many more orientations can experience an efficient CE than in a static sample. Indeed, the DNP enhancement shows a strong increase when going from a static sample to slow spinning frequencies.[28,48] At higher spinning frequency however, the efficiency slowly decreases because there is less time for anticrossings to occur and polarization exchange is less efficient.

1.2.4 Depolarization

The CE mechanism under MAS has important implications for spectra of a DNP sample that are recorded without microwave irradiation. As it can be seen from Table 1.2, only the microwave and the SE rotor event require microwave irradiation, whereas dipolar and CE rotor events can also occur in its absence. In this case, the dipolar rotor events tend to equilibrate the populations of the two electrons because no microwave events occur that would increase their polarization difference. If the electron polarization difference becomes smaller than the nuclear polarization difference, the CE events will reduce nuclear polarization by transferring it to the electrons.[50,51]

This effect was first described by Thurber and Tycko[51] for experiments at 25 K. Shortly after, Mentink-Vigier *et al.*[50] demonstrated that it also has significant influence on spectra recorded under the "standard" DNP conditions at ≈100 K. When a sample contains a CE biradical like TOTAPOL or AMUPol, the signal integral in "microwave-off" spectra recorded under MAS conditions is clearly smaller than that under static conditions. On the other hand, it remains constant in samples containing the monoradical Trityl which is used for SE-DNP.[50]

Numerical simulations demonstrated a few additional interesting aspects of depolarization:[50] Most crystallite orientations which depolarize strongly do not hyperpolarize very well and *vice versa*. This indicates that in samples with strong depolarization there are many radicals with unfavorable orientations which do not contribute positively to the DNP effect. The depolarization effect becomes more pronounced at long T_{1e} because this leaves more time for the electron polarizations to equilibrate, also by intermolecular electron-electron couplings. Hence, depolarization is more prominent at lower temperatures around 25 K.

An important implication of depolarization concerns the established way of quantifying DNP enhancement by $\epsilon_{\text{on/off}}$, which is obtained by comparing signal intensities measured with and without microwave irradiation. If the "microwave-off" signal is reduced due to depolarization, $\epsilon_{\text{on/off}}$ will become larger than the actual sensitivity gain and can even surpass the theoretical maximum of ≈ 660.[50,52] The evaluation of new DNP radicals or different sample preparation methods therefore has to be done with great care and should ideally be based on signal-to-noise measurements rather than $\epsilon_{\text{on/off}}$.

1.2.5 DNP hardware

The standard DNP setup uses a gyrotron as source of high-power high-frequency microwave irradiation,[30–32] a microwave transmission line, a cooling cabinet to cool the spinning gas flows to near liquid nitrogen temperature and a special MAS-DNP probe.[28,29]

The gyrotron tube which is under ultrahigh vacuum is placed inside a superconducting magnet (9.7 T for 263 GHz microwave frequency, used for 9.4 T NMR magnets). An electron gun inside the tube produces an electron beam which is initially accelerated by a high voltage and then further accelerated and focused by a magnetic field. It then passes through a resonant cavity which is located in the center of the gyrotron's magnetic field. In here, the electron beam energy is converted into microwave irradiation at a frequency which is mainly governed by the cavity dimensions and the magnetic field. The electron beam energy is then dissipated on a water-cooled collector, and the microwave beam leaves the gyrotron tube through an output window and is guided to the NMR probe through a corrugated waveguide.

The low-temperature MAS-DNP probe is specifically designed to accommodate a waveguide which delivers the microwave beam to the sample, irradiating perpendicular to the rotor axis. Moreover, it is thermally insulated to allow efficient cooling of the sample and inserting and ejecting samples at cryogenic temperatures.

Cold nitrogen gas is produced in the cooling cabinet which has three nitrogen-filled heat-exchange chambers to cool the three gas lines (bearing, drive, variable temperature). The chambers are immersed in a liquid nitrogen dewar which is constantly refilled from an external liquid nitrogen reservoir.

1.2.6 DNP radicals

The paramagnetic dopant is one of the most important parameters for DNP experiments. One of the breakthroughs for high-field DNP was the discovery that chemically linking two TEMPO radicals results in substantially increased enhancements, as this structure enables an efficient CE due to increased electron-electron dipolar couplings.[33] Shortly after, TOTAPOL (Figure 1.6a) was introduced,[34] which was the most efficient biradical for DNP experiments in aqueous solutions for more than five years.

Since then, great efforts have been made towards improving DNP radicals.[37] Today, the most commonly used radicals for CE-DNP are AMUPol[53] (Figure 1.6b) for applications in aequeous solutions and TEKPol[54] (Figure 1.6c) for applications

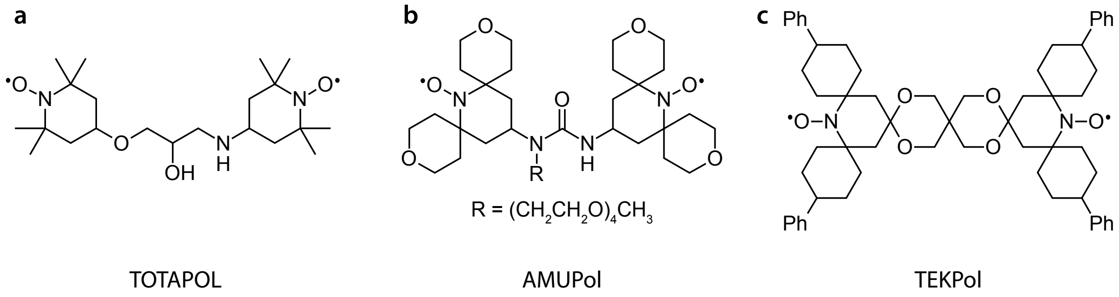

Figure 1.6: Chemical structures of CE-DNP polarizing agents TOTAPOL,[34] AMUPol,[53] and TEKPOL.[54]

in organic solvents. Both radicals have bulky substituents at the TEMPO rings, introduced with the aim of increasing nuclear and electron relaxation times.[55] Moreover, the two TEMPO rings are linked by rather short moieties, resulting in large electron-electron dipolar couplings.

However, enhancement factors in MAS-DNP experiments are still far from reaching their theoretical maximum, and plenty of room for radical development remains. Moreover, the availability of higher magnetic fields (up to 18.8 T[29]) and faster spinning frequencies[56] for DNP necessitates the development of dedicated radicals. For instance, the use of mixed trityl-TEMPO biradicals is a promising option for DNP at higher magnetic fields.[57] With the still growing theoretical understanding of CE-DNP in mind,[58] major improvements of DNP efficiency can still be expected in the future.

1.2.7 Sample preparation for DNP

Another decisive step for DNP is sample preparation, i.e. the incorporation of an exogeneous polarizing agent in a way that efficient hyperpolarization can be achieved. One of the earliest sample preparation methods is dissolving the analyte and the polarizing agent in a mostly deuterated glycerol/water matrix, commonly with a volume ratio D_8-glycerol/D_2O/H_2O of 60:30:10.[59] This matrix is often termed "DNP juice" and reflects two of the main concepts of DNP sample preparation. Firstly, the proton concentrations is kept at a low level which makes the hyperpolarization process of the smaller proton bath more efficient. At the same time, the concentration is high enough to enable efficient spin diffusion over a large volume and hence hyperpolarization of the whole sample. Secondly, the glycerol/water matrix forms a glass at low temperatures which ensures a uniform radical distribution.

This concept is a reliable preparation for obtaining high enhancement values

($\epsilon_{\text{on/off}}$). However, it is not applicable if one is interested in the 3D structure of a solid sample, which would be destroyed upon dissolution. In addition, the actual quantity of analyte in a frozen solution sample is rather small, and a larger quantity would be desirable for achieving higher sensitivity.

For powdered solids, the most common and simplest sample preparation method is so-called impregnation:[60] The radical is dissolved in a solvent which does not dissolve or alter the sample structure. The powdered sample is then mixed or ground with a small amount of the radical solution until a slightly wet paste is obtained. The most common radical-solvent combinations used are AMUPol in the standard “DNP juice” and TEKPol in 1,1,2,2-tetrachloroethane, with radical concentrations typically around 10 mM.

The impregnation method has the advantage that roughly the same sample quantity can be packed into a rotor as if the pure powder was used. It works particularly well in porous samples in which radical and solvent molecules can diffuse into the pores and distribute over the whole sample. However, impregnation is of limited power when particle sizes are too large, such that hyperpolarization cannot be transferred through the whole particle and/or polarization buildup times become very long. In such cases, one has to resort to more advanced sample preparation methods, such as the matrix-free approach.[38,40,61]

1.2.8 Judging the gain from DNP

In order to judge whether DNP - a relatively costly technique - is of actual use on a certain sample, the sensitivity gain has to be quantified properly. As mentioned before, the commonly used enhancement factor $\epsilon_{\text{on/off}}$ (or ϵ_{DNP}) is distorted by depolarization which affects the signal intensity of the reference spectrum without microwave irradiation.[50] Therefore, while $\epsilon_{\text{on/off}}$ is simple to measure and can serve as an indicator of DNP efficiency, it is not suitable for quantifying the real sensitivity gain.

A more relevant comparison is that to a conventional ssNMR experiment which can be quantified by the so-called Absolute Sensitivity Ratio (ASR).[38] The ASR is the ratio of the signal-to-noise per unit square root of time values that can be obtained with DNP and with conventional ssNMR at room temperature. This factor attempts a fair comparison by taking into account that conventional ssNMR experiments can make use of more diverse measurement conditions for increasing the sensitivity of a specific sample, such as the use of larger sample volumes, higher fields, and/or faster spinning.

Another important factor to consider when judging the applicability of DNP is the quality of the spectrum that can be obtained with DNP. Spectral resolution can be severely reduced at the low measurement temperatures due to the freezing of molecular motions, which is especially a problem in biological samples.[62] On the other hand, fairly rigid structures such as organic self-assemblies have been shown to experience only minor line broadening at low temperatures and are thus well-suited for DNP.[40] Moreover, low temperatures and/or the addition of a DNP matrix may alter the structure of the sample under investigation which is of course an unwanted effect. Finally, it should be kept in mind that coherence lifetimes such as T_2' and $T_{1\rho}$ may be shortened in the presence of a paramagnetic species.

1.3 NMR crystallography of organic solids

1.3.1 Structural information from solid-state NMR

Knowledge of the atomic-level structure of powdered organic solids is of great importance for understanding their properties and function. The use of ssNMR data for structure determination and refinement is often referred to as NMR crystallography.[63–65] As discussed in section 1.1, ssNMR experiments can provide a wealth of structural information, some of which are summarized below.

The chemical shielding of a nucleus depends on its electronic environment. Therefore, the isotropic and anisotropic chemical shift components encode information on the direct chemical surrounding of the respective nucleus. For instance, the presence of hydrogen bonds shifts resonances to higher frequencies, and resonance splitting in a sample can provide information on the size of its asymmetric unit cell. Further interpretation of chemical shift data is often enabled by density functional theory (DFT) which can be used to compute the expected chemical shielding tensor of a given structure (see next section).[66–68]

The J-coupling is mediated by the bonding electrons and can therefore be used to obtain information on internuclear connectivity. For example, 2D carbon-carbon correlation spectra using the J-coupling for polarization transfer will only show correlation peaks of nuclei which are directly bonded.[69]

Even more direct structural information can be obtained from the measurement of dipolar couplings, because the size of the dipolar coupling between two spins is inversely proportional to the cube of their distance (see equation 1.14). For this purpose, dipolar recoupling experiments are used, in which the dipolar couplings (averaged by MAS) are reintroduced and mediate polarization transfer.[70,71] The buildup of transferred polarization as a function of increasing recoupling time is recorded, and internuclear distances can be extracted from these curves. Such measurements of ^{13}C−^{13}C and ^{13}C−^{15}N dipolar couplings will be central to this thesis.

1.3.2 Complementary techniques

In the context of organic solids, the term NMR crystallography usually implies that NMR data is combined with information from other analytical and computational techniques.[63–65] Such techniques are for example powder X-ray diffraction (XRD), density functional theory (DFT), and computational modelling. The input from these techniques is an important contribution because of the limited sensitivity of NMR experiments on organic samples at their NA.

DFT is perhaps the most important complementary technique for NMR crystallography.[66–68] It is a quantum mechanical approach for *ab initio* electronic structure calculations, and computes the ground state energy of a given system of electrons. For these calculations, the energy is described as a functional (i.e., a function of a function) of the spatially dependent electron density. The electronic structure in solids is usually described using planewave basis sets and pseudopotentials in order to account for periodicity of the structure.

DFT can be applied to compute the energy and, if required, optimize the geometry of a given system. Its great utility for NMR lies in the fact that also the NMR parameters of the system can be computed, using the gauge-including projector-augmented wave (GIPAW)[72] approach. A common strategy in NMR crystallography is therefore the comparison of calculated and experimental NMR parameters, most commonly of the isotropic chemical shifts. Based on this comparison, potential structures can be validated, a structure can be chosen among a number of models, or a given structure, obtained for example from diffraction data, can be refined.[63–65]

Powder XRD is another analytical technique which can be applied to non-crystalline solids. As diffraction techniques are more sensitive to the long-range order and periodicity of a system than NMR, such data can provide valuable complementary information. Indexing of the powder pattern can often yield the unit cell parameters and the space group (or a set of space groups) which are extremely useful input parameters for structural modelling.[63–65] Powder diffraction data can also be used as another way of validating a final structure, as the calculation of the expected powder pattern for a given structure is straightforward.

Computational modeling or minimization of candidate structures is usually involved in NMR crystallography protocols, too. One such technique is crystal structure prediction (CSP) which aims at predicting possible crystal structure only based on knowledge of atom connectivities in a molecule.[73,74] CSP algorithms create a large set of potential crystal structures and their energies. As it can be expected that the "correct" structure will be among them, experimental NMR data can be used to evaluated these structures and identify the best one. Indeed, it has been shown that the comparison of experimental chemical shifts and the chemical shifts calculated for each predicted structure can be used for structure determination.[75,76] Proton chemical shifts have been shown to be particularly sensitive to the supramolecular structure,[75] and even allowed the *de novo* structure determination of a large drug molecule without a known crystal structure.[76]

1.3.3 Use of DNP for NMR crystallography

As mentioned before, NMR experiments on organic solids are limited by their low sensitivity due to the low NA of ^{13}C and ^{15}N spins. This limitation becomes even more severe for 2D correlation experiments and/or distance measurements, since the probability of encountering a particular $^{13}\mathrm{C}{-}^{13}\mathrm{C}$ or $^{13}\mathrm{C}{-}^{15}\mathrm{N}$ spin pair is as low as $\approx 0.01\,\%$ and $\approx 0.001\,\%$, respectively. MAS-DNP now provides a tool which can greatly enhance the sensitivity of ssNMR experiments and make such correlations feasible. For instance, a DNP-enhanced $^{13}\mathrm{C}{-}^{13}\mathrm{C}$ 2D correlation spectrum of NA cellulose can be recorded in only 20 minutes[38] whereas this would have required several days under normal ssNMR conditions.

The use of NA samples for advanced correlation experiments is not only made possible by DNP, but comes with the advantage of greatly reduced dipolar truncation as compared to isotopically labeled samples. Dipolar truncation describes the phenomenon that small homonuclear dipolar couplings are truncated by larger dipolar couplings.[77] This makes polarization transfer over long distances very challenging and the corresponding multi-spin dynamics very complex. Hence, the exact determination of long distances in uniformly ^{13}C-labeled systems is extremely difficult. In a sample which contains ^{13}C at its NA, on the other hand, $^{13}\mathrm{C}{-}^{13}\mathrm{C}$ spin pairs can be expected to occur mostly isolated, meaning that undisturbed polarization transfer over long distances is possible, which is extremely valuable for supramolecular structure determination. Indeed, it has been shown that cross-peaks corresponding to intermolecular contacts can be obtained in ^{13}C$-$^{13}C correlation spectra recorded at NA.[40,41] The simple spin dynamics in a two-spin system are expected to make distance measurements from dipolar recoupling experiments much more straightforward. The work reported in this thesis will take advantage of this situation for internuclear distance measurements.

1.4 Outline of this thesis

The aim of this thesis is to explore the new possibilities that the sensitivity enhancement from MAS-DNP offers for structure determination of organic solids at their NA. The major focus lies on the use of dipolar recoupling experiments for ^{13}C$-$^{13}C and ^{13}C$-$^{15}N distance measurements, exploiting the advantages of reduced dipolar truncation at NA.

In chapter 2, it is shown that DNP-enhanced ssNMR can be used for recording ^{13}C$-$^{13}C and ^{15}N$-$^{13}C correlation spectra of an organic sample at its NA. These spectra allow the full ^{13}C and ^{15}N resonance assignment of a deoxyguanosine derivative with two molecules in the asymmetric unit cell which could not have been assigned from one-dimensional (1D) spectra alone.

Chapter 3 demonstrates the feasibility of probing ^{13}C$-$^{13}C and ^{15}N$-$^{13}C distances at NA. On the self-assembled cyclic diphenylalanine peptide (cyclo-FF),[40] approaches for recording polarization buildup curves based on 1D or 2D spectra will be presented. Upon comparison to the known crystal structure of cyclo-FF, a detailed analysis of the buildup curves is conducted and information regarding the number of contributing distances, their range, and the (small) effects of dipolar truncation can be extracted. It is shown that these curves do contain a multitude of internuclear distances and are in excellent agreement with simulations based on the crystal structure.

Chapter 4 presents steps towards a full *de novo* structure determination protocol which is primarily based on polarization buildup curves obtained with DNP-enhanced ssNMR. First, the molecular structure of cyclo-FF is determined by combining the NMR data with molecular mechanics and DFT. Then, a code for supramolecular structure elucidation is presented which is based on knowledge of the molecular conformation. It is used to determine a structure which is in excellent agreement with the crystal structure of cyclo-FF, demonstrating the accuracy of the buildup curves described in chapter 3.

In chapter 5, improvements for the SR26 recoupling sequence[78] are presented since this sequence is well suited for obtaining long-range distance information. The chapter shows how SR26 2D DQ-SQ correlation spectra can be recorded with an arbitrary spectral width in the indirect dimension, and how the DQ-filtering efficiency of SR26 can be increased by rearranging the sequence blocks in a certain order. Theoretical explanations and experimental demonstrations are given for both aspects.

Chapter 2

Complete ^{13}C/^{15}N resonance assignment for NMR crystallography

2.1 Introduction

2.1.1 Resonance assignment in NMR crystallography

The essential first step for solid-state NMR studies on organic molecules consists in assigning all resonances to the corresponding atom in the molecule. As described in section 1.1.2, the chemical shifts are highly sensitive to the local chemical environment. The isotropic chemical shifts therefore act as unique identifiers for each atom in a molecule and contain valuable structural information. Resonance assignment is thus also a central aim of the "traditional" NMR crystallography approach which is based on comparing the experimental chemical shifts to the chemical shifts obtained from DFT computations with the GIPAW method on a structural model,[63–65] as introduced in section 1.3.2.

When molecular size and complexity increase, resonance assignment becomes very challenging due to peak overlap and ambiguities in 1D spectra. Two- (or even higher-) dimensional NMR spectra are then required to separate resonances and obtain information about connectivities through the observed correlation peaks. The acquisition of an additional experimental dimension requires the presence of a coupling (*J*-coupling or dipolar coupling) between close-by nuclear spins, and substantially increases the experimental time. In NA organic samples, this increase easily becomes prohibitive when considering $^{13}C-^{13}C$ or $^{13}C-^{15}N$ correlation spectra since the probability of encountering suitable spin pairs is very low (see also section 1.3.3).

Typical 2D correlation experiments in NMR crystallography display at least one proton spectral dimension,[79] both because of the high abundance and gyromagnetic ratio of protons, but also because their chemical shifts are very sensitive to the crystal packing.[75,76] $^{13}C-^{13}C$ or $^{13}C-^{15}N$ correlations are usually out of reach due to the low NA of these spin pairs. Hence, the broad applicability of NMR crystallography is limited by poor proton spectral resolution, even though significant progress has been made on this front over the last few decades.[80,81]

Consequently, a *de novo* resonance assignment is not straightforward, especially when spectral ambiguities occur, caused, for example, by peak splitting due to polymorphism or crystallographic asymmetry.[82] In particular, the inability to assign ^{13}C and ^{15}N resonances also affects the proton assignment, which is mostly done from H−X correlation spectra. In such instances, tentative assignments, mostly relying on comparisons with DFT results, become necessary. This constitutes a potential source of uncertainties and errors.[82]

This chapter shows that this limitation can be overcome and reports the first complete *de novo* ^{13}C and ^{15}N chemical shift assignment of a NA sample with two molecules in the asymmetric crystallographic unit cell. This approach is exclusively based on NMR experimental data, notably involving the first NA $^{15}N-^{13}C$ correlation spectrum. Owing to the high spectral resolution, an unambiguous assignment is straightforward and does not require any previous knowledge of the crystal structure. MAS-DNP is used to compensate for the very low sensitivity of these experiments and makes them feasible within hours.

2.1.2 Self-assembled guanosine derivatives

The resonance assignment for NMR crystallography using MAS-DNP is demonstrated on 2'-deoxy-3',5'-dipropanoylguanosine ($dG(C3)_2$, Figure 2.1a), a derivative of the DNA base deoxyguanosine.[83] It is a representative of the large family of self-assembled guanosine-based architectures, with possible applications in fields ranging from medicinal chemistry to nanotechnology.[84–86] Solid guanine-based architectures for instance could be used to fabricate molecular electronic devices like photodetectors and light-harvesting systems.[85–87]

Mediated by hydrogen bonding, $dG(C3)_2$ self-assembles into a ribbon-like structure in the solid state, displaying two independent molecules in the asymmetric unit cell, as shown by X-ray crystallography.[88] Previous ssNMR studies of dG(C3)$_2$ and related compounds were able to reveal different hydrogen bonding arrangements, which allows to distinguish quartet- and ribbon-like self-assembly.[89,90] In ^{15}N isotopically enriched samples, intermolecular ^{15}N-^{15}N correlation peaks could unambiguously be assigned to the different hydrogen bonding patterns.[89] Moreover, characteristic features of these patterns were identified in ^{1}H spectra of NA samples.[90] However, a full resonance assignment of dG(C3)$_2$ so far had to rely on GIPAW chemical shift calculations based on the known crystal structure, since separate assignment of the two molecules in the asymmetric unit cell was not possible from NMR alone.[90]

2.2 Results and discussion

2.2.1 DNP on dG(C3)$_2$

For DNP experiments, dG(C3)$_2$ was impregnated with a 10 mM solution of the biradical AMUPol[53] in D$_8$-glycerol/D$_2$O (60:40 v/v). DNP-enhanced ^{13}C and ^{15}N CPMAS spectra of this sample are shown in Figure 2.1b and c. The DNP signal enhancement ($\epsilon_{\mathrm{on/off}}$) is 11 and an ASR of >10 was measured (see section 1.2.8), which translates into a time saving factor of at least 100 compared to conventional ssNMR experiments (using a 4 mm rotor at room temperature, RT). The CPMAS spectra at 105 K are consistent with, and of similar resolution, to spectra recorded at RT (see Figure 2.1d,e), with only minor resonance shifts (<2 ppm) and broader CH$_3$ contributions occurring. The spectra shown here are very similar to published spectra,[89,90] with this DNP sample presenting the expected ribbon-like structure. Worth noticing are also the remarkably narrow ^{13}C and ^{15}N linewidths at 105 K (60−70 Hz for ^{13}C and ≈ 40 Hz for ^{15}N resonances). This is an indicator of a rigid self-assembled structure, but also a result of measuring at NA, where the carbon lines in 1D spectra are not broadened by J_{CC} couplings.

A striking feature of the CPMAS spectra is the doubling of peaks for the majority of the resonances (differences up to 3.5 ppm for C3' and 4.4 ppm for N7) due to the presence of two distinct molecules (A and B) in the asymmetric unit cell of dG(C3)$_2$.[88] This signal splitting makes the acquisition of 2D spectra necessary for complete resonance assignment.

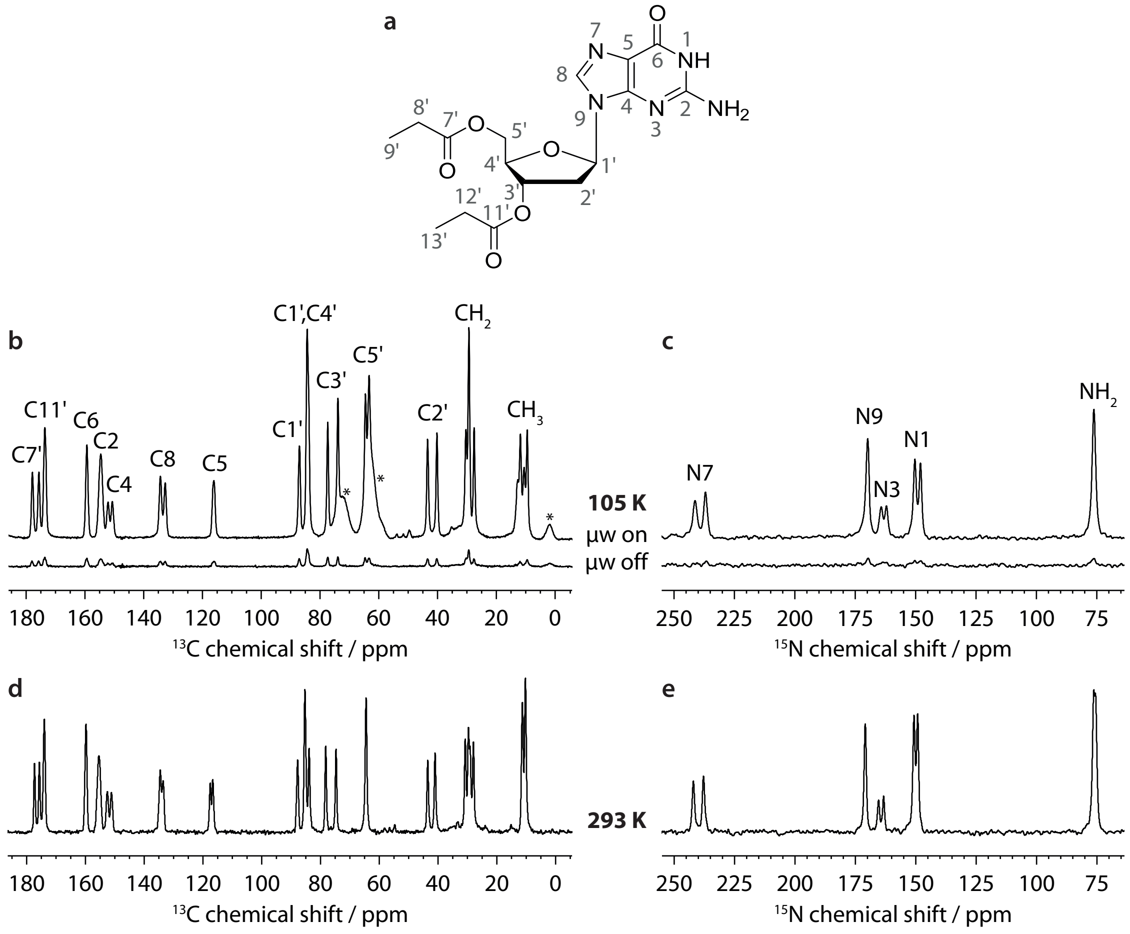

Figure 2.1: (a) Chemical structure of dG(C3)$_2$. (b,c) ^{13}C and ^{15}N CPMAS spectra of the dG(C3)$_2$ DNP sample. The spectra were taken at 105 K with and without microwave irradiation (μw on/off). Asterisks indicate silicon grease and glycerol (from sample synthesis and preparation). (d,e) ^{13}C and ^{15}N CPMAS spectra of dG(C3)$_2$ powder, taken at room temperature (293 K).

2.2.2 Full ^{13}C and ^{15}N resonance assignment

As a first step for ^{13}C resonance assignment, a through-bond ^{13}C$-^{13}$C J-refocused INADEQUATE spectrum[69] was recorded (Figure 2.2a). As multiple-bond J-couplings are very small, the spectrum only shows one-bond contacts and the unambiguous connection of directly bonded carbon nuclei is possible. This allows the identification of the different dG(C3)$_2$ subunits for the two conformers, i.e. deoxyribose, the two propanoyl side chains and a part of the guanine base (C4$-$C6). For deoxyribose, signals belonging to molecules A and B can be clearly distinguished (see also Figure 2.4). However, a connection to other parts of the molecule cannot be made, as the chains of carbon atoms are interrupted by nitrogen or oxygen atoms. Based on this spectrum alone, it is thus not possible to assign the propanoyl and guanine resonances to molecules A and B. In addition, the two propanoyl side chains of one molecule cannot be distinguished.

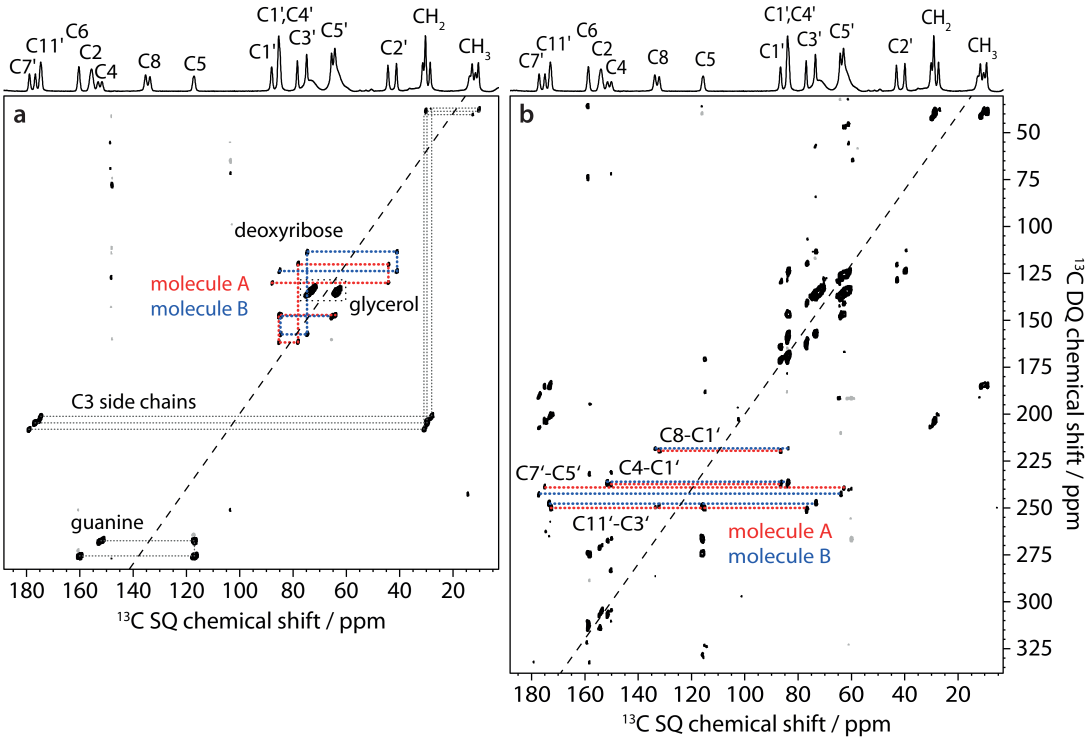

Figure 2.2: (a) ^{13}C—^{13}C *J*-refocused INADEQUATE spectrum[69] of dG(C3)$_2$. The spectrum was recorded in ≈ 18 h. (b) ^{13}C—^{13}C DQ-SQ correlation spectrum of dG(C3)$_2$, obtained with the dipolar recoupling sequence SR26[78,91] at 8 kHz MAS frequency, using a total recoupling time (DQ excitation plus reconversion) of 4 ms. Two spectra were co-added, each taken in ≈ 7 h. The ^{13}C CPMAS spectra are shown above for illustrative purposes.

For this purpose, a through-space ^{13}C—^{13}C correlation spectrum was recorded with the dipolar recoupling sequence SR26,[78,91] applying STiC phase shifts to achieve a sufficiently large indirect dimension (see section 5.2). Acquired with the DQ-excitation and -reconversion mixing times set each to 2 ms, the spectrum shown in Figure 2.2b displays both one-bond and two-bond correlations, and allows to complete the ^{13}C assignment. As highlighted in the spectrum, the two propanoyl side chains can be distinguished and the corresponding resonances assigned through the C7'-C5' and C11'-C3' correlations. In addition, the C1'-C4 and C1'-C8 correlations allow for the unambiguous assignment of the split guanine resonances C4 and C8 to molecules A and B. The latter will be confirmed by a ^{15}N—^{13}C double CP-based[92] heteronuclear correlation experiment (DCP-HETCOR) discussed below. The two ^{13}C—^{13}C correlation spectra in Figure 2.2 thus permit the complete assignment of all ^{13}C resonances of both conformers.

For the assignment of nitrogen resonances, a ^{15}N—^{13}C DCP-HETCOR spectrum of dG(C3)$_2$ was recorded (Figure 2.3).[93] To the best of our knowledge, this is the first time such an experiment has been achieved at NA in ssNMR. The ^{15}N−^{13}C CP contact time (7 ms) was chosen such that only one-bond transfers can occur. Despite the very low NA of both nuclei, this demonstrates the feasibility of a ^{15}N−^{13}C correlation spectrum with good signal-to-noise ratio in reasonable experimental time (cf. ≈ 25 h instead of > 100 days without MAS-DNP). The spectrum clearly shows all expected one-bond correlations. This allows the straightforward assignment of all nitrogen resonances for both conformers, when combined with only the partial ^{13}C chemical shift assignment obtained from the *J*-refocused INADEQUATE spectrum. Indeed, since N9 is linked to C1', which shows a clear splitting for molecules A and B, the assignment of nitrogen resonances for A and B is possible. This additionally allows to assign the split C4 and C8 resonances.

Overall, the three presented spectra (Figures 2.2 and 2.3) allow the complete assignment of all ^{13}C and ^{15}N resonances, including the differentiation of molecules A and B. This assignment is summarized in Table 2.1.

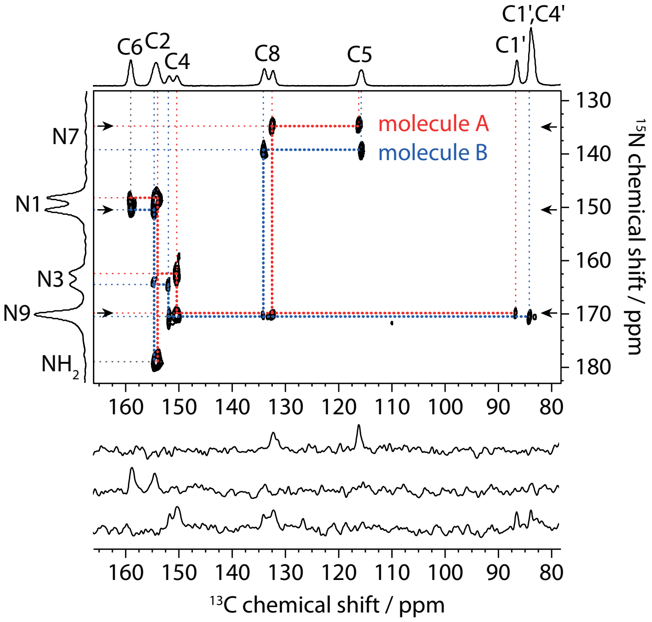

Figure 2.3: ^{15}N−^{13}C DCP-HETCOR spectrum of dG(C3)$_2$. ^{15}N−^{13}C polarization transfer was achieved by adiabatic transfer (APHH-CP)[93] with a contact time of 7 ms. The spectrum was recorded in ≈ 25 h. The spectral width in the indirect dimension was optimized such that N7 and NH$_2$ resonances are folded on the respective opposite side of the spectrum. ^{13}C and ^{15}N CPMAS spectra are shown above and left for illustrative purposes, respectively. Cross sections are shown below the spectrum, taken at the positions indicated by arrows.

Table 2.1: Experimental ^{13}C and ^{15}N chemical shifts of dG(C3)$_2$ and their assignments. ^{13}C and ^{15}N chemical shifts are reported with respect to TMS at 0 ppm and liquid NH$_3$ at 0 ppm, respectively, and were calibrated with glycine as an external reference at RT (CO at 176.0 ppm, NH$_2$ at 33.4 ppm).

Carbon						**Nitrogen**		
$\delta(^{13}C)$	Assignment		$\delta(^{13}C)$	Assignment		$\delta(^{15}N)$	Assignment	
177.6	C7'	B	83.9	C1'	B	241.5	N7	B
175.4	C7'	A	83.6	C4'	B	237.1	N7	A
173.6	C11'	B	77.0	C3'	A	170.2	N9	B
172.9	C11'	A	73.5	C3'	B	169.6	N9	A
159.0	C6	A,B	64.2	C5'	B	164.4	N3	B
154.4	C2	B	62.9	C5'	A	162.1	N3	A
154.0	C2	A	43.0	C2'	A	150.3	N1	B
151.8	C4	B	39.8	C2'	B	148.0	N1	A
150.3	C4	A	30.0	C8'	B	76.1	NH$_2$	A,B
134.0	C8	B	28.9	C8'	A			
132.3	C8	A	28.9	C12'	B			
116.2	C5	A	27.2	C12'	A			
115.6	C5	B	11.4	C9'	A,B			
86.7	C1'	A	9.1	C13'	A,B			
84.2	C4'	A						

2.2.3 Comparison to GIPAW-based assignment

The *de novo* assignment of both dG(C3)$_2$ conformers presented here (see Table 2.1) is globally in agreement with previously published GIPAW-based results.[90] However, one important discrepancy is found concerning the carbonyl resonances of the C3 side chains (C7' and C11'). Correlation peaks between these carbonyl and the deoxyribose resonances (C7'-C5' and C11'-C3') in the SR26 spectrum clearly show that the carbonyl signals at lower field belong to C7' and those at higher field to C11', which contradicts the computational results used for assignment in ref. 90. Although GIPAW calculations are clearly a powerful method, this demonstrates that their results should always be examined with care.

The carbonyl assignment based on NMR data can also be rationalized from the dG(C3)$_2$ crystal structure: the C7' carbonyl group is involved in a hydrogen bond with the NH$_2$ group of an adjacent molecule (see Figure 2.4), which could explain the downfield shift of the C7’ resonances with respect to the C11’ signal. Moreover, this hydrogen bond seems to present a slightly different length for the two conformations A and B, namely 3.0 Å and 3.1 Å (O−N distance, highlighted in orange in Figure 2.4). This allows the tentative assignment of molecules A and B to the two different conformations in the X-ray structure, with B being the one with the C7’ signal at lower field. This corresponds to the assignment given in Table 2.1. In comparison to the GIPAW based assignment,[90] the same resonances are attributed to molecules A and B in both assignments, except for the aforementioned exception of C7’ and C11’.

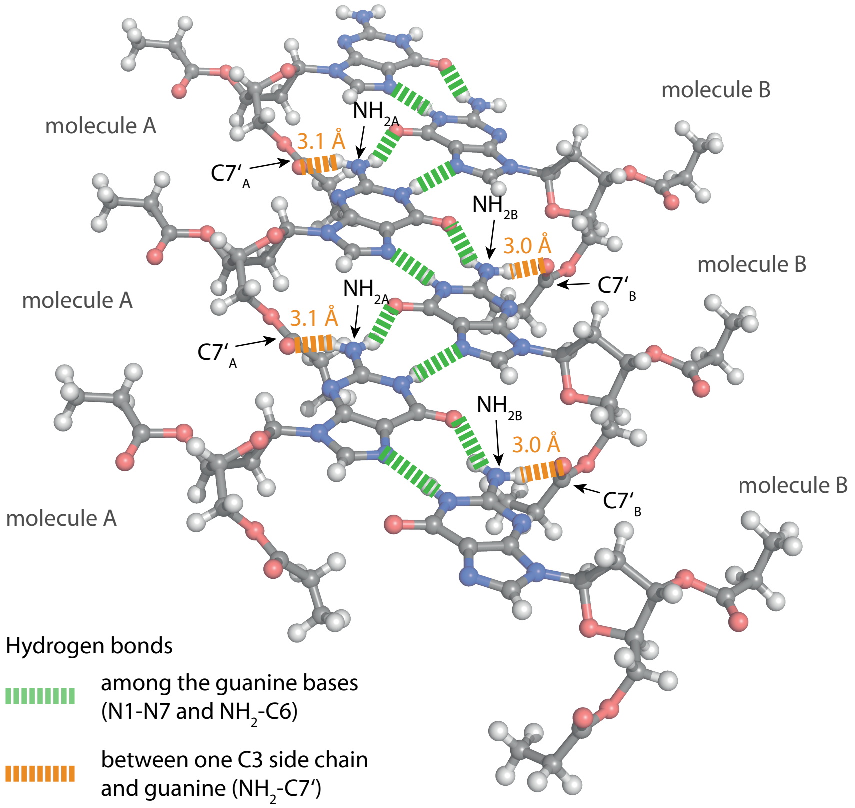

Figure 2.4: Illustration of hydrogen bonding in the crystal structure of dG(C3)$_2$ (structure taken from ref. 88), causing the ribbon-like assembly. Hydrogen bonds among the guanine bases (green) are 2.8 and 2.9 Å long and hydrogen bonds between one of the C3 side chains and the guanine NH$_2$ group (orange) are 3.0 and 3.1 Å long (N-O or N-N distances).

2.3 Conclusions

This chapter has presented the first complete *de novo* ^{13}C and ^{15}N resonance assignment of ribbon-like self-assembled dG(C3)$_2$ at NA obtained using DNP-enhanced ssNMR spectroscopy. The assignment was accomplished on the basis of three 2D experiments: a through-bond J-refocused INADEQUATE displaying one-bond $^{13}C-^{13}C$ connections, a through-space homonuclear correlation spectrum based on SR26 dipolar recoupling showing additional longer distance $^{13}C-^{13}C$ correlations, and finally a $^{15}N-^{13}C$ DCP-HETCOR for assigning the ^{15}N resonances. Notably, we were able to separately assign the two different molecules in the asymmetric unit cell of dG(C3)$_2$. This had previously required GIPAW calculations based on the known crystal structure,[90] which however did not yield the fully correct assignment, as shown here. With the assignment of carbon and nitrogen resonances, the assignment of ^1H chemical shifts using H-X HETCOR experiments becomes straightforward.

The ability to obtain *de novo* ("DFT-free") NMR assignments at NA is an essential improvement for NMR crystallography, since it does not require prior knowledge of the structure and circumvents potential DFT-based assignment errors. Even more so, the feasibility of performing $^{13}C-^{13}C$ and $^{15}N-^{13}C$ 2D correlation experiments at NA is also the crucial first step towards structure determination based on distance measurements, following a similar strategy to the one developed for isotopically enriched biomolecules. Notably, the inclusion of ^{15}N will prove particularly useful for investigating structurally essential interactions like hydrogen bonding.

2.4 Materials and methods

Synthesis of dG(C3)$_2$ and DNP sample preparation

2'-Deoxy-3',5'-dipropanoylguanosine (dG(C3)$_2$) was synthesized according to literature[83] and recrystallized in a 2.5:1 mixture of tetrahydrofuran and water.

For DNP experiments, dG(C3)$_2$ (30 mg) was impregnated with a 10 mM solution (30 µL) of the biradical AMUPol[53] in D_8-glycerol/D_2O (60:40 v/v). The sample had a pasty consistency, did not contain excess liquid, and was fully packed into a 3.2 mm thin-wall zirconia rotor.

NMR experimental details

All DNP experiments presented in this thesis were recorded on a 9.4 T Bruker AVANCE III wide-bore NMR system equipped with a 263 GHz gyrotron, a microwave transmission line and a low-temperature 3.2 mm MAS-DNP probe operating at ≈ 105 K.[28] The probe was used in double-resonance or triple-resonance mode, depending on the experiment. Data were recorded and processed using Bruker Topspin 3.2.

Low-temperature spectra of dG(C3)$_2$ were recorded at 12.5 kHz MAS frequency and with a recycle delay of 2.6 s, unless stated otherwise. For all spectra, proton pulses as well as SPINAL-64 decoupling[21] were applied at an RF-field strength of 100 kHz. Carbon pulses were applied at an RF-field strength of 50 kHz. CP from protons to carbon or nitrogen was carried out using adiabatic passage Hartmann-Hahn CP[94] (APHH-CP) with the ^{13}C and ^{15}N RF-field strengths fixed to 50 kHz and an adiabatic tangential sweep around the $n = +1$ Hartmann-Hahn condition at an average RF-field strength of 62.5 kHz on the proton channel. The CP contact times were 3.5 ms for CP to carbon and 4 ms for CP to nitrogen. States-TPPI quadrature detection[95] was used for all 2D spectra.

For the ^{13}C−^{13}C J-refocused INADEQUATE spectrum[69] shown in Figure 2.2a, the J-evolution periods were rotor synchronized and set to 3.04 ms each. Acquisition times were 30 ms in the direct dimension and 2.4 ms in the indirect dimension. 128 transients were accumulated for each of the 96 complex points of the indirect dimension, leading to a total experimental time of ≈ 18 h. Prior to Fourier transform, data were zero-filled in both dimensions and apodized with 40 Hz exponential line-broadening in the direct dimension only.

The ^{13}C−^{13}C DQ-SQ dipolar correlation spectrum of Figure 2.2b employing the SR26 recoupling scheme[78,91] was acquired at 8 kHz MAS frequency. Two spectra were taken, one with the SR26 sequence and one with two cycles of the $(S_0S_0')_{\mathrm{exc}}(S_0'S_0)_{\mathrm{rec}}$ sequence (see section 5.3), with otherwise identical parameters. For the recoupling periods , the ^{13}C RF-field strength was set to 52 kHz and continuous-wave Lee-Goldburg (CW-LG) decoupling[96] was applied on the proton channel at an RF-field strength of 100 kHz. The total mixing time (DQ excitation plus reconversion) was 4 ms, and acquisition times were 20 ms in the direct and 1.9 ms in the indirect dimension. 80 transients were accumulated for each of the 62 t_1 complex points, leading to a total experimental time of ≈ 7 h for each spectrum. STiC phase shifts were applied in both cases (see section 5.2). Prior to Fourier transform, data were zero-filled in both dimensions and apodized with 40 Hz exponential line-broadening in the direct dimension only. The two spectra gave similar results and were added to give the spectrum in Figure 2.2b.

For the ^{15}N−^{13}C DCP-HETCOR spectrum, ^{15}N−^{13}C polarization transfer was performed using APHH-CP,[93] with the ^{13}C RF-field strength set to 50 kHz and an adiabatic ramp around the $n = -1$ Hartmann-Hahn condition on the nitrogen channel (average RF-field amplitude of 37.5 kHz). The CP contact time was 7 ms. CW-LG decoupling at an RF-field strength of 90 kHz was applied on the proton channel during CP. Acquisition times were 20 ms in the direct dimension and 7.0 ms in the indirect dimension. The spectral width in the indirect ^{15}N dimension was set to 4167 Hz (102.7 ppm), resulting in folding of the N7 and NH_2 resonances. 600 transients were accumulated for each of the 29 t_1 complex points, leading to a total experimental time of ≈ 25 h. Prior to Fourier transform, data were zero-filled in both dimensions and apodized with 50 Hz exponential line-broadening in the direct dimension only.

Room temperature spectra were acquired on a 9.4 T Bruker wide-bore NMR spectrometer, equipped with a 4 mm double-resonance MAS probe. A 4 mm rotor filled with dG(C3)$_2$ powder as obtained from synthesis and purification was used. ^{13}C and ^{15}N CPMAS spectra were obtained respectively with 1024 and 81920 added scans, using a recycle delay of 3.9 s. No apodization was applied to the ^{13}C spectrum, and the ^{15}N spectrum was apodized with 20 Hz exponential line-broadening.

Chapter 3

Probing homo- and heteronuclear distances at natural abundance

3.1 Distance measurements at NA

3.1.1 Strategies

As it has been explained in the introduction, internuclear distances can be determined through the measurement of dipolar couplings (see section 1.3.1). They can be extracted from plots of the transferred polarization in a dipolar recoupling experiment as a function of increasing recoupling times. When such curves - called "(polarization) buildup curves" in this thesis - are to be recorded at NA of ^{13}C and/or ^{15}N, problems arise due to the large number of uncoupled spins which dominate the spectrum without providing any distance information. Special care has therefore to be taken to suppress these signals.

This chapter presents three different approaches for recording buildup curves of $^{13}\mathrm{C}{-}^{13}\mathrm{C}$ and $^{13}\mathrm{C}{-}^{15}\mathrm{N}$ polarization transfers at NA. For homonuclear ($^{13}\mathrm{C}{-}^{13}\mathrm{C}$) distance measurements, two complementary approaches are shown. The first one makes use of selective pulses which ensures that polarization transfer originates from only one or very few resonances. With the source of polarization known, no second spectral dimension is required and buildup curves can be recorded from a series of 1D spectra. This "1D approach" offers the advantage of very short experimental times. In the second, more traditional strategy, $^{13}\mathrm{C}{-}^{13}\mathrm{C}$ buildup curves are extracted from a series of 2D DQ-SQ correlation spectra where DQ filtration is applied to remove signals from uncoupled spins. This "2D approach" is of course more time-consuming, but also more universally applicable. It enables distance measurements between spins with similar isotropic chemical shifts, for which selective pulses cannot be conveniently applied.

$^{13}C{-}^{15}N$ distance measurements are a valuable extension to the homonuclear case as they make an additional set of distances available for structural studies. Selection of $^{13}C{-}^{15}N$ spin pairs over uncoupled spins can be achieved by a coherence transfer step from one spin species to the other. The measurements are accompanied by additional challenges as $^{13}C{-}^{15}N$ correlation experiments exhibit lower sensitivity due to the lower NA of ^{15}N. Furthermore, the smaller gyromagnetic ratio of ^{15}N means that $^{13}C{-}^{15}N$ dipolar couplings are about four times smaller than $^{13}C{-}^{13}C$ couplings for the same distance. Consequently, the longest distance measurable in $^{13}C{-}^{15}N$ recoupling experiments is generally shorter than in $^{13}C{-}^{13}C$ experiments.

In the following, these three approaches for distance measurements at NA will be demonstrated experimentally on the self-assembled cyclic diphenylalanine peptide (cyclo-FF, see section 3.2),[97] using MAS-DNP for sensitivity enhancement. The experimental data will be analyzed based on numerical simulations and the known crystal structure of cyclo-FF.[98] The main objective of this chapter is to evaluate the information content and accuracy of experimental buildup curves to assess their utility for obtaining structural information. The term “distance measurements” as used here does therefore not mean that distances are directly determined from the experimental data. This possibility will be discussed in the following chapter, together with other approaches for *de novo* structure determination.

3.1.2 Pulse sequences

The choice of a good recoupling pulse sequence is crucial for the success of dipolar recoupling experiments, especially when they involve quantitative distance measurements. One important point to consider is the efficient suppression of interferences from other interactions such as CSA, chemical shift offsets, RF inhomogeneity, and couplings to protons. In the present case, good compensation for CSA was particularly important since the sample under investigation has carbonyl and aromatic carbons. Both possess large CSAs (up to 200 ppm for aromatic carbons[99]) which can dramatically decrease the efficiency of most recoupling pulse sequences.[100] Additionally, the recoupling sequence should not have too high RF power requirements to enable long recoupling times without damaging the probe hardware. For these reasons, the S_3 and $[S_3]$ pulse sequences[101,102] were chosen for homonuclear recoupling and TEDOR was chosen for heteronuclear recoupling.[103]

The S_3 and $[S_3]$ pulse sequences are part of a series of homonuclear dipolar recoupling sequences S_p developed by Edén and co-workers.[101,102] They are recursively generated from symmetry-based sequences (see section 5.1.1),[104] according to the scheme $S_p \equiv S\mathrm{R}2^1_{2^p} \equiv \mathrm{R}2^1_{2^p}\mathrm{R}2^{-1}_{2^p}$ with $p = 1, 2, 3, \dots$. Upon increasing sequence order p, their compensation for resonance offsets, RF inhomogeneity and CSA improves progressively, at the expense of a longer sampling interval. All S_p sequences require very low RF power ($\omega_{nut} = \omega_r/2$). They were originally designed for the very fast MAS regime ($\omega_r/2\pi \geq 60\,\mathrm{kHz}$) where they do not require additional ^{1}H decoupling.[101] It was later shown that they can also be efficiently applied in the moderate spinning regime, if the spinning frequency is considerably larger than the strength of the CSA ($\omega_r \geq 1.5\omega_{\mathrm{CSA}}$) and high-power ^{1}H decoupling is applied.[102]

The S_3 pulse sequence can be written explicitly as[101]

$$\begin{aligned} S_3 \equiv S\mathrm{R}2^1_8 \equiv\ & 360_{270}\ 270_{90}\ 90_{270}\ 360_{90}\ 270_{270}\ 90_{90} \\ & 360_{90}\ 270_{270}\ 90_{90}\ 360_{270}\ 270_{90}\ 90_{270} \end{aligned} \tag{3.1}$$

with flip angles and RF phases (subscripts) given in degrees. Its construction is also illustrated in Figure 3.1a. The full sequence spans 16 rotor periods and has the aforementioned RF power requirement ($\omega_{nut} = \omega_r/2$). The sequence order $p = 3$ was chosen because p is large enough to provide good compensation for CSA, but the sequence is still short enough to allow sufficiently small steps for sampling the polarization buildup. Owing to the low recoupling power, the recoupling bandwidth of S_3 is limited at the experimental conditions used in this thesis. With the maximum spinning frequency being $\approx 14\,\mathrm{kHz}$, the available recoupling bandwidth is $\approx 7\,\mathrm{kHz}$ which corresponds to about half the ^{13}C spectrum at 9.4 T.

For the construction of $[S_3]$ (“bracketed S_3”), the S_3 pulse sequence is “sandwiched” between two $\pi/2$ pulses.[101] This removes ZQ terms which are created by S_3 together with the DQ terms. $[S_3]$ is therefore a pure DQ recoupling sequence and can be used without DQ filtration which is beneficial for the 1D approach (section 3.3). The scaling factor of $[S_3]$ (≈ 0.530) is twice as large as that of S_3 (≈ 0.265),[101] meaning that polarization transfer is twice as fast. This is advantageous for the recoupling of small dipolar interactions.

The TEDOR pulse sequence is based on the REDOR (rotational-echo double-resonance) experiment[105,106] whose basic pulse scheme is shown in Figure 3.1b. While magnetization of one spin species (here ^{13}C) evolves under a spin echo, two π-pulses per rotor period are applied on the other spin species (here ^{15}N). These

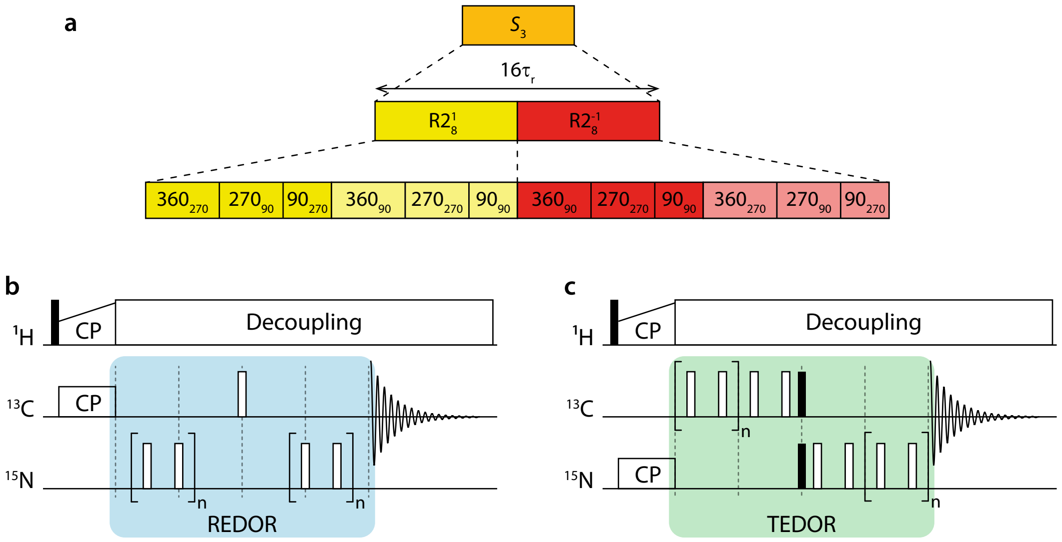

Figure 3.1: (a) Construction scheme of the S_3 pulse sequence.[101] (b-c) General pulse schemes for REDOR dephasing[105,106] (b) and TEDOR polarization transfer[103] (c) experiments. Filled and open rectangles represent $\pi/2$ and πpulses, respectively. Dotted vertical lines indicate the start of a rotor period.

π-pulses recouple the heteronuclear dipolar interaction, and the resulting dephasing of ^{13}C magnetization with increasing recoupling time is observed (S). An additional reference is usually recorded without application of ^{15}N pulses to account for signal decay which is not caused by ^{13}C$-$^{15}N dipolar couplings (S_0). The advantage of REDOR experiments is that the S/S_0 ratio is a direct measure of the recoupling efficiency, allowing very accurate distance measurements.[107–109]

For ^{13}C$-$^{15}N distance measurements in NA samples, however, the application of REDOR is practically impossible because the background signal of uncoupled spins is more than 100 times larger that that of dipolar coupled ^{13}C$-$^{15}N pairs.[103] Therefore, the dephasing caused by these couplings would most likely be within the noise of the experiment. For such situations, TEDOR (transferred-echo double-resonance) was developed to select the dipolar coupled spin pairs by a coherence transfer step.[103] The basic TEDOR sequence as shown in Figure 3.1c resembles the REDOR sequence in that two π-pulses per rotor period are applied to recouple the dipolar interaction. After a first recoupling period, $\pi/2$ pulses are applied simultaneously on both spin species, causing a coherence transfer from one spin species to the other (here from ^{15}N to ^{13}C), comparable to the INEPT transfer in solution-state NMR.[110] The sequence in Figure 3.1c is a basic example and more sophisticated implementations are usually used.[108]

Apart from enabling the selection of dipolar coupled ^{13}C$-$^{15}N spin pairs, TEDOR is also very well suited to ^{13}C$-$^{15}N distance measurements because it is very robust with respect to CSA and RF offsets and does not require continuous RF irradiation on ^{13}C or ^{15}N.[108] Its main drawback is signal decay due to transverse relaxation during the free evolution periods, caused primarily by heteronuclear dipolar couplings to the proton spins. Therefore, careful optimization of heteronuclear decoupling is required.

3.2 Cyclo-FF

All approaches for distance measurements in this chapter will be demonstrated on the cyclic diphenylalanine peptide (cyclo-FF) which self-assembles into nanotubes or nanowires (Figure 3.2a,b).[97,111] Cyclo-FF nanowires possess semiconducting properties and strong blue fluorescence,[111] and surface coating with cyclo-FF nanotubes can provide highly hydrophobic self-cleaning surfaces, ultra-capacitors for energy storage, and microfluidic chips.[97] Powder XRD studies on cyclo-FF nanowires[111] have shown that their structure is in good agreement with the single-crystal structure of cyclo-FF.[98] The main driving forces in the self-assembly process are hydrogen bonding between the backbone amides, and aromatic interactions between the phenyl rings, with both parallel and perpendicular π-stacking occurring.[98,111]

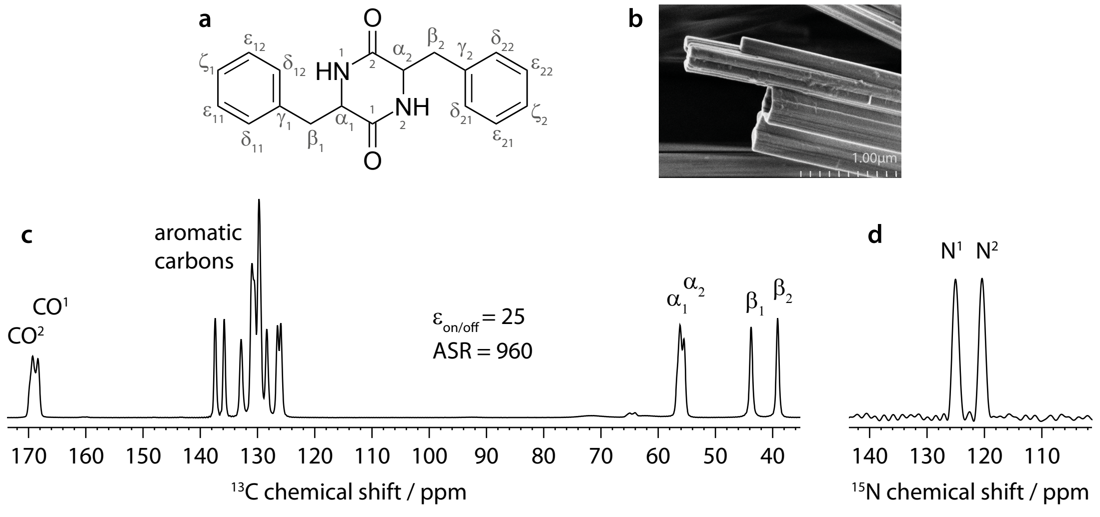

Figure 3.2: (a) Chemical structure of cyclo-FF. (b) Scanning electron microscopy image of cyclo-FF nanotubes. (c-d) DNP-enhanced ^{13}C and ^{15}N CPMAS spectra of cyclo-FF.

Takahashi *et al.* have introduced an efficient, matrix-free (MF) protocol for preparation of cyclo-FF for DNP.[40] It is a solution-based method where nanotubes are formed in the presence of the biradical polarizing agent. This protocol had to be developed because direct impregnation of cyclo-FF powder with a radical-containing solution does not lead to an efficient DNP process. On the sample prepared in this way, NA 2D ^{13}C$-^{13}$C correlation spectra were recorded, demonstrating among other things for the first time the feasibility of observing intermolecular contacts in NA samples.[40]

The cyclo-FF sample used for this work was prepared according to the MF protocol described above.[40] The only difference is that the previously employed polarizing agent (TOTAPOL[34]) was replaced by AMUPol[53] in order to improve the DNP efficiency.

The DNP-enhanced ^{13}C and ^{15}N CPMAS spectra of cyclo-FF prepared this way are shown in Figure 3.2c,d. The improved sample preparation results in a higher DNP enhancement ($\epsilon_{\text{on/off}} = 25$), and more importantly an increased ASR of 960 (see section 1.2.8) as compared to the sample used previously (8.8, and 390, respectively). The improved ASR signifies that experiments can be run six times faster than before, which was already five orders of magnitude faster than with conventional ssNMR.[40] Note that the ASR is very high in this case because of the long ^{1}H T$_1$ relaxation time of cyclo-FF at room temperature (RT, ^{1}H $T_1 > 600$ s).[40] Similar sensitivity under DNP conditions can in principle also be obtained on powdered samples with a smaller ASR, combined with a shorter ^{1}H T_1 at RT (e.g., ASR ≈ 10, ^{1}H $T_1 \approx 3\,$s).

The ^{13}C CPMAS spectrum is identical to the one reported by Takahashi *et al.*.[40] Notably, very narrow lines are obtained again, comparable to the dG(C3)$_2$ sample investigated in chapter 2. This indicates that the rigidity of self-assembled structures is generally beneficial for retaining good resolution at low temperatures. The carbons of the two phenylalanine residues have different chemical shift which is a consequence of intermolecular interactions like hydrogen bonding and π-stacking.[40] The ^{15}N CPMAS spectrum exhibits sharp lines, too, making it possible to resolve the two nitrogen signals. The high DNP efficiency of cyclo-FF in combination with the existing crystal structure make it a perfect sample to demonstrate and validate the approaches for distance measurements described above.

3.3 The 1D approach: Distances between carbonyl and aromatic carbons

3.3.1 Experimental results

The position of the aromatic rings with respect to the central diketopiperazine ring gives important information on the conformation of the cyclo-FF molecule. Probing distances from the two carbonyls to the aromatic carbons therefore constitutes an interesting application of the 1D approach as introduced in section 3.1.1. The isotropic chemical shifts of the carbonyls are well enough separated from the aromatics to allow the use of selective pulses. At the same time, both sets of resonances are within 5 kHz, which can be covered by the bandwidth of $[S_3]$.

The pulse sequence used in the experiment is shown in Figure 3.3a. After an initial CP step from DNP-enhanced protons to carbons, the CO magnetization is selectively flipped back to the z-axis from the transverse plane. During the following recoupling period, this magnetization is transferred to aromatic carbons, using the dipolar recoupling sequence $[S_3]$. After a selective readout pulse on the aromatics, their magnetization is detected.

This pulse sequence allows a straightforward measurement of polarization buildup on the aromatic carbons by following their signal intensity as a function of the incremented recoupling period. Due to the CO-selective excitation pulse (followed in addition by a selective saturation pulse on aromatics), no magnetization is present on the aromatics at the beginning of the recoupling period, and the use of DQ filtration becomes unnecessary. The selective pulse on the aromatics after recoupling ensures that the large magnetization of uncoupled CO spins remains along the z-axis. Consequently, it does not perturb the detection of the much smaller aromatic signals which also allows adapting the receiver gain to their low intensity. Overall, the 1D approach benefits from immensely decreased experimental times compared to the acquisition of DQ-filtered 2D spectra. In addition, data extraction by deconvolution and integration of 1D spectra is relatively straightforward.

A selection of 1D spectra acquired with the sequence of Figure 3.3a using different recoupling times (τ_{mix}) is presented in Figure 3.3b. The full dataset, consisting of 15 1D spectra, was recorded in ≈ 7 h, corresponding to only 28 min per spectrum. From each spectrum, the integrals of six peaks (Cγ_1, Cγ_2, Cδ_{21}, Cϵ_{22}, Cζ_1, Cζ_2) were extracted after deconvolution. The large central peaks ($128 - 126$ ppm) could not be reliably deconvoluted due to the contributions of too many carbons (Cδ_1, Cδ_{22},

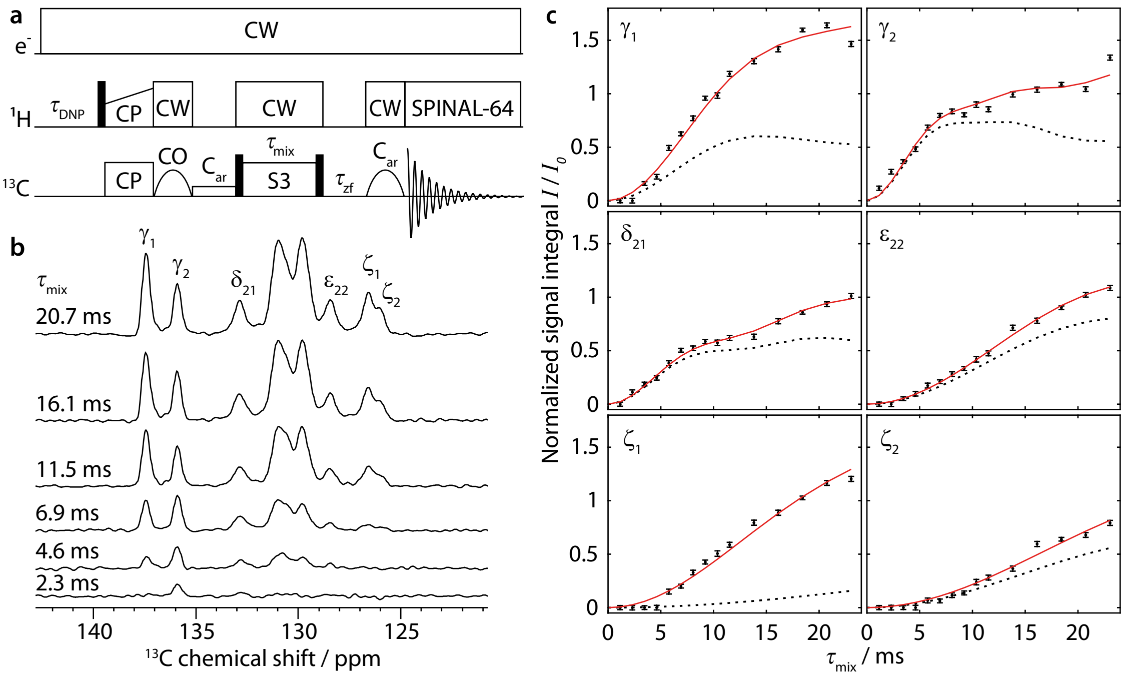

Figure 3.3: (a) Pulse sequence for the 1D approach, used to obtain buildup curves for polarization transfer from carbonyl to aromatic carbons. [S_3] is employed as the dipolar recoupling sequence, with the $\pi/2$ bracketing pulses indicated as black bars on the ^{13}C channel. The recoupling time (τ_{mix}) is incremented to record the buildup curves. (b) Aromatic region of selected 1D spectra, recorded on cyclo-FF with the pulse sequence shown in (a) using different recoupling times as indicated in the Figure. (c) Full experimental polarization buildups (black points) for the six peaks labeled in (b). Error bars denote the average noise integral over 2 ppm. Red solid and black dotted lines show SPINEVOLUTION simulations[112] of the buildups based on the cyclo-FF crystal structure,[98] respectively taking into account all distances up to 7 Å (red) or intramolecular distances only (black). The simulated curves are fitted to experimental points with an amplitude factor A (see Table 3.1). Note that the experimental signal integral (I) is normalized with respect to the initial polarization of CO spins (I_0) in such a way that the initial available polarization in a particular ^{13}CO$-^{13}$C$_{\text{aromatic}}$ spin pair is 1 (more details in section 3.8).

Cϵ_1, and Cϵ_{21}).

Figure 3.3c shows the resulting polarization buildup curves for the six peaks (black points). They are normalized with respect to the initial polarization on the carbonyls, taking into account the number of COs per molecule and the fraction of them which is coupled to another ^{13}C spin (1.1 %, see section 3.8 for more details). As a result, the y-axes in Figure 3.3c reflect the absolute transferred polarization and can thus be directly compared to numerical simulations.

All buildup curves display polarization transfer efficiencies far above the expected maximum for a single spin pair under these conditions ($\approx$ 0.38 in numerical simulations). This is a clear indicator that various spin pairs contribute additively to each buildup curve. For instance, both CO^1 and CO^2 can provide polarization because they are excited simultaneously. Thus, two different intramolecular polarization transfer pathways are possible for each peak, and the sum of their contributions can give rise to a maximum polarization of ≈ 0.76. This number is still exceeded in the majority of cases, which indicates that intermolecular distances contribute as well (discussed in more detail in section 3.3.3).

The six experimental buildup curves possess distinctly different features. For instance, while most peaks build up continuously, the Cγ_2 and Cδ_{21} signal intensities slightly level out before rising again. Moreover, the Cγ_2 peak has a faster initial buildup, most probably indicating the presence of a very short CO-Cγ_2 distance compared to all other distance contributions here. The Cγ_1 peak, on the other hand, has a slower initial buildup, but rises to higher intensity at longer mixing times, suggesting a higher total number of distances involved in the buildup.

The reason for the additive contribution of distances to the buildup curves lies in the NA nature of the sample (see also section 1.3.3). Nearly all ^{13}C$-^{13}$C spin pairs are isolated (surrounded by ^{12}C), such that the polarization transfer between them is not detrimentally affected by the presence of a third ^{13}C spin, even over longer distances. In addition, all different kinds of spin pairs are randomly distributed in the sample. Each spin pair leads to a typical polarization buildup depending on the internuclear distance, and it is the addition of these individual contributions that yields the experimentally observed buildups. Similar observations have been reported by Brouwer *et al.* in the process of structure determination of zeolites, where they probed the slightly more abundant ^{29}Si spins.[113,114]

Overall, the buildup curves contain a high level of information. As described above, some qualitative information is already accessible from a relative comparison between the different curves. However, the extraction of quantitative distance information requires the use of numerical simulations for comparison and fitting.

3.3.2 Numerical simulations

In order to relate the experimental polarization buildup curves to the crystal structure and evaluate their consistency, the expected polarization buildups were simulated numerically with SPINEVOLUTION,[112] taking into account the known distances from the crystal structure of cyclo-FF.[98]

As a first step, the behavior of $[S_3]$ under the experimental conditions employed here was investigated in more detail. This was necessary because the large CSAs of aromatic carbons (up to ≈ 20 kHz at 9.4 T) faced a comparably slow spinning frequency of 13.889 kHz which does not comply with the recommended regime for the

$[S_3]$ sequence ($\omega_r \geq 1.5\omega_{\mathrm{CSA}}$).[102] Numerical simulations showed that polarization can still be transferred efficiently with $[S_3]$ (and also S_3) under the experimental conditions employed here. However, the buildup curves for $[S_3]$ exhibit a strong dependency on all CSA parameters. More precisely, the asymmetry and anisotropy affect the overall polarization transfer amplitude, without having a major influence on the shape of the curve. On the other hand, a change of the orientation of the principal axis of the CSA tensor can change this shape significantly. To run accurate simulations, the magnitudes and orientations of the ^{13}C CSA tensors of cyclo-FF were computed with the gauge-including projector-augmented wave (GIPAW)[72] approach, using its implementation in the Quantum ESPRESSO[115] software package. The crystal structure of cyclo-FF[98] served as the initial input for the DFT calculations, and hydrogen atom positions were optimized before the GIPAW calculations.

The expected polarization buildups were then simulated with SPINEVOLUTION, based on the CSA tensor parameters from the DFT computations, atomic positions from the crystal structure, and isotropic chemical shifts from experiment. The polarization buildups for all relevant spin pairs were simulated separately, and the individual curves were then co-added for each peak. It is important to stress again that, although several different distances contribute to each buildup curve, we consider these contributions to be coming from isolated spin pairs. Deviations from this approximation by the presence of a third spin leading to dipolar truncation at NA will be discussed in section 3.3.4.

Notably, this concept of data analysis differs from those employed previously in similar contexts of ^{13}C$-$^{13}C[41] or ^{29}Si-^{29}Si[114] recoupling experiments at NA, which rely on analytical functions to describe polarization transfers. We instead chose to use numerical simulations, since they can easily account for, among other things, isotropic and anisotropic chemical shift effects.

3.3.3 Intra- and intermolecular contributions

In a first approximation, the experimental data was compared to simulated buildup curves that take into account only intramolecular spin pairs. These intramolecular distances are underlined in Table 3.1, and the corresponding simulations are shown as dotted lines in Figure 3.3c. Each simulated curve represents the sum of two contributions, as in our case polarization transfer to an aromatic carbon can originate from CO^1 or CO^2. The intramolecular distances are generally the shortest distance contributions to the experimental buildup curves, except for the Cζ_1 peak.

Table 3.1: Distances from CO^1 and CO^2 in cyclo-FF to surrounding aromatic carbons up to a limit of 7 Å.[98]

	$C\gamma_1$	$C\gamma_2$	$C\delta_{21}$	$C\epsilon_{22}$	$C\zeta_1$	$C\zeta_2$
Distances from CO^1 / $Å^a$	$\underline{3.8}$	$\underline{3.7}$	$\underline{4.6}$	$\underline{4.5}$	4.3	$\underline{5.3}$
	4.9	6.0	5.9		5.1	6.9
	5.3	6.5			$\underline{6.5}$	
	5.5				6.8	
					6.9	
Distances from CO^2 / $Å^a$	$\underline{4.2}$	$\underline{3.0}$	$\underline{3.3}$	$\underline{5.0}$	4.9	$\underline{5.1}$
	4.2	5.3	6.5	5.5	5.4	6.3
	6.5		6.7		$\underline{6.4}$	6.8
					6.5	
					6.5	
Total number of distances	7	5	5	3	10	5
A^b	0.88	1.14	0.91	1.15	0.73	0.97
RMSD	0.07	0.06	0.03	0.02	0.05	0.04

a. Intramolecular distances are underlined. *b.* Factor for scaling the amplitude of the simulated curves to experimental data as used in Figure 3.3c, obtained by minimizing the root mean square deviation (RMSD) between experiment and simulation.

Consequently, the initial polarization buildups are mainly determined by those, as evident from Figure 3.3c. At the same time, however, all experimental buildups deviate from the simulations at longer mixing times, which highlights the contribution of intermolecular contacts.

The extent of this deviation can be rationalized by the number and magnitude of intermolecular distances, which are listed up to a limit of 7 Å in Table 3.1. For example, the experimental data for the $C\gamma_1$ peak starts to deviate significantly from the simulation for intramolecular distances at mixing times as short as ≈ 6 ms, and rises to more than three times the simulated intensity. This can be explained by the high number of comparably short intermolecular distances (four distances ≤ 5.5 Å). The $C\zeta_1$ buildup shows an even more drastic deviation, which results from the fact that the intramolecular distances here are very long (6.4 and 6.5 Å) compared to other distances. The buildup curve of $C\zeta_1$ is therefore almost exclusively determined by intermolecular spin pairs. Deviations between intramolecular simulations and experimental data are less pronounced for the other four peaks, since there the intramolecular spin pairs represent the two shortest distance contributions, separated from the next longer ones by at least 0.5 Å.

This comparison shows that the inclusion of intermolecular spin pairs into the simulation is essential for a thorough explanation of the polarization buildup curves. To obtain more accurate simulated curves, all distances in Table 3.1 were taken into account. The amplitudes of the calculated curves were adjusted to the experimental points by fitting an individual amplitude factor A for each curve ($I_{\text{exp}} = A \cdot I_{\text{sim}}$). The results of the full simulations, including scaling by A, are shown as red lines in Figure 3.3c. The optimized amplitude factors A with corresponding RMSD values are summarized in Table 3.1.

The full simulation is in excellent agreement with the experimental data. Notably, no systematic deviation at longer mixing time is observed, which would have indicated relaxation-related losses during the recoupling. Even small features like the changes in slope for Cγ_2 and Cδ_{21} are reproduced by simulation. Furthermore, all amplitude scaling factors lie between 0.7 and 1.2, which is reasonably close to the theoretically expected value of 1 (see also next section). This indicates that it is indeed possible to directly relate experimental data to the polarization transfer efficiency. This constitutes a big advantage, as precious information on the approximate number of distances contributing to a buildup curve can be extracted. Furthermore, the fact that the experiments are clearly sensitive to intermolecular contacts is highly encouraging, as these are imperative for supramolecular structure elucidation.

3.3.4 Dipolar truncation effects at NA

In order to investigate the origin of the small deviations of A from unity reported in Table 3.1, we simulated buildup curves which take into account the cumulative contribution of all ^{13}C$-$^{13}C spin pairs falling below increasing cutoff distances from 4 Å to 20 Å. These simulations are shown as dashed lines in Figure 3.4 without any scaling ($A = 1.0$) in order to allow direct comparison to experimental points. For the considered range of mixing times (up to 25 ms), the simulated buildup curves keep rising to higher intensities upon the inclusion of longer distances up to ≈ 14 Å. This appears surprising since the polarization transfer under $[S_3]$ for a single 14 Å distance within 25 ms recoupling time is negligibly small. However, the number of possible spin pairs at such long internuclear distances becomes so high that their cumulative contribution gets significant (e.g. for cyclo-FF there are about 30−40 different spin pairs whose distances lie between 10 and 14 Å for a total of 60−70 distances below 14 Å).

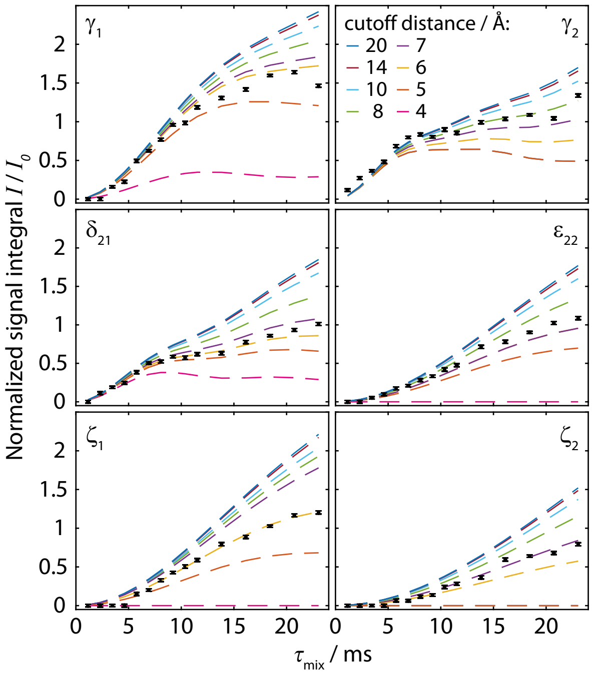

Figure 3.4: Simulated polarization buildup curves (dashed lines) for the experiment shown in Figure 3.3, taking into account the cumulative contribution of all spin pairs whose internuclear distances lie below a cutoff distance increased from 4 Å to 20 Å. The y-axis corresponds to the absolute transferred polarization, and no scaling has been applied to the simulated curves. Experimental points (black points) are identical to those given in Figure 3.3c, including normalization with respect to the CO polarization.

A reevaluation of potential dipolar truncation effects at NA of ^{13}C becomes necessary when considering the possibility of observing such long distance polarization transfers. To this end, we need to estimate the probability of finding a third ^{13}C spin in a defined volume around the respective ^{13}C—^{13}C two-spin system, which is demarcated by their internuclear distance. At NA of ^{13}C, this probability is $n_{\mathrm{C}} \cdot 1.1\%$, with n_{C} being the number of carbon atoms in the considered volume. Accordingly, the polarization transfer efficiency is expected to be lowered by this percentage. The effect increases with the number of atoms in the volume, and thus with the internuclear distance for the considered polarization transfer. Hence, no polarization transfer can statistically be observed between two spins which are at such a distance that the corresponding volume around the spin pair contains 91 carbons or more, as there will always be a third ^{13}C spin truncating the desired transfer. An exact definition of the "truncating" volume is beyond the scope of this thesis, and this crude model also does not consider cases in which polarization transfer is only partially truncated. Nevertheless, from the crystal structure of cyclo-FF, the limit of ≈ 100 carbon atoms is found within a sphere of radius 8 Å. It is therefore very unlikely that polarization transfers over this distance can be observed in cyclo-FF, even with considerably longer mixing times. This illustrates the limits of the idealized two-spin system model used here to rationalize polarization transfer in NA samples.

These considerations also raise the question whether the choice of a cutoff distance of 7 Å is reasonable. In order to assess this problem, simulations for all $^{13}C{-}^{13}C$ spin pairs up to different cutoff distance were summed up and fitted to the experimental data with the amplitude factor A. Figure 3.5 reports the minimized RMSD (red) as well as the corresponding A values (black solid line) and their deviation from unity ($|1 - A|$, black dotted line) obtained for cutoff distances between 3 and 15 Å.

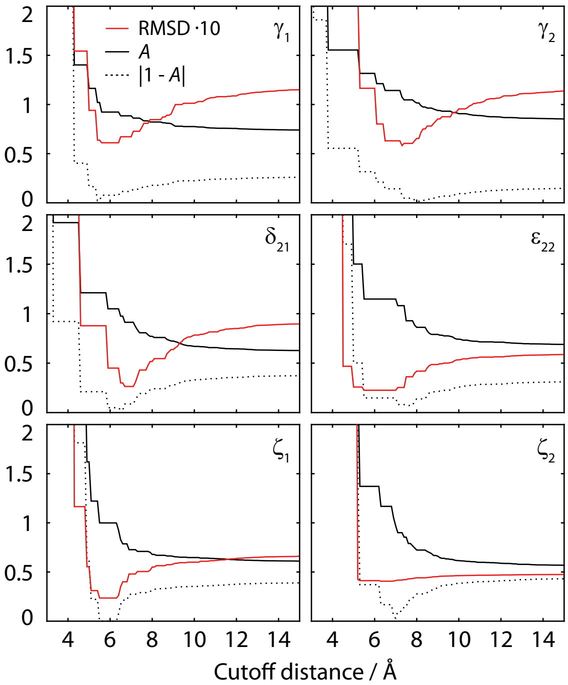

Figure 3.5: Quality of the fit of simulated buildup curves to experimental data from the 1D approach (see Figure 3.3), depending on the maximum distance (cutoff distance) included in the simulations. For these plots, simulations for all relevant spin pairs with distances up to the respective cutoff distance were summed up and fitted to the experimental data with the amplitude factor A by minimizing the RMSD between experiment and simulation. The corresponding RMSD (red solid line) and A value (black solid line) are plotted here depending on the cutoff distance.

Starting from 3 Å and upon inclusion of longer distances, the RMSD first decreases significantly until it reaches a minimum and then increases again. Similarly, the A value decreases from a value much larger than 1 to a value smaller than 1. Interestingly, the RMSD and the $|1 - A|$ curves reach a minimum at roughly the same cutoff distance for a given peak, meaning that the lowest RMSD does coincide with an A value very close to 1. This is a remarkable observation and demonstrates that the experimental data (including its normalization) can be reproduced very well by simulation. In addition, the increase of the RMSD with longer cutoff distances can indeed be understood as the influence of dipolar truncation, confirming the considerations above.

The exact positions of RMSD minima depend on the peak and occur at a cutoff distance between 5.5 and 7.5 Å. This confirms our assumption that the experiments are sensitive to long distances ($>$ 4.5 Å), and that they therefore have to be included in simulations. At the same time, too long distances cannot be observed due to dipolar truncation. The slightly different positions of the minima in the six cases analyzed here can be explained by the different numbers and lengths of contributing distances. When considering spin pairs at distances between 5 and 7 Å, some of them are in proximity of a third ^{13}C spin and hence the polarization transfer is affected by dipolar truncation, whereas others are still isolated. Therefore, such distances do still contribute to the buildup curves, but with a lowered intensity. Depending on how many distances fall in this category, the "optimum" cutoff distance can change, and the corresponding A value may not be exactly unity.

Overall, these simulations justify our way of treating and fitting the experimental data. 7 Å is a reasonable choice for a cutoff distance, since the RMSD minima lie around this value (Figure 3.5), and most experimental points lie in between the corresponding simulated buildup curves with 6 and 8 Å cutoff distance (Figure 3.4). The occurrence of slightly different "optimum" cutoff distances justifies the determination of different A values for each peak. This factor, which should theoretically be unity, takes into account spin-pair-dependent deviations owing to some longer distance transfers, partial dipolar truncation, and the influence of experimental errors and/or instabilities. In the case of cyclo-FF, our fitting procedure exclusively returns amplitude factors close to 1 (see Table 3.1), which confirms the validity of our approach. Notably, this approach differs from other reported fitting procedures which use a global amplitude factor for all buildup curves.[41,114]

It should be mentioned that slightly different fitting procedures would also be possible. A cutoff distance different from 7 Å ($\approx \pm 1$ Å) could also be chosen and would still lead to good fitting results. Alternatively, the A value could be set to 1.0 and the cutoff distance could be fitted to obtain the minimum RMSD. This procedure would lead to good results, too, and has been applied for evaluation of structural models presented in chapter 4.

3.4 The 1D approach: Distances between aliphatic carbons

3.4.1 Experimental results

The previous section has demonstrated the use of the 1D approach for probing distances between carbonyl and aromatic carbons. The short experimental times and high accuracy of this approach make it very attractive and therefore its applicability to other spin pairs was tested as well. Looking at the CPMAS spectrum of cyclo-FF (Figure 3.2c), the aliphatic carbons should be another suitable target for the approach, involving selective excitation of either Cβ_1 or Cβ_2.

The pulse sequence used for this experiment is shown in Figure 3.6a and is very similar to the one used in the previous section (Figure 3.3a). It only differs in that the selective flip-up pulse is centered on Cβ_1 or Cβ_2, and that the readout pulse is a hard pulse. $[S_3]$ is again used as dipolar recoupling sequence. Select spectra obtained by exciting Cβ_1 or Cβ_2 are shown in Figure 3.6b and c, respectively.

A complicating aspect of this experiment is that the aliphatic resonances are fairly close to each other, making the use of selective pulses more challenging. Still, it was possible to selectively flip back one or the other Cβ (peak maxima $\approx$ 460 Hz apart). This required the application of very long Gaussian shaped pulses (15 ms, corresponding to 116.5 Hz bandwidth) accompanied by efficient heteronuclear decoupling (SW$_f$-TPPM[22]). The length of these selective pulses led to $\approx$ 40 % loss of Cβ magnetization. Moreover, it restricted the maximum recoupling time to 20 ms because of the high RF power levels required for proton decoupling during selective pulse, recoupling and acquisition. Nevertheless, the mere possibility of selectively exciting such a narrow bandwidth is very encouraging regarding the applicability of the 1D approach to samples with crowded spectra. Moreover, selective excitation of only one resonance means that there will be only one origin of polarization transfer, enabling more precise analysis of buildup curves as compared to those obtained from exciting two COs together in section 3.3.

Another consequence of probing such a narrow region of the spectrum is that no selective readout pulse can be reasonably applied. Instead, a hard pulse has been used, resulting in the signal of the previously flipped up carbon dominating the spectrum, as it can be seen in Figure 3.6b,c. This means that the receiver gain cannot be set to be optimal for the small recoupled signals.

Taking a closer look at the spectra in Figure 3.6b,c, the first observation is that

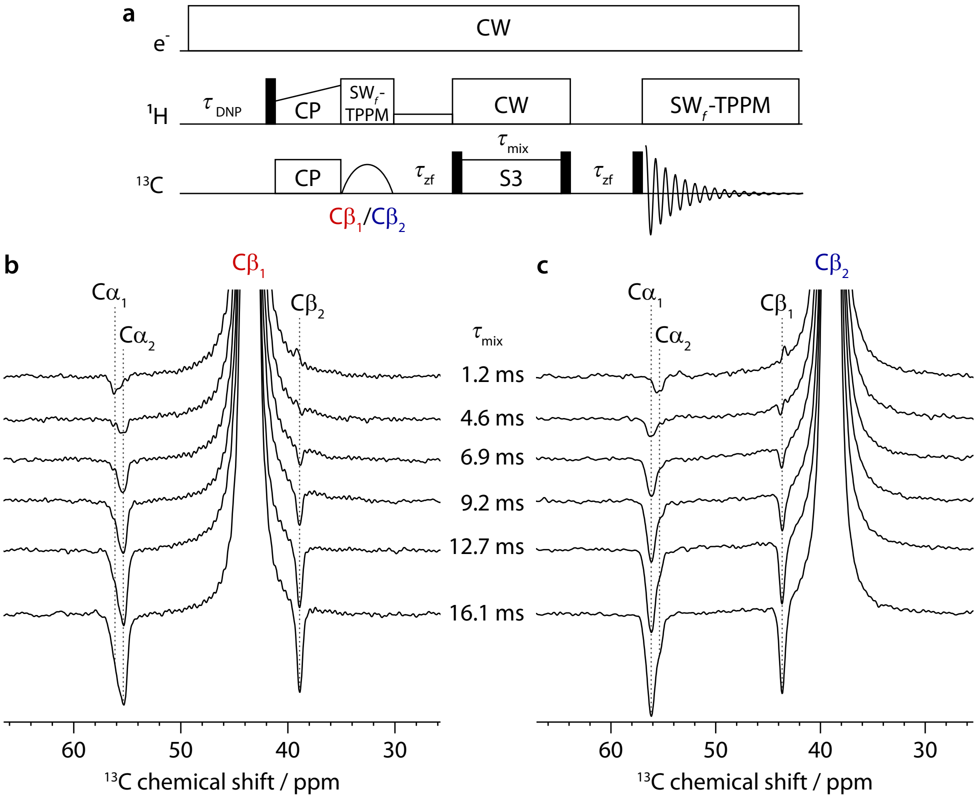

Figure 3.6: (a) Pulse sequence for recording buildup curves of polarization transfer from Cβ_1 or Cβ_2 to other aliphatic carbons, following the 1D approach. The shaped pulse selects either the Cβ_1 or the Cβ_2 resonance. (b-c) Aliphatic regions of selected 1D spectra, recorded on cyclo-FF with the pulse sequence shown in (a) and the selective pulse centered on either Cβ_1 (b) or Cβ_2 (c). Each spectrum was recorded in $\approx$28 min.

the signals originating from polarization transfer and the signal of the initially excited Cβ spins are of opposite sign, as it is expected for DQ recoupling experiments.[116] A nice "buildup" of these negative signals with increasing recoupling time can be observed. Before focusing on their analysis with respect to the crystal structure of cyclol-FF, two additional observations regarding the signals of the Cα spins should be mentioned.

As expected for the shortest mixing time, only one Cα can be observed at $\tau_{\text{mix}} =$ 1.2 ms. This Cα is the one which is directly bonded to the excited Cβ, i.e. Cβ_1−Cα_1 in Figure 3.6b and Cβ_2−Cα_2 in Figure 3.6c. However, at the next longer mixing time (4.6 ms), this signal is much less intense and only starts building up slowly again when the mixing time increases further. This is the only time that signal decay is observed in the spectra for the 1D approach presented in this thesis. It suggests that different dynamics are active for the recoupling of a one-bond spin pair as compared to spin pairs at a longer distance. One contribution is the one-bond J-coupling which is expected to be $\approx 35\,\mathrm{Hz}$ here.[12] It modulates the recoupling efficiency, but the $^1J_{\mathrm{CC}}$-coupling alone does not explain this rapid decay. It can therefore be concluded that the one-bond ^{13}C$-$^{13}C spin pairs are subject to an additional rapid decay of DQ coherences, causing the one-bond peak to disappear almost completely. This decay may be caused by cross-terms involving the comparably large ^{13}C$-$^{13}C dipolar coupling of a one-bond distance and, for example, the dipolar coupling to a ^{14}N or a ^{1}H spin.

The second observation is that all Cα signals are broadened or even show a slight splitting, especially at short mixing times. This phenomenon does not only occur for peaks originating from one-bond polarization transfer, meaning that it cannot result from $^1J_{\mathrm{CC}}$-couplings alone. The source of the broadening can therefore be identified with high probability as the quadrupolar moment of the neighbouring ^{14}N spins because of which the ^{13}C$-$^{14}N dipolar interaction is not completely averaged.[117,118] Such broadening can usually be observed at magnetic fields up to $\approx 10\,\mathrm{T}$.[118] Indeed, it is also observed here for CO and Cα resonances in the CPMAS spectrum of cyclo-FF. The intensity ratio of the split signals is approximately 2:1, as expected in such a case.[117,118] On the other hand, no such splitting is observed for the other carbons which are not directly connected to the amide nitrogens. Similarly, one-bond ^{15}N$-$^{13}C correlation peaks in the 2D TEDOR spectra presented later in this chapter (Figure 3.11) do not exhibit any splitting either because the detected carbon is bonded to a ^{15}N nucleus. The modified peak shapes have been taken into account during signal deconvolution and should not have a pronounced effect on the data analysis.

3.4.2 Fitting of experimental data

For analysis of the experimental data, peak integrals were extracted by deconvolution and scaled with respect to the initial polarization on Cβ_1 or Cβ_2, in analogy to the procedure in section 3.3. They are shown as black points in Figure 3.7. Since the buildup of transferred polarization between the Cβs can be extracted from both sets of experiments (C$\beta_1$$-C\beta_2$ from Figure 3.6b and C$\beta_2$$-C\beta_1$ from Figure 3.6c), the average of both is shown in Figure 3.7.

Following the same procedure as described in the previous section, the expected buildup curves for each contributing distance up to 7 Å (see Table 3.2) were simulated separately with SPINEVOLUTION. An advantage of recoupling the aliphatic carbons is that their CSA is much smaller than that of aromatic carbons, lead-

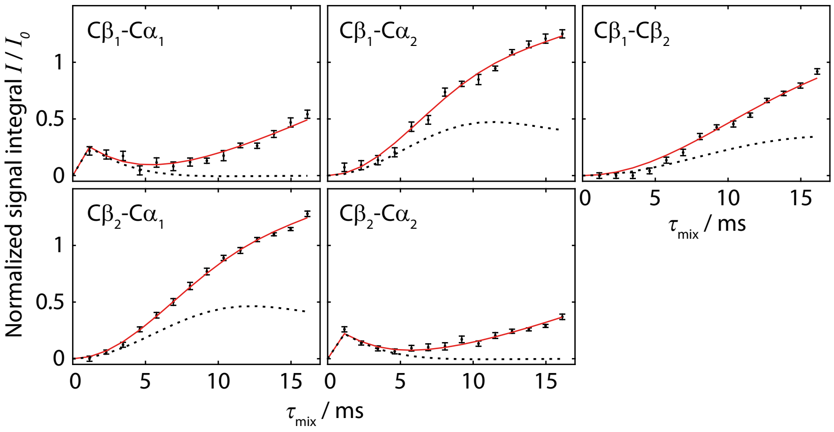

Figure 3.7: Full experimental polarization buildups (black points) for the aliphatic-aliphatic recoupling experiments as shown in Figure 3.6. Error bars denote the average noise integral over 3 ppm. Red solid lines show SPINEVOLUTION simulations of the buildups based on the cyclo-FF crystal structure, taking into account all distances up to 7 Å. The simulated curves are fitted to experimental points with an amplitude factor A and an additional exponential decay factor for the one bond distances in $C\beta_1{-}C\alpha_1$ and $C\beta_2{-}C\alpha_2$ only (see Table 3.2). The experimental signal integral (I) is normalized with respect to the initial polarization of the $C\beta_1$ or $C\beta_2$ spins (I_0) in the same way as described in section 3.3.

ing to only marginal dependence of the buildup curves on CSA tensor orientation. Therefore, the literature values for phenylalanine ($\sigma_{\text{aniso}}(C\alpha) = 27\,\text{ppm}$ and $\sigma_{\text{aniso}}(C\beta) = -45\,\text{ppm}$)[99] were used for simulation instead of the values computed with DFT-GIPAW. The simulated buildup curves were summed up and fitted to the experimental values with an amplitude factor A.

A small modification to the fitting procedure had to be made for the buildups containing one-bond distances ($C\beta_1{-}C\alpha_1$ and $C\beta_2{-}C\alpha_2$). In order to account for the experimentally observed decay (see section 3.4.1), the simulation of polarization transfer over one bond included a $^1J_{\text{CC}}$-coupling of 35 Hz and was multiplied by an exponential decay function with time constant τ_{decay}. For fitting of the $C\beta_1{-}C\alpha_1$ and $C\beta_2{-}C\alpha_2$ simulated buildup curves to the experimental data, the following equation was used

$$I_{\text{exp}}(\tau_{\text{mix}}) = A\left(I_{\text{sim}}(\tau_{\text{mix}},1)\exp\left[-\tau_{\text{mix}}/\tau_{\text{decay}}\right] + \sum_{i=2\ldots i_{\max}} I_{\text{sim}}(\tau_{\text{mix}},i)\right), \qquad (3.2)$$

where $i = 1, 2, \ldots i_{\max}$ denotes the i-th contributing distance with $i = 1$ being the one-bond distance (1.6 Å). Accordingly, $I_{\text{sim}}(\tau_{\text{mix}}, i)$ denotes the intensity of the simulation for the i-th distance at mixing time τ_{mix}. A and τ_{decay} were optimized together in the fitting procedure.

Table 3.2: Distances from Cβ_1 and Cβ_2 to neighboring aliphatic carbons up to a limit of 7 Å.[98]

	Cβ_1−Cα_1	Cβ_1−Cα_2	Cβ_2−Cα_1	Cβ_2−Cα_2	Cβ_1−Cβ_2
Distances / Å^a	$\underline{1.6}^c$	$\underline{3.9}$	$\underline{4.0}$	$\underline{1.6}^c$	$\underline{4.5}$
	6.2	5.0	5.1	6.1	5.9
	6.2	5.1	5.2	6.6	5.9
	6.5	6.7	6.9	6.7	6.1
	6.5		7.0	6.9	
Total number of distances	5	4	5	5	4
A^b	1.06	0.93	0.91	1.11	0.89
RMSD	0.03	0.04	0.02	0.05	0.02

a. Intramolecular distances are underlined. *b.* Factor for scaling the amplitude of the simulated curves to experimental data as used in Figure 3.7, obtained by minimizing the RMSD between experiment and simulation. *c.* For fitting, the one-bond distance has been simulated with a J-coupling ($^1J_{CC} = 35$ Hz) and multiplied by an exponential decay with a time constant of 4.2 ms.

The A and RMSD values determined with this fitting procedure are summarized in Table 3.2. τ_{decay} was found to be $\approx$4.2 ms. The simulated buildup curves multiplied by A (and by the exponential decay function, where applicable) are shown as solid red lines in Figure 3.7. In addition, simulations which only take into account the intramolecular distances are sown as dotted lines, analogous to Figure 3.3.

Based on the fitting results and the plots, very similar conclusions to those of the experiments on carbonyl and aromatic carbons in section 3.3 can be drawn: The buildup curves corresponding to the full simulation rise to considerably higher intensity compared to the curves simulated for the intramolecular distance contribution only, demonstrating that these experiments too are sensitive to intermolecular contacts. In this context, the buildup curves for the Cβ_1−Cα_1 and Cβ_2−Cα_2 spin pairs are an extreme case, being almost exclusively determined by intermolecular distance contributions at longer mixing times, owing to the fast decay of the one-bond distance contribution. Overall, a very good agreement between experiment and simulation is obtained, with the A value being close to 1. No significant relaxation is observed at longer mixing times (except for one-bond distances), which facilitates the detection of long distances and simplifies the fitting procedure. The experiments shown in this section therefore represent another successful application of the 1D approach, underlining its high accuracy for distance measurements between different carbon species.

3.5 The 2D approach: Distances between aromatic carbons

3.5.1 Aromatic-aromatic 2D correlation spectra

Probing aromatic-aromatic interactions is of high interest since π-stacking is an important non-covalent interaction in supramolecular structure formation. In addition, aromatic moieties often constitute the main functional part of molecular assemblies, owing to the possibilities of energy and charge transport through their π-systems.[119–122] Numerous ssNMR studies have been discussed in the literature which rely on probing the aromatic proton spins.[123,124] This section will show an alternative approach based on the observation of π-stacking through ^{13}C$-$^{13}C correlation spectra. As the aromatic carbons only span a small chemical shift range ($\approx$ 15 ppm), distance measurements among them do require the 2D approach.

Accordingly, ^{13}C$-$^{13}C DQ-filtered DQ-SQ correlation spectra of cyclo-FF were recorded, focusing specifically on the aromatic region. Owing to its excellent CSA compensating properties, S_3 was employed as the dipolar recoupling sequence. Figure 3.8 shows two of the spectra obtained, using total recoupling times of 2.3 ms (a) and 13.8 ms (b). Nicely resolved correlations among aromatic carbons are observed, highlighting the excellent performance of S_3 for recoupling carbons with large CSA. The spectra presented here are the first ^{13}C$-$^{13}C dipolar correlation spectra showing such well-resolved correlations between aromatic carbons.

The spectrum in Figure 3.8a was acquired with the shortest possible mixing time, using one S_3 block for DQ excitation and reconversion each (2.3 ms in total), and contains mainly one-bond correlations. It can thus be used for complete assignment of all aromatic resonances as illustrated in the Figure. In addition, correlation peaks of lower intensity can be observed, which arise from polarization transfers over distances corresponding to two or three bonds within one phenyl ring. The assignment shows that the δ_1 and ϵ_1 resonances of one phenyl ring overlap whereas they are resolved for the second ring (δ_{21}, δ_{22}, ϵ_{21}, and ϵ_{22}). The up- and downfield shifts of ϵ_{22} and δ_{21}, respectively, are signs of intermolecular interactions, in this case of parallel π-stacking.[40,98]

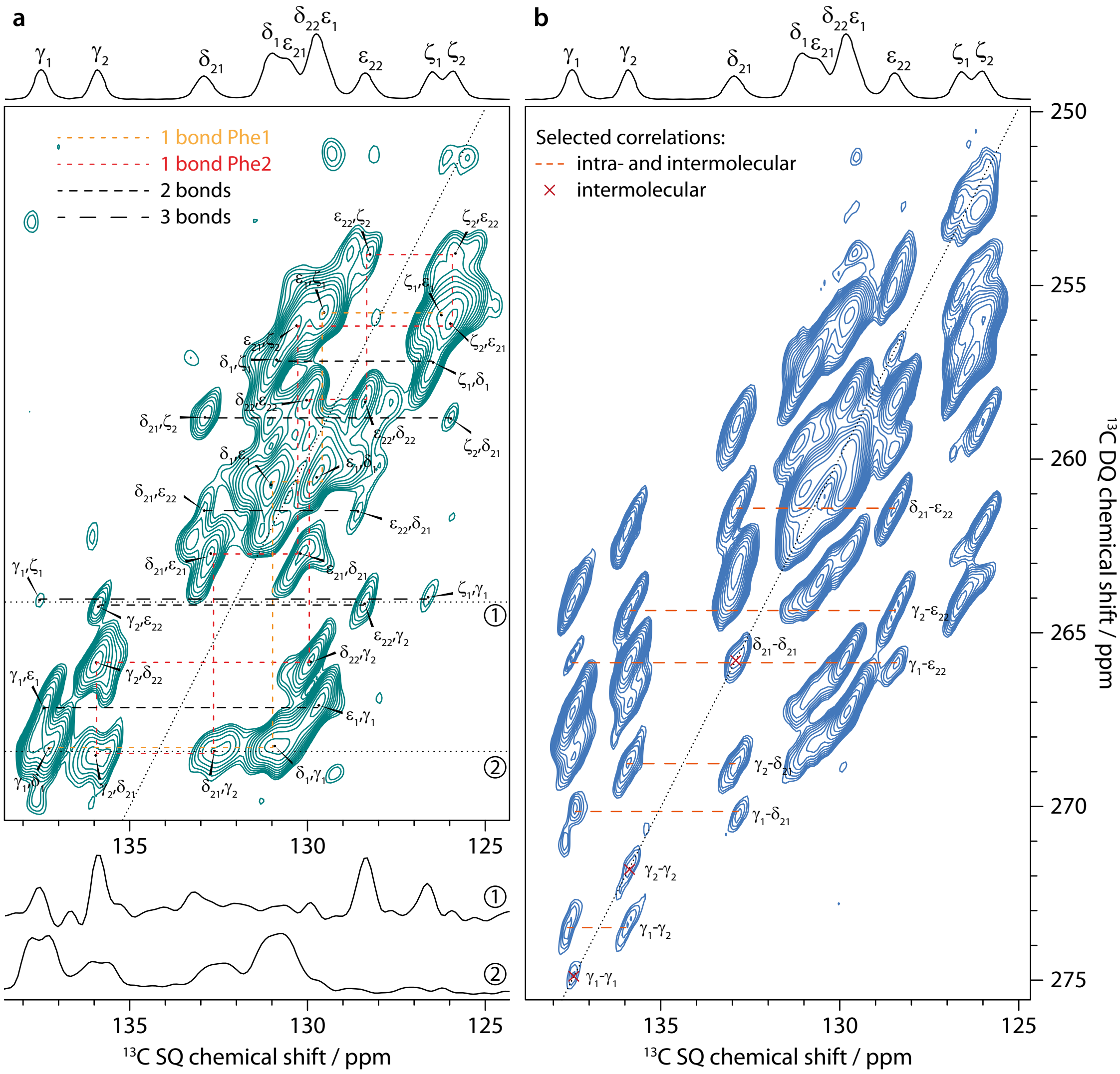

Figure 3.8: Aromatic region of ^{13}C$-$^{13}C DQ-SQ correlation spectra of cyclo-FF, obtained with the dipolar recoupling sequence S_3 applied during total recoupling times (DQ excitation plus reconversion) of 2.3 ms (a) and 13.8 ms (b). The spectra were recorded in $\approx$18.5 h (a) and $\approx$7.4 h (b), respectively. ^{13}C CPMAS spectra are shown above for illustrative purposes. Cross sections along the black dotted lines ($\delta_{\mathrm{DQ}} = 264.1$ ppm and $\delta_{\mathrm{DQ}} = 268.5$ ppm) in (a) are displayed below and show the narrowing of linewidths for long distance peaks (upper cross section, linewidths 40$-$50 Hz) compared to cross-peaks arising from directly bonded carbons (lower cross section, linewidths $>$100 Hz). Resolved cross-peaks used for the buildup analysis (see Figure 3.9a) are labeled in (b). Among them, pure intermolecular peaks are marked by a red cross, and peaks resulting from intra- and intermolecular contributions are connected with an orange dashed line.

The spectrum acquired with longer mixing time (13.8 ms, Figure 3.8b) looks remarkably different from the previous one. Numerous additional peaks can be observed, e.g. between the Cγ resonances. They arise from long distance correlations, occurring between carbons from different phenyl rings. Notably, the C$\gamma_1$$-C\gamma_1$ cross-peak demonstrates that polarization transfers over distances of more than 6 Å can

Table 3.3: Distances between selected aromatic carbons up to a limit of 7 Å.[98]

	Cγ_1-C$\gamma_1{}^a$	Cγ_1-Cγ_2	Cγ_1-Cδ_{21}	Cγ_1-Cϵ_{22}	Cγ_2-C$\gamma_2{}^a$	Cγ_2-Cδ_{21}	Cγ_2-Cϵ_{22}	Cδ_{21}-C$\delta_{21}{}^a$	Cδ_{21}-Cϵ_{22}
Distances /	6.2	$\underline{4.9}$	$\underline{4.7}$	$\underline{4.7}$	4.5	$\underline{1.4}$	$\underline{2.4}$	3.5	$\underline{2.8}$
Å^b	6.2	6.2	6.0	5.2	6.2	4.2	4.5	6.2	4.2
	6.6	6.6	6.4	5.4	6.2	5.0	5.5	6.2	4.7
		6.8		5.8		6.4	6.7		5.7
		6.9							
Total number of distances per molecule^c	1.5	5	3	4	1.5	4	4	1.5	4
A^d	1.55	1.45	1.37	0.61	1.61	0.78	0.98	1.08	0.93
RMSD	0.06	0.09	0.09	0.09	0.05	0.04	0.08	0.04	0.13

a. Intermolecular autocorrelation peaks. *b.* Intramolecular distances are underlined. *c.* Distances in autocorrelation peaks are counted half for each molecule because they are "shared" between two molecules. *d.* Factor for scaling the amplitude of the simulated curves to experimental data as used in Figure 3.9, obtained by minimizing the RMSD between experiment and simulation.

be observed, as the shortest distance between two Cγ_1 atoms is 6.2 Å (see Table 3.3). Moreover, this peak is one of several autocorrelation cross-peaks appearing on the DQ diagonal. As a DQ filter was implemented in the pulse sequence, they have to originate exclusively from intermolecular correlations, which makes them particularly valuable for the investigation of the supramolecular assembly.

Another striking difference between the two spectra in Figure 3.8 is a splitting of some cross-peaks along the direct detection dimension, which is only observed at short mixing time. This splitting occurs for correlation peaks that correspond to a one-bond contact, and is caused by the $^1J_{\mathrm{CC}}$-coupling between the two directly bonded carbons. Since the size of the $^1J_{\mathrm{CC}}$-coupling (55-60 Hz for monosubstituted benzenes[125]) is similar to the peak linewidths (40-60 Hz), it is barely resolved and constitutes the limiting factor for resolution. It results in considerable line broadening and reduced signal-to-noise ratios for one-bond cross-peaks. In NA samples, correlation peaks over longer distances are sharper (see cross sections in Figure 3.8a) since the detected carbons mostly do not have a directly bonded ^{13}C spin and the size of two-bond and longer-range J_{CC}-couplings is negligible compared to the ^{13}C linewidths obtained here. At the same time, peaks which are split at short mixing time appear also sharper at longer mixing times (e.g. the Cγ_1-Cδ_{21} correlation), as contributions of spin pairs with longer internuclear distances (and therefore free of $^1J_{\mathrm{CC}}$-coupling) are becoming active. They benefit from increased signal-to-noise ratios and readily dominate the spectrum.

3.5.2 Observation of π-stacking

For the investigation of π-stacking interactions, buildup curves for polarization transfer between aromatic carbons are required. For this purpose, a series of ten DQ-filtered DQ-SQ correlation spectra was recorded in the same manner as the spectrum in Figure 3.8b, using ten different recoupling times. Peak volumes for nine isolated correlation pairs (labeled in Figure 3.8b) were then extracted with Monte-Carlo volume integration[126] after shearing of the spectra (see section 3.8 for more details).

These experimental points (black points) along with the simulated polarization buildup curves (red solid lines) are shown in Figure 3.9 for the different spin pairs. In order to normalize the experimental data, the $\mathrm{C}\gamma_2{-}\mathrm{C}\epsilon_{22}$ and $\mathrm{C}\epsilon_{22}{-}\mathrm{C}\gamma_2$ cross-peaks at the first point of the buildup were used as reference points ($\tau_{\mathrm{mix}} = 4.6\,\mathrm{ms}$). They have the advantage of being free of one-bond J-coupling, and their summed volume ($V_1 + V_2$) corresponds to a two-bond distance transfer, which can be compared to the simulated expected transfer efficiency (S). The ratio $S/\left(V_1 + V_2\right)$ was then taken as the normalization factor for all integrated intensities. Notably, this procedure can be done without knowledge of the crystal structure, because the length of a two-bond distance in a phenyl ring is well-known.

Similar observations as in the 1D approach can be made for the buildup curves obtained from 2D spectra, with notably the contribution of multiple distances resulting in higher transferred intensities than the theoretical maximum for a single spin pair (≈ 0.21). Several correlations have contributions from distances shorter than $3\,\mathrm{\AA}$, originating from spin pairs within one phenyl ring ($\mathrm{C}\gamma_2{-}\mathrm{C}\delta_{21}$, $\mathrm{C}\gamma_2{-}\mathrm{C}\epsilon_{22}$, and $\mathrm{C}\delta_{21}{-}\mathrm{C}\epsilon_{22}$). Accordingly, their buildup curves start with high intensity at the first point (reflecting a fast initial buildup), whereas the transferred polarization for all other correlations is significantly lower at such a short mixing time.

For a better evaluation of the experimental data, full simulations of the expected polarization buildup curves were run with SPINEVOLUTION, in the same manner as for the 1D buildup curves. Accordingly, distances up to $7\,\mathrm{\AA}$ were taken into account (summarized in Table 3.3). As for the 1D approach, the simulated data was fitted to the experimental points with an amplitude factor A. Good agreement be-

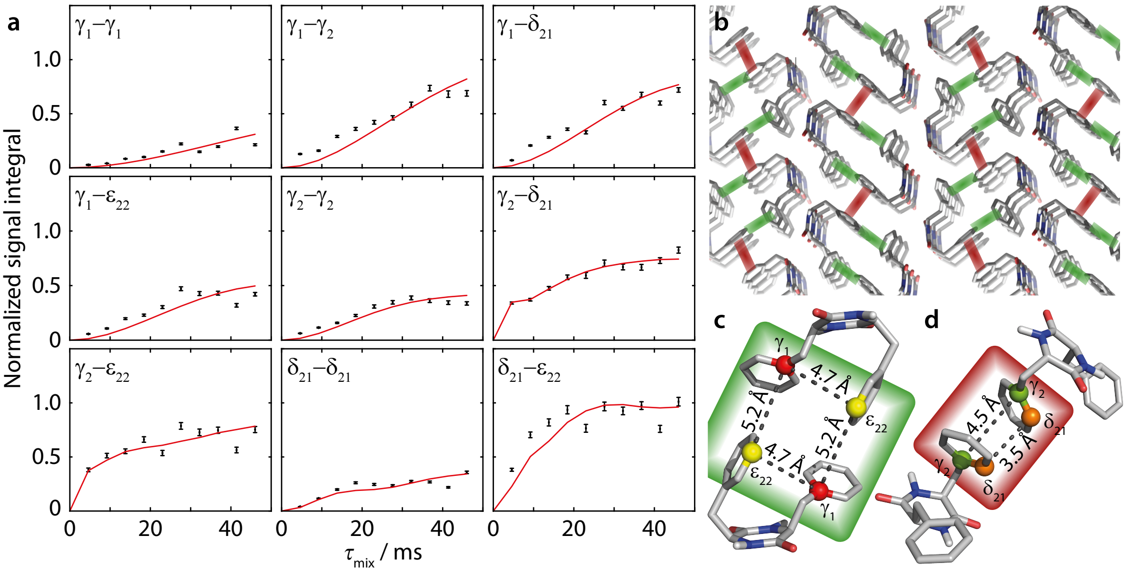

Figure 3.9: (a) Normalized experimental (black points) and simulated (red lines) polarization buildup curves for aromatic-aromatic spin pairs in DQ-SQ correlation spectra. Experimental points were obtained from Monte-Carlo integration of nine different cross-peak pairs as shown in Figure 3.8b for ten mixing times ranging from 4.6 ms to 46 ms. Error bars indicate the error in volume extraction using the Monte-Carlo method.[126] Normalization of the experimental points is explained in the text. The simulated curves take into account all distances up to 7 Å and are fitted to experimental points with an amplitude factor A (see Table 3.3). (b) Crystal structure of cyclo-FF[98] with perpendicular and parallel π-π interactions highlighted in green and red, respectively. (c-d) Close-up of perpendicular (c) and parallel (d) π-stacking. The highlighted distances can be probed by the 2D experiments presented in this section. Note that the relevant carbon atoms and distances are highlighted for illustrational purposes on the same pair of cyclo-FF molecules. However in a sample at NA, it is highly unlikely to have four ^{13}C isotopes occurring in only two cyclo-FF molecules. The highlighted distances contribute individually to the polarization transfer in different molecule pairs across the sample.

tween experiment and simulation is again obtained. The more complex nature of 2D experiments leads however to a lower accuracy when compared to the 1D approach, as revealed by higher RMSDs and larger deviations from unity for the amplitude factor A (see Table 3.3). This can be explained by the possibility of a direct normalization of 1D spectral intensities as well as by the simpler signal integration of 1D peaks. Moreover, the acquisition of the complete set of 2D spectra requires several days and is hence more susceptible to spectrometer instabilities.

Nevertheless, these experiments constitute a powerful approach for the investigation of π-stacking. It is clearly possible to observe correlations that arise from structurally important π-π interactions, which are illustrated in Figure 3.9b. For instance, the parallel π-stacking in cyclo-FF (Figure 3.9d) is well described by the $C\gamma_2-C\gamma_2$ and the $C\delta_{21}-C\delta_{21}$ polarization buildup curves. Indeed, the distances describing this interaction are by far the shortest contributions and therefore dominate the buildup curves. For the perpendicular π-stacking, the involved $C\gamma_1{-}C\epsilon_{22}$ distances are illustrated in Figure 3.9c, with the shortest distance being intramolecular (4.7 Å) and the next longer distance (5.2 Å) arising from the π-π interaction. This second example illustrates the strength and the challenges of these experiments. They are clearly sensitive to π-π contacts and can be used to probe π-stacking. On the other hand, however, it is challenging to distinguish the "relevant" π-π contacts from other contributions like intramolecular distances. In this respect, peaks on the diagonal are particularly interesting as they do not contain intramolecular contributions.

3.6 Heteronuclear distance measurements: Carbon-nitrogen distances

3.6.1 The TEDOR pulse sequence

As described in section 3.1.2, TEDOR was chosen for heteronuclear dipolar recoupling owing to its relatively low power requirements and high robustness. A 2D implementation was chosen here in order to resolve the signals of the two nitrogen atoms of cyclo-FF (Figure 3.2d). The corresponding pulse sequence is shown in Figure 3.10. It is based on the 3D z-filtered TEDOR sequence which was developed for experiments on uniformly ^{13}C,^{15}N-labeled samples, with the third dimension being the incremented recoupling time.[127]

After CP from proton to carbon, ^{13}C spins evolve under a spin echo while REDOR pulses (two π-pulses per rotor period) are applied on the nitrogen channel. During this period, anti-phase coherence is created: $I_x \rightarrow I_x + 2I_yS_z \sin(\omega_{IS}\tau_{mix}/2)$, where I, S, and ω_{IS} represent carbon and nitrogen spins, respectively, and the dipolar coupling between them. Next, a 90°_x pulse on the carbon channel creates I_zS_z magnetization. The remaining transverse magnetization (I_x) is left to decay during the following z-filter period, aided by proton irradiation at the rotary resonance condition ($\omega_1 = \omega_r$). Nitrogen magnetization is then flipped into the transverse plane, evolves during t_1 and is flipped back along z. In order to maintain rotor synchronization of the sequence, a short delay δ is then inserted whose length depends on the length of t_1. Next, the carbon magnetization is flipped into the transverse plane again and another REDOR period follows, identical to the one in the beginning of the sequence. This reconverts the I_yS_z anti-phase coherence into carbon in-phase coherence I_x which is detected after another z-filter period.

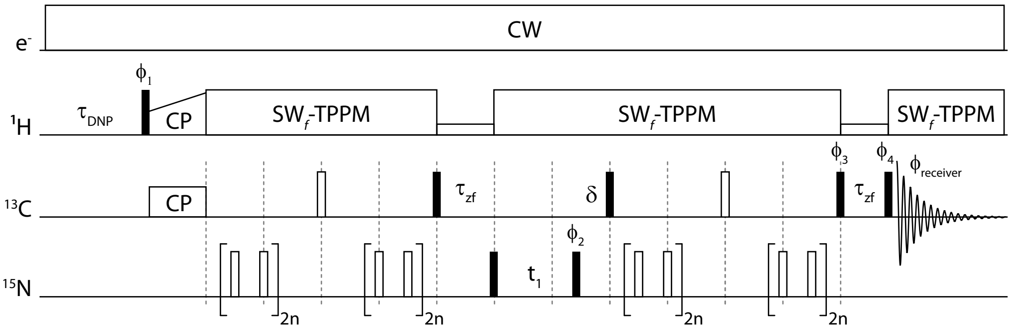

Figure 3.10: Pulse sequence used for the acquisition of 2D TEDOR spectra.[127] Filled and open rectangles represent $\pi/2$ and π-pulses, respectively. Vertical dashed lines indicate the beginning of a rotor period. The length of δ is adjusted depending on the length of t_1 in order to preserve rotor synchronization in case of non-rotor-synchronized t_1 evolution. During the z-filter periods (τ_{zf}), low-power irradiation on the proton channel is applied at the rotary resonance condition ($\omega_1 = \omega_r$) to achieve more efficient dephasing of transverse carbon magnetization. The number of π-pulses on the nitrogen channel is incremented ($n = 1, 2, 3, ...$) to increase the mixing time τ_{mix}. Phase cycling:[127] $\phi_1 = 16\times(1)\ 16\times(3)$; $\phi_2 = 31$; $\phi_3 = 1133$; $\phi_4 = 1111\ 2222\ 3333\ 0000$; $\phi_{\mathrm{receiver}} = 3113\ 0220\ 1331\ 2002\ 1331\ 2002\ 3113\ 0220$, where $1 = \mathrm{y}$, $2 = -\mathrm{x}$, $3 = -\mathrm{y}$, $4 = -\mathrm{x}$. π-pulses on the nitrogen channel were phase cycled according to the xy-16 scheme.[128]

During the REDOR periods, efficient heteronuclear proton decoupling is crucial for minimizing T_2'-relaxation-related losses, especially over long recoupling times. SW$_f$-TPPM[22] was found to be the most efficient decoupling sequence in the present case.

The z-filtered TEDOR sequence was developed for uniformly ^{13}C,^{15}N-enriched biomolecules where ^{13}C$-$^{13}C J-couplings lead to phase-distorted cross-peaks when no z-filters are applied.[127] In NA samples, J_{CC}-couplings can be safely neglected as the vast majority of ^{13}C spins is not directly bonded to another ^{13}C spin. On the other hand, one has to ensure the suppression of signals from ^{13}C spins without dipolar coupling to a ^{15}N spin. Phase cycling of the second 90° pulse on ^{15}N, selecting a coherence change of ± 1, ensures that only coherences which have passed through nitrogen are detected. While this should in theory be sufficient, additional precautions have been taken because the signal which has to be suppressed is several magnitudes larger than the desired signal. Therefore, the first z-filter was set to be long enough ($\approx 2\,\mathrm{ms}$) to allow complete decay of transverse magnetization, which is primarily that of uncoupled ^{13}C spins. No loss of z-magnetization was observed during the z-filter. The second z-filter is less crucial for experiments at NA of ^{13}C and ^{15}N, but is kept to allow, e.g., the decay of remaining anti-phase magnetization.

3.6.2 Experimental results

Figure 3.11 shows three examples of 2D TEDOR spectra of cyclo-FF which were recorded with the pulse sequence in Figure 3.10. The first spectrum (a) was recorded with a short recoupling time of 1.33 ms. Accordingly, only correlations over one bond between each nitrogen and its neighbouring Cα and CO spins are observed. This enables assignment of the two nitrogen peaks to N^1 and N^2. With a longer mixing time of 5.33 ms (spectrum (b)), correlations corresponding to two-bond distances become visible, too. This comprises correlations with the respective second Cα and CO as well as correlations with one of the Cβs, namely $N^1{-}C\beta_1$ and $N^2{-}C\beta_2$. At the very long mixing time of 17.33 ms (spectrum (c)), a multitude of cross-peaks is observed: Correlations of both nitrogens with all Cβs, Cαs, Cγs, and COs are observed, as well as correlations with some δ and ϵ carbons.

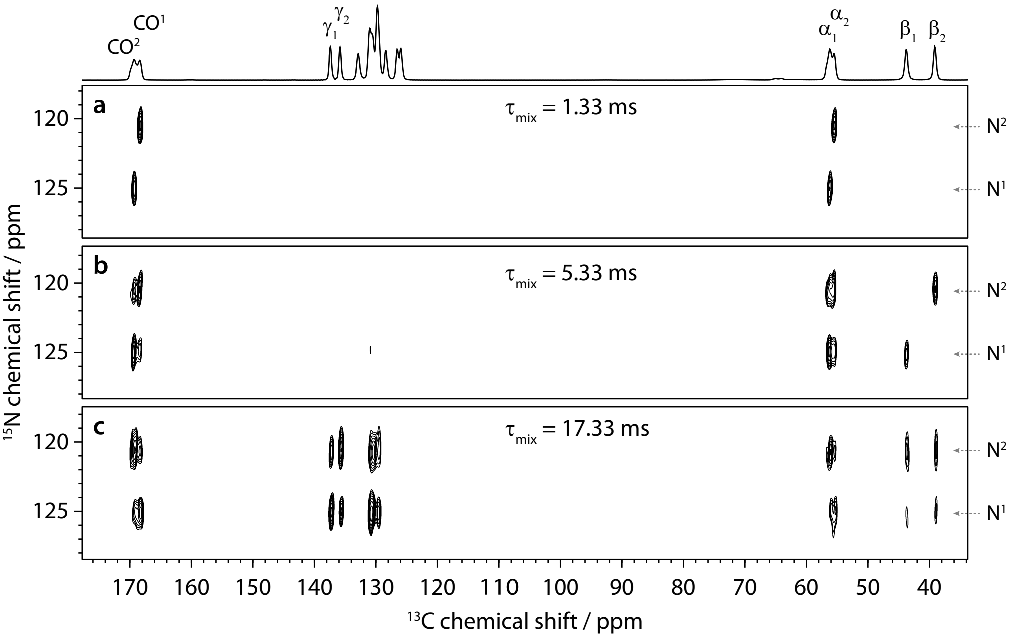

Figure 3.11: 2D TEDOR spectra of cyclo-FF, obtained with the pulse sequence in Figure 3.11, using mixing times (τ_{mix}) of 1.33 ms (a), 5.33 ms (b), and 17.33 ms (c). Each spectrum was acquired in ≈ 3 h 45 min. The same contour levels are shown for all spectra. A ^{13}C CPMAS spectrum is shown above for illustrative purposes.

The acquisition of each 2D spectrum took only ≈ 3 h 45 min which is truly remarkable for an organic sample at NA. These short experimental times were possible in part because the two nitrogen resonances lie within 5 ppm and require only a small number of t_1 increments to be resolved. Overall, 22 spectra were recorded with mixing times between 0.67 ms and 18.67 ms. The number of cross-peaks obtained and their very good resolution shows that the TEDOR sequence is well suited for ^{13}C$-$^{15}N recoupling experiments at NA.

For data extraction, projections along the F_2 dimension were calculated for the N^1 and N^2 correlation peaks, and the signals from CO, Cγ_1, Cγ_2, Cδ_{21}, Cα, Cβ_1, and Cβ_2 were integrated. No deconvolution of the CO and Cα signals was attempted. The integrals were normalized by the following two factors which account for varying CP efficiency and help to estimate the polarization transfer efficiency:

Each cross-peak integral was first scaled individually with respect to the average of the corresponding signal integrals in ^{13}C CPMAS spectra which were recorded before and after the respective 2D spectrum. This procedure was particularly important because slight detuning of the probe was observed over the course of the experiments, resulting in a loss of CP signal intensity of up to 10 %. The scaling with respect to CPMAS efficiency accommodates this change in efficiency, but is unfortunately not sufficient to estimate its impact on the recoupling efficiency. This leads to larger fluctuations in the experimental data than normally expected, as it can be seen in Figure 3.12.

In order to estimate the absolute polarization transfer efficiency, a procedure similar to the one for the 2D approach (section 3.5) was then applied, where intensities of cross peaks corresponding to a known distance were scaled with respect to the expected transfer efficiency. In section 3.5.2, a two-bond ^{13}C$-$^{13}C distance was chosen for this purpose. For the TEDOR experiments presented here, the first three points of the buildup curves for N^1$-$CO, N^2$-$CO, N^1$-$Cα, and N^2$-$Cα were taken into account. They correspond to the buildup of a one-bond distance, without experiencing significant contribution from two-bond distances, as verified from simulation and experimental data. The expected polarization transfer was determined by numerical simulations with SPINEVOLUTION. A scaling factor for each point was determined, and their average was then used to scale all experimental points. The resulting experimental buildup curves are shown as black points in Figure 3.12, with the y-axis corresponding to the estimated polarization transfer efficiency.

The experimental buildup curves do reflect the geometry of the cyclo-FF molecule and the observations that were already made for the three spectra shown in Figure 3.11. N$-$Cα and N$-$CO buildup curves rise very fast and to very high intensities. This is an expected result owing to the contribution of two carbon species and hence numerous distances, in particular a one-bond and a two-bond distance (see also Table 3.4). The buildup curves which have contributions from a two-bond distance (N^1$-$Cβ_1 and N^2$-$Cβ_2) reach a maximum within 8 ms and show a slight os-

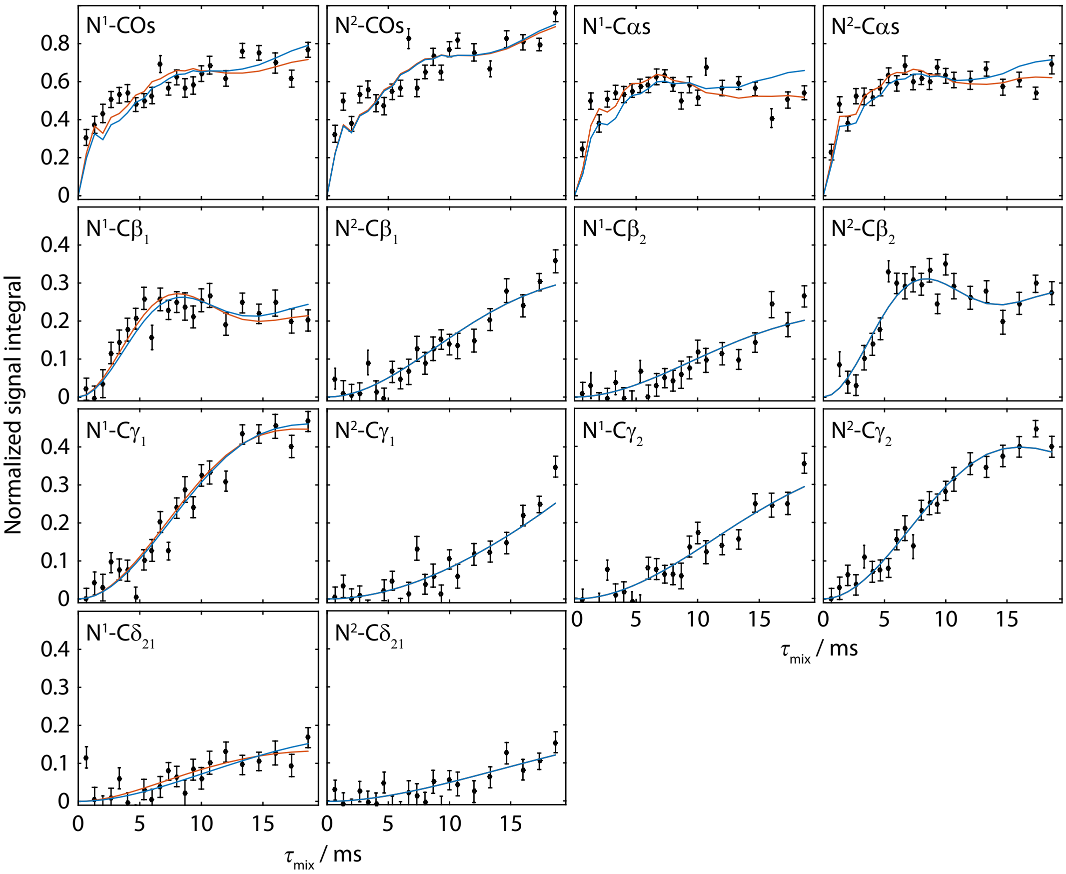

Figure 3.12: Experimental polarization buildup (black points) of ^{13}C$-$^{15}N cross peaks (see Figure 3.11), obtained with the TEDOR pulse sequence in Figure 3.10. Error bars indicate the average noise integral over spectral regions of the same range as the integrated signals (1.4$-$3.2 ppm). Blue and red lines represent the expected polarization buildup curves based on the crystal structure of cyclo-FF, taking into account distances up to 6 Å. They were fitted to the experimental data by an amplitude factor A only (blue lines) or by an amplitude factor and an exponential decay function (red lines).

cillation after that. This shows that the influence of the next-longer distance ($>$ 5 Å, see Table 3.4) is rather small, which distinguishes these buildups from the ^{13}C$-$^{13}C buildup curves presented before.

3.6.3 Fitting of experimental data

The comparison of experimental data to simulation was performed in a similar way as described for the ^{13}C$-$^{13}C distance measurements in this chapter. Accordingly, the expected polarization buildup curves were simulated separately for each contributing distance up to 6 Å (Table 3.4) and then summed up. Simulations were run with SPINEVOLUTION, using isotropic chemical shifts from experiment and CSA parameters for phenylalanine from literature.[99,129] The use of these literature

Table 3.4: Distances from N^1 and N^2 to relevant carbons as shown in Figure 3.12 up to a limit of 6 Å.[98]

	COs	Cαs	Cβ_1	Cβ_2	Cγ_1	Cγ_2	Cδ_{21}
Distances from N^1 / Å^a	$\underline{1.3}$	$\underline{1.5}$	$\underline{2.5}$	$\underline{3.5}$	$\underline{3.1}$	$\underline{3.6}$	$\underline{3.8}$
	$\underline{2.5}$	$\underline{2.4}$	5.2	5.1	4.6	5.6	
	3.7	4.5	5.3	5.5			
	4.7	5.1					
		5.1					
		5.2					
A^b	0.63	0.67	0.63	0.53	0.89	0.77	0.74
RMSD	0.078	0.084	0.031	0.031	0.023	0.029	0.021
Distances from N^2 / Å^a	$\underline{1.3}$	$\underline{1.4}$	$\underline{3.4}$	$\underline{2.5}$	$\underline{4.8}$	$\underline{3.1}$	$\underline{4.2}$
	$\underline{2.5}$	$\underline{2.4}$	4.6	5.5	4.9		5.5
	3.8	4.4	5.8	5.8	5.1		
	4.4	5.2	5.9		5.6		
		5.2					
		5.3					
		5.5					
A^b	0.71	0.71	0.66	0.75	0.87	0.97	0.73
RMSD	0.074	0.064	0.027	0.032	0.023	0.021	0.022

a. Intramolecular distances are underlined. *b.* Factor for scaling the amplitude of the simulated curves to experimental data as used in the blue curves in Figure 3.12, obtained by minimizing the RMSD between experiment and simulation.

values was sufficient due to the negligible dependence of the TEDOR recoupling efficiency on CSA tensor orientations. This property would also allow the use of Bessel functions for calculating polarization buildup curves.[127,130]

Since the TEDOR experiments involve long spin echoes for ^{13}C, the experimental signal intensities are affected by T_2'-decay. Therefore, the ^{13}C signal decay under an echo sequence was measured in a separate experiment. The signal intensities of the relevant peaks after different echo lengths are shown in Figure 3.13. Their decay is best described as a bi-exponential curve with one fast and one slowly relaxing component (see solid lines in Figure 3.13) and can be regarded as the minimum expected relaxation in the TEDOR experiments.[127] In order to take this into account, the simulated expected buildup curves were multiplied by the bi-exponential decay functions used to fit the spin echo decay curves in Figure 3.13.

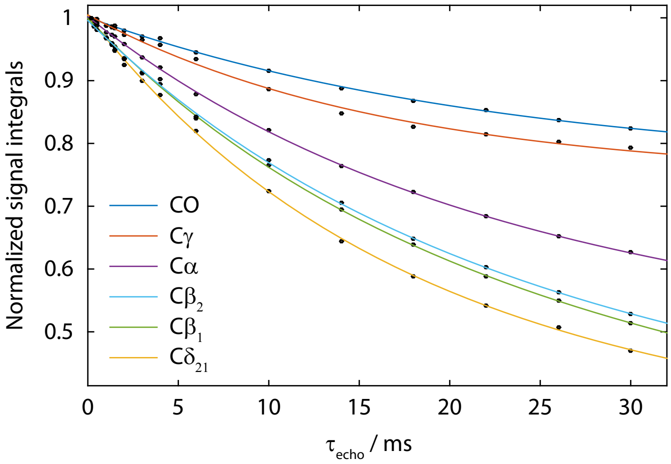

Figure 3.13: Experimental decay of ^{13}C magnetization of cyclo-FF under a spin echo of length τ_{echo} (black dots) and fit with a bi-exponential decay function (solid lines). Heteronuclear decoupling was applied during the echo with the same parameters as used during the recoupling periods of the TEDOR experiments (SW$_f$-TPPM[22] at ≈100 kHz RF field strength).

Note that the actual T_2'-relaxation parameters can only be obtained with great uncertainty from the plot in Figure 3.13 because the experimental data was only measured up to 30 ms echo time whereas the time constant of the slowly decaying component appears to be substantially longer than 100 ms. Still, the solid lines in Figure 3.13 model the T_2'-decay over 30 ms very well. This is sufficient for the analysis of the TEDOR experiments presented here since the longest mixing time employed was 18.67 ms.

Two methods were compared for fitting the simulated curves to the experimental data. The first method is identical to the one used for ^{13}C$-$^{13}C distance measurements, meaning that the simulated buildup curves were scaled by an amplitude factor A to minimize the RMSD between simulation and experiment. The A and RMSD values obtained in this way are summarized in Table 3.4, and the resulting curves are shown as blue lines in Figure 3.12. For the second method, a second fit parameter was used in addition to A to evaluate the influence of additional relaxation. This was tested because decay rates reported in literature are often faster than the T_2'-relaxation alone.[127] To see whether this is the case here as well, the simulated curves, already scaled by T_2'-relaxation, were multiplied by A and an exponential decay function $\exp(-\tau_{\text{mix}}/\tau_{\text{decay}})$, where A and τ_{decay} were optimized by minimizing the RMSD between experiment and simulation. The resulting simulated buildup curves are shown as red lines in Figure 3.12.

Good agreement between experiment and simulation is obtained again. Multiplication by an additional decay function does not lead to substantially improved fits except for the N−Cα buildup curves where decay time constants of $\approx$40 ms (N^1−Cαs) and $\approx$63 ms (N^2−Cαs) are found. These buildup curves differ from the others in that they have at least six contributing distances shorter than 6 Å compared to maximum four distances in that category for all other curves (Table 3.4). This is a rather exceptional case and it may be concluded that fitting with an A value alone is generally sufficient for the experiments shown here. The A values obtained this way span a relatively narrow range of values between 0.53 and 0.97 (Table 3.4), demonstrating the good data quality. The fact that they are all smaller than 1 may indicate decreased recoupling efficiency owing to experimental imperfections. Comparable amplitude factors between 0.5 and 1 have also been reported for uniformly ^{13}C,^{15}N-labeled systems.[127]

The fitting of experimental ^{13}C−^{15}N buildup curves recorded at NA is considerably easier than in a uniformly ^{13}C,^{15}N-labeled sample. These isotopically enriched samples require a set of equations for fitting the buildup of each cross peak, accommodating ^{13}C−^{13}C J-couplings and “passive” dipolar couplings to other ^{15}N spins, resulting in a precision of approximately $\pm 10 - 20\%$.[127] Most of this uncertainty stems from the simplifications used in the model, which neglects the relative orientations of the different ^{13}C−^{15}N dipolar coupling tensors.[127] Neither ^{13}C−^{13}C J-couplings nor dipolar couplings to other ^{15}N spins are generally an issue in samples at NA, which is why a much simpler model can be used for data fitting.

The data shown here confirms that ^{13}C−^{15}N buildup curves are generally more sensitive to shorter (intramolecular) distances. This can for example be used to probe the molecular conformation which will be demonstrated in the following chapter. Most buildup curves do however also experience contributions from intermolecular distances (see Table 3.4) which is essential for supramolecular structure determination. Overall, ^{13}C−^{15}N buildup curves recorded at NA do constitute another valuable source of structural information.

3.7 Conclusions

This chapter has presented dipolar recoupling experiments for recording polarization buildup curves and measuring distances in organic solids at NA of ^{13}C and ^{15}N, using MAS-DNP to compensate for their very low sensitivity. Two approaches for ^{13}C−^{13}C distance measurements were shown and one approach for ^{13}C−^{15}N distance measurements, both along with experimental demonstration.

The first approach for homonuclear distance measurements is the “1D approach” in which selective pulses are used to enable the acquisition of polarization buildup curves from a series of 1D spectra. This makes experiments very fast and a set of six polarization buildup curves was obtained in only 7 h. Another important advantage of the 1D approach is that the magnitude of starting polarization can be determined with good accuracy. It can then be used to scale the intensity of the experimental points in a way that they reflect the actual transferred polarization. This allows direct comparison to numerical simulations, providing a valuable additional constraint for fitting procedures. The main limitation of the 1D approach is the applicability of selective pulses which require a sufficiently large separation between peaks.

The “2D approach” is the second procedure presented for homonuclear distance measurements. It refers to the more traditional approach of recording 2D DQ-SQ correlation spectra, applying DQ filtration for selecting dipolar coupled spin pairs only. The acquisition of two-dimensional spectra makes it more time consuming (7 h per 2D spectrum here), but does allow probing distances between close-by resonances where selective pulses cannot be applied. For instance, π-stacking contacts can be detected through carbon-carbon correlation spectra, as shown here.

For both homonuclear approaches, the S_3 and $[S_3]$ pulse sequences have proven extremely valuable. Their high robustness enables efficient recoupling, even involving carbons with large CSA, and their low RF power requirements allow the use of long recoupling times for probing small dipolar couplings. Heteronuclear decoupling can also be applied very efficiently because proton decoupling fields more than ten times larger than the carbon recoupling field can be used. No relaxation is generally observed in the buildup curves acquired with S_3 or $[S_3]$, which facilitates the observation of long distances and also the fitting procedures. Currently, the main drawback associated with S_3 and $[S_3]$ is the recoupling bandwidth which is limited to $\approx$ 7 kHz with a commercial 3.2 mm LTMAS probe (maximum MAS frequency $\approx$ 14 kHz at 100 K). Technical developments towards faster sample spinning with cryogenic helium gas[52,131] and/or smaller rotor diameter MAS-DNP probes[56] can offer a solution for this problem in the future.

For heteronuclear (^{13}C$-$^{15}N) distance measurements, 2D TEDOR spectra were recorded. While in general more time consuming due to the lower abundance of ^{15}N, they were acquired here in only 3 h 45 min per spectrum. These experiments are of great use for structure determination because they probe another nucleus and make another set of distances available. Due to slower polarization transfer (smaller gyromagnetic ratio of ^{15}N), however, the distances which can be probed are shorter than in ^{13}C$-$^{13}C experiments with comparable mixing times.

All approaches for distance measurements were demonstrated on nanotubes of cyclo-FF, probing distances between carbonyl and aromatic carbons (1D approach), among the aliphatic carbons (1D approach), among the aromatic carbons (2D approach), and between carbons and nitrogens (TEDOR). The polarization buildup curves obtained in all cases can be fully rationalized with numerical simulations based on the cyclo-FF crystal structure. The analysis reveals that each curve consists in the superposition of different distance contributions, reaching up to a remarkable length of ≈ 7 Å for ^{13}C$-$^{13}C distances. A theoretical description of these contributions as isolated spin pairs is shown to be sufficient, making the analysis straightforward and simple. Importantly, all buildup curves do contain contributions from several intermolecular distances, making them extremely valuable for supramolecular structure determination.

3.8 Materials and methods

DNP sample preparation of cyclo-FF

The cyclo-FF DNP sample was prepared by adapting the existing protocol:[40] Cyclo-FF powder (20 mg) was dissolved under gentle heating in hexafluoroisopropanol (750 µL). The solution was added dropwise and under continuous sonication to a solution of AMUPol (0.3 mg), trehalose dihydrate (0.5 mg) and D_8-glycerol (2 mg) in D_2O (2.5 ml) and D_4-methanol (0.5 mL), causing instant precipitation of cyclo-FF nanotubes. The mixture was transferred onto a petri dish and dried slowly under reduced pressure, while repeatedly stirring it with a spatula. After sufficient drying time (10$-$13 h), a wet paste was obtained and packed into a 3.2 mm thin-wall zirconia rotor. This process was repeated once more to fill up the rotor. It was observed that the slow drying process and the retaining of moisture at all times are beneficial for optimal MAS-DNP sensitivity.

DNP-enhanced solid-state NMR experiments

DNP experiments were performed on the MAS-DNP system described in section 2.4. All spectra were recorded with a recycle delay of 6.5 s. Proton and carbon $\pi/2$ pulses were applied at 100 kHz and 50 kHz RF-field strength, respectively. For CP from proton to carbon, the ^{13}C RF-field strength was fixed to ≈ 50 kHz and a linear ramp from 80 to 100 % around the $n = +1$ Hartmann-Hahn condition was applied on the proton channel. The CP contact time was 3 ms. Pre-saturation pulse trains were applied on both the proton and carbon channel prior to experiments. All spectra were recorded at a MAS frequency of 13.889 kHz except for the TEDOR experiments for which a MAS frequency of 12 kHz was used. The acquisition time for ^{13}C in the direct dimension was 25 ms.

Experimental details for the 1D approach

Spectra for the 1D approach were recorded with the pulse sequences shown in Figures 3.3a and 3.6a. Heteronuclear decoupling (CW,[16] SPINAL-64,[21] SW$_f$-TPPM[22]) was applied at 100 kHz RF-field strength. [S_3] homonuclear recoupling was applied with the S_3 pulses at an RF-field strength of 6.9 kHz. Selective carbon pulses were centered on the respective resonances, all other carbon pulses were centered between the carbon resonances which were recoupled. For each mixing time, 256 transients were accumulated, corresponding to ≈ 28 min per spectrum. The spectra were deconvoluted using the simplex algorithm in Topspin.

For the spectra probing polarization transfer from carbonyl to aromatic carbons (section 3.3), a ^{13}C 270° Gaussian pulse (truncated at 1 %) of 2.5 ms length and an excitation bandwidth of 700 Hz was applied to selectively flip up the carbonyl spins. Remaining transversal carbon magnetization was left to decay for 1 ms, assisted by a low-power purge pulse centered on the aromatic resonances and applied at an RF-field strength of ≈ 0.38 kHz. After the recoupling period, a z-filter of 100 µs was applied, followed by a selective E-BURP2[132] pulse with a duration of 1.65 ms and an excitation bandwidth of 3000 Hz. To measure the polarization buildups, 15 different mixing times were used, taking into account between 1 and 20 loops of S_3 between the bracketing pulses, with 1 loop of S_3 spanning 16 rotor cycles (1.152 ms in total). The total experimental time was ≈ 7 h for the whole set of 1D spectra. Spectra were processed without any apodization.

For spectra probing polarization transfer between the aliphatic carbons (section 3.4), a ^{13}C 270° Gaussian pulse (truncated at 1 %) of 15 ms length and an excitation bandwidth of 116.5 Hz was used. Remaining transversal carbon magnetization was left to decay for 2 ms, assisted by irradiation on the proton channel at an RF-field strength of ≈ 13.889 kHz. For the polarization buildup curves, 14 different mixing times were used, corresponding to $1-14$ loops of S_3. The total experimental time was ≈ 13 h for acquisition of the two sets of 1D spectra discussed in section 3.4.

The spectra were processed using 20 Hz exponential line broadening.

Experimental details for the 2D approach

2D ^{13}C$-$^{13}C DQ-SQ correlation spectra of the aromatic region were acquired with all carbon pulses centered close to the aromatic resonances (139 ppm). DQ excitation and reconversion of ^{13}C spins were achieved using the S_3 pulse sequence. 100 kHz RF-field strength was used for heteronuclear decoupling using SW$_f$-TPPM during indirect and direct detection periods, and CW decoupling during recoupling. A z-filter of 100 µs was inserted before acquisition. Ten experiments were recorded with different mixing times ranging from 2 to 20 loops of S_3 for both the DQ excitation and reconversion blocks. The acquisition time in the indirect dimension was 9.2 ms and States-TPPI[95] was used for quadrature detection. 32 transients were accumulated for each of the 64 complex t_1 points, leading to a total experimental time of $\approx$ 7.4 h. Spectra were processed without any apodization.

The spectrum in Figure 3.8a was taken with 80 scans per complex point (instead of 32), but was not taken into account for the polarization buildup curves.

For extracting the peak volumes, the Fourier-transformed DQ-SQ 2D spectra were sheared by 45° using NMR Pipe[133] prior to peak integration using a Monte-Carlo method.[126] The peak volumes were normalized as mentioned in section 3.5.2 and additionally scaled with respect to the CPMAS spectrum to take into account differential CP transfers.

Experimental details for the TEDOR spectra

2D ^{15}N$-$^{13}C correlation spectra were recorded with the TEDOR pulse sequence shown in Figure 3.10. $\pi/2$ and π-pulses on the carbon channel were applied at an RF-field strength 55 kHz. Pulses on the nitrogen channel were applied at 42 kHz RF-field strength. Each of the two REDOR periods consisted of $8n$ π-pulses on the nitrogen channel, equally distributed on both sides of one refocusing π-pulse on the carbon channel. n was incremented between 1 and 16 in steps of 1, and between 18 and 28 in steps of 2 in order to record spectra with different mixing times. SW$_f$-TPPM heteronuclear decoupling was applied during the REDOR and acquisition periods at an RF-field strength of $\approx$ 100 kHz. During the z-filters (τ_{zf}), irradiation on the proton channel was applied at an RF-field strength of $\approx$ 12 kHz for 2.083 ms (25 rotor periods, first z-filter) and 2 ms (second z-filter). Acquisition times in the direct and indirect dimension were 20 ms and 8.2 ms, respectively. Frequency discrimination in the indirect dimension was achieved using States-TPPI quadrature detection. 208 transients were accumulated for each of the 5 complex t_1 points, leading to an experimental time of $\approx 3\,\mathrm{h}\ 45\,\mathrm{min}$ for one 2D spectrum. 22 spectra were acquired which corresponds to a total experimental time of ≈ 3.5 days.

Normalization of polarization buildup curves for the 1D approach

For a better comparison to simulations, peak integrals of the spectra recorded with the 1D approach were normalized according to the initial polarization on CO, Cβ_1, or Cβ_2 spins. For this purpose, a reference experiment was performed replacing the entire recoupling block by a $\pi/2$ ^{13}C excitation pulse with subsequent detection. The resulting peak (CO, Cβ_1, or Cβ_2) was integrated and multiplied by 0.011 to take into account the probability of finding a particular ^{13}C spin in proximity to one of the excited spins. In addition to that, the integral of the CO peak was divided by 2 because the two carbonyls were excited together. These scaled values of the integrals were then used as normalization factor for all integrals of the respective buildup curves. This normalization procedure defines the initial magnetization available in each spin pair as 1, allowing to assess the absolute transferred polarization in these experiments for direct comparison to numerical simulations.

DFT-GIPAW calculations

Quantum chemical calculations on the cyclo-FF crystal structure were run using the planewave pseudopotential approach, with the GIPAW method[72] for computation of CSA tensors. The calculations were performed with the PWSCF module version 5.2.1, and GIPAW version 5.1. within the Quantum ESPRESSO package.[115] Norm-conserving pseudopotentials of the Troullier-Martins type[134] were used for all atoms, employing the PBE exchange-correlation functional.[135] They were downloaded from http://sites.google.com/site/dceresoli/pseudopotentials in September 2015 (X.pbe-tm-new-gipaw-dc.UPF, with X = H, C, N, O). The crystal structure of cyclo-FF was used as an initial input, and hydrogen positions were optimized prior to GIPAW calculations. A planewave cutoff energy of 96 Ry, and a $2 \times 2 \times 2$ Monkhorst-Pack k-point grid[136] were used. The results served as an input in SPINEVOLUTION simulations for buildup curves involving aromatic carbons.

Chapter 4

Towards *de novo* structure determination

4.1 General considerations

The previous chapter introduced different strategies for distance measurements and presented corresponding experimental data obtained on cyclo-FF. A thorough analysis of polarization buildup curves showed that they are in excellent agreement with the crystal structure of cyclo-FF. Based on these encouraging results, the present chapter will discuss the perspectives of using such buildup curves, recorded at NA, for *de novo* structure determination.

Ideally, one would want to extract internuclear distances directly from the polarization buildup curves and use them for structural modelling. The quality of the data presented in chapter 3, especially for the 1D approach, does demonstrate great potential towards this goal. However, in the present case of cyclo-FF, the applicability of this idea is strongly limited by the high number of distances which contribute to each polarization buildup curve. This situation arises because cyclo-FF is a rather small molecule in a densely packed structure,[98] meaning that many distances below 7 Å can be found for the same spin pair. Hence, a "*de novo*" fitting of polarization buildup curves becomes very ambiguous, especially when several contributing distances are of comparable length. While the direct extraction of single distances for cyclo-FF is therefore rather difficult, it can be expected to be considerably easier for larger molecules where fewer distances contribute to each buildup curve.

Since single distances can hardly be determined, it is more reasonable to use the ensemble of buildup curves for evaluating structural models. Based on a comparison between the experimental data and simulation of the expected buildup curves for the respective model, one can select among several candidate structures the structure which satisfies the experimental data best. The accuracy of the buildup curves acquired on cyclo-FF, their sensitivity to long distances, and their large number of distance contributions suggest that they will be very well suited to such a strategy. In addition to NMR data, this will also require the use of computational codes for creating the candidate structures. Moreover, powder XRD data should be a valuable addition which can potentially provide information on the unit cell and space group of the sample under investigation. The applicability of a similar approach has been shown by Brouwer *et al.* who used ^{29}Si$-$^{29}Si DQ buildup curves in combination with powder XRD data and computational algorithms for structure determination of zeolithes.[114]

The following sections will examine the sensitivity of the polarization buildup curves to the (supra)molecular structure of cyclo-FF and demonstrate the general feasibility of the approach described above. For this purpose, a step-wise approach to structure determination will be presented. First, the molecular structure of cyclo-FF will be determined by combining molecular mechanics, DFT, and NMR data (section 4.2). Second, it will be shown that supramolecular structure determination based on the polarization buildup curves is feasible when this molecular conformation is known (section 4.3).

4.2 Molecular structure of cyclo-FF

The determination of the molecular conformation within a supramolecular structure can be an important first step for structure determination. Because cyclo-FF has a fairly simple molecular structure, optimization of its conformation by computational methods is indeed relatively straightforward.

For this purpose, a conformational search of the entire potential energy surface of an isolated cyclo-FF molecule was carried out using the software TINKER.[137] Six local minima were obtained whose geometries were then optimized with the molecular DFT software ORCA.[138] After optimization, the three lowest energy structures (Figure 4.1a) were regarded as possible molecular conformations of cyclo-FF in the nanotubes studied here. Their energies all lie within 4 kcal/mol, which is in the range of the energy of non-covalent interactions like hydrogen bonding or π-stacking.

The three structures mainly differ in the positioning of the phenyl rings with respect to the central ring. In structure (**1**), they both point away from the central

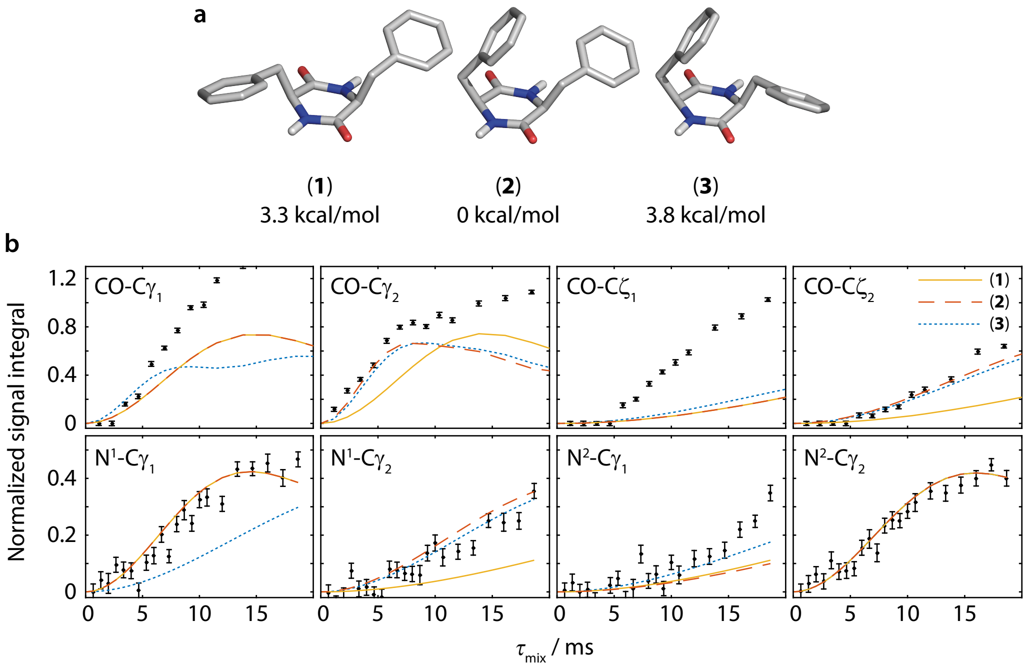

Figure 4.1: (a) Possible molecular conformations of cyclo-FF as determined by computational structure optimization. Their relative energies with respect to (**2**) are given below the structures. (b) Comparison of selected experimental polarization buildup curves (black points) to simulations for structures (**1**) (yellow solid lines), (**2**) (dashed red lines), and (**3**) (blue dotted lines). The experimental points are identical to those shown for the 1D approach between carbonyl and aromatic carbons in Figure 3.3 (top row), and to those obtained from the TEDOR spectra in Figure 3.12 (bottom row). Only intramolecular spin pairs are included in the simulation, meaning that two distances contribute to each CO buildup curve and one distance contributes to each nitrogen buildup curve. No scaling was applied to the simulated curves.

ring, whereas one of them is bent over it in the other two structures. In structure (**2**), the phenyl ring which points away is oriented towards the NH group of the central ring, whereas it is oriented towards the carbonyl group in structure (**3**). Overall, there are two asymmetric (**2** and **3**) and one nearly C_2-symmetric structure (**1**). Structure (**2**) has the lowest energy in vacuum.

The different experimental chemical shifts for the two phenylalanines in cyclo-FF suggest that an asymmetric structure is present in the nanotubes, such as found in structures (**2**) and (**3**). The most likely structure can be selected based on the experimental polarization buildup curves presented in chapter 3. Since the main difference between the three structures lies in the orientation of the phenyl rings with respect to the central ring, buildup curves were chosen which probe distances between these rings (Figure 4.1b). More precisely, they represent polarization transfer between nitrogens or carbonyls (central ring) and the aromatic carbons Cγ or Cζ (phenyl rings).

Table 4.1 summarizes the distances which occur in structures (**1**)−(**3**) for the respective spin pairs probed by the buildup curves. Based on these distances, the expected polarization buildup curves for the spin pairs containing CO were simulated in SPINEVOLUTION,[112] using CSA values from literature[99] and random CSA tensor orientations. The buildup curves for the TEDOR experiments were calculated using Bessel functions[127,130] and multiplied by the biexponential decay function as used in section 3.6.3. Figure 4.1b compares the experimental points of the aforementioned buildup curves with the simulations for the three different structures.

A visual examination of the Figure already allows determining the most likely structure. Structure (**1**) is not very well supported, as it can be seen from the deviation between experimental points (black points) and simulation (yellow solid lines) in the plots for CO−Cγ_2, CO−Cζ_2, and N^1−Cγ_2. The buildup for the N^1−Cγ_1 spin pair also allows distinguishing between structures (**2**) and (**3**). It probes the orientation of the phenyl ring which points away from the central ring, which is the main difference between the two structures. In structure (**2**), the phenyl ring is oriented over the NH group, leading to a short distance between N^1 and Cγ_1 (3.0 Å). This distance is considerably longer in structure (**3**) (3.8 Å) where the phenyl ring is oriented over the carbonyl group. The rather fast rise of the experimental curve therefore matches the simulation for structure (**2**) (red dashed line) much better than the simulation for structure (**3**) (blue dotted line). These observations suggest that structure (**2**) describes the conformation of the cyclo-FF molecule best.

To further support this analysis, the goodness-of-fit coefficient χ^2 (see Table 4.1) was determined to evaluate the difference between experimental points and simulation for each structure. It was calculated as the residual sum of squares

$$\chi^2 = \sum_i (I^i_{\text{exp}} - I^i_{\text{sim}})^2, \tag{4.1}$$

where i includes all points of the buildup curves shown in Figure 4.1b with the following two exceptions. For the CO−Cγ_1 and CO−Cγ_2 buildups, only the first five points were considered because the influence of additional (intermolecular) distances becomes too prominent at longer mixing times. The buildup curve for CO−Cζ_1 is clearly not dominated by intramolecular distances and was therefore not taken into account for this analysis. For comparison, the simulated curves were also fitted to the experimental points by an amplitude factor A as described in chapter 3. In order to avoid unrealistic scaling, A was constrained to be in between 0.5 and 1.5. The

Table 4.1: Distances (in Å) in structures (**1**)−(**3**) in Figure 4.1a which can contribute to the buildup curves in Figure 4.1b.

	Structure (**1**)	Structure (**2**)	Structure (**3**)
CO−Cγ_1	3.9 / 4.1	3.9 / 4.1	3.2 / 4.8
CO−Cγ_2	3.9 / 4.0	3.0 / 3.6	3.1 / 3.7
CO−Cζ_1	6.1 / 6.5	6.1 / 6.5	5.3 / 7.5
CO−Cζ_2	6.1 / 6.5	5.0 / 5.1	5.1 / 5.2
N^1−Cγ_1	3.0	3.0	3.8
N^1−Cγ_2	4.7	3.6	3.7
N^2−Cγ_1	4.7	4.8	4.3
N^2−Cγ_2	3.1	3.1	3.1
$\chi^{2\,a}$	2.13	0.54	0.80
$\chi_A^{2\,a}$	1.16	0.26	0.32

a. Goodness-of-fit coefficients between experimental points and simulation in Figure 4.1b, determined without (χ^2) and with (χ_A^2) an amplitude factor A (constrained between 0.5 and 1.5) that scales simulation to experiment.

goodness-of-fit coefficient χ_A^2 (see Table 4.1) was determined for this procedure, too:

$$\chi_A^2 = \sum_i (I_{\mathrm{exp}}^i - A \cdot I_{\mathrm{sim}}^i)^2, \tag{4.2}$$

where the scaling factor A has been optimized for each buildup curve separately. Table 4.1 shows that both methods (χ^2 and χ_A^2) return the same order of structures, where structure (**2**) has the lowest, and structure (**1**) the highest χ^2 values.

In summary, the experimental buildup curves and the calculated energy are consistent with a conformation very similar to structure (**2**) being present in the cyclo-FF self-assembled nanotubes. This is confirmed by comparison to the crystal structure of cyclo-FF.[98] An RMSD of 1.12 Å is obtained when comparing atomic positions (not including hydrogen atoms) in structure (**2**) to those in the molecule as present in the crystal structure. Hence, the described method of combining molecular mechanics and DFT leads to the globally correct structure of cyclo-FF which can be identified based on the NMR data.

It should be kept in mind that such a procedure may not always be successful in determining the molecular conformation independently from its assembly. The main reason for this is that the computational structural search and optimization are performed on an isolated molecule. Therefore, intermolecular interactions like hydrogen bonding and π-stacking are not taken into account which can however stabilize conformations that may not be the most energetically favoured on their own. In the present example of cyclo-FF though, its geometry seems to be determined mainly on the molecular level and not so much by intermolecular interactions. A conformational search as shown here then provides an extremely valuable entry point for further structure calculations.

A general complicating factor for identifying the molecular structure is the need of being able to distinguish between intra- and intermolecular distances in the polarization buildup curves. The results shown here suggest that relatively short distances in the candidate structures should mainly be looked at, in particular distances between atoms that are linked by three or four chemical bonds, like in the N$-$Cγ and CO$-$Cγ buildup curves. Such distances provide useful information on the local geometry, and only minor intermolecular distance contributions to their buildup curves should normally occur during the initial recoupling period. In certain cases, it may be advisable to only consider the first few points of the buildup curves (as it was done for the CO$-$Cγ buildup curves here) to not be misled by contributions from intermolecular distances.

4.3 Supramolecular structure of cyclo-FF

4.3.1 The idea

The previous section has shown that polarization buildup curves recorded at NA allow determining the molecular conformation of cyclo-FF (section 4.2). However, they do not only probe the structure of one molecule, but are also clearly sensitive to intermolecular contacts (up to distances of ≈ 7 Å) as demonstrated in chapter 3. The aim of this section is therefore to show that this sensitivity to intermolecular distances is indeed good enough to enable supramolecular structure determination. For this purpose, we designed a computational code, implemented in Fortran by Jean-Marie Mouesca, which creates a multitude of potential structures and determines the crystal structure which is in best agreement with the experimental data.

The present implementation of this code assumes that the molecular structure of cyclo-FF and its unit cell parameters are known. As demonstrated in the previous section, this is a realistic assumption regarding the molecular conformation. The unit cell parameters are often also accessible through powder XRD data. Since the main objective of this section is to demonstrate the usefulness of NMR buildup curves for structure determination, literature values for both the molecular structure[98] and the unit cell parameters (orthorhmobic lattice with $a = 6.185\,\text{Å}$, $b = 10.383\,\text{Å}$, $c = 23.851\,\text{Å}$[111]) will be used in the following.

These parameters allow determining the number of formula units (Z) in the unit cell, using the empirical equation[139]

$$Z \approx \frac{V}{18 \cdot n_{\text{non-H}}}, \tag{4.3}$$

with V being the volume of the unit cell in Å^3 and $n_{\text{non-H}}$ the number of non-hydrogen atoms in the molecule. This calculation gives $Z \approx 3.87$, meaning that there are four formula units in the unit cell of cyclo-FF. The occurrence of more than one independent molecule in the asymmetric unit can be excluded with relative certainty from the CPMAS spectra (Figure 3.2c,d). Based on this analysis, potential space groups for cyclo-FF can be narrowed down to fourteen which have an orthorhombic lattice and $Z = 4$: Space groups 16 to 19 and 25 to 34.

The Fortran code has been designed with the aim of finding the most likely arrangement of cyclo-FF molecules for each of these fourteen space groups by systematic sampling of the space in the unit cell and comparison to the NMR polarization buildup curves. While the space group of a sample can often be extracted directly from powder XRD data, the code was still run here for all possible space groups. This provides the opportunity to evaluate more candidate structures and to obtain a better idea of how sensitive the NMR polarization buildup curves really are to the supramolecular structure.

For the results presented in the following, only buildup curves from the 1D approach were used since this data has the highest quality. This corresponds to a total of nine buildup curves, comprising all six curves for polarization transfer from carbonyl to aromatic carbons (section 3.3) and three curves for polarization transfer between the aliphatic carbons (section 3.4). The $\text{C}\beta_1{-}\text{C}\alpha_1$ and $\text{C}\beta_2{-}\text{C}\alpha_2$ curves were not included due to the complicating contribution of a one-bond distance (see section 3.4). Since a central element of the code is the comparison of expected polarization buildup for a trial structure to the experimental buildup, a library of simulated buildups has been created with SPINEVOLUTION for $^{13}\text{C}{-}^{13}\text{C}$ spin pairs at distances between 3.0 and 9.0 Å in steps of 0.1 Å, using CSA values from literature[99] and random CSA orientations. From this library, the expected polarization buildup curves can be computed rapidly, and no (more time-consuming) simulations with SPINEVOLUTION are required during execution of the code.

4.3.2 Principle of the computational code

The general principle of the Fortran code is sketched in Figure 4.2 and will be explained in the following. At first, a three-dimensional search grid is created in one eighth of the unit cell. For the results presented in the following, the grid was composed of $9 \times 9 \times 9$ points around a central point with fractional coordinates $(0.25, 0.25, 0.25)$. Points were spaced by regular steps of 0.05 in each dimension, ranging from 0.05 to 0.45. Sampling only this fraction of a unit cell with $Z = 4$ is sufficient for probing all possible supramolecular arrangements because all other positions of cyclo-FF molecules will be occupied by applying the respective symmetry operations.

An iterative search procedure is performed for each grid point. The molecule is first centred on the grid point, and then translated to different points on a "microgrid" (here $5 \times 5 \times 5$ points spaced by 0.01) around the main grid point. For each position on this microgrid, all possible orientations are probed by rotating the molecule around its geometric center. Each molecular orientation obtained this way is then evaluated by creating the surrounding molecules based on the space group symmetry, determining all relevant distances to these molecules, and calculating the expected polarization buildup curves based on the library created with SPINEVOLUTION (see previous section). For this calculation, either a fixed cutoff distance of 7 Å is used or the cutoff distance is optimized for each buildup curve separately (see below). The expected buildup curves are then compared to the experimental curves and the goodness-of-fit coefficient χ^2 is calculated as given in equation 4.1, taking all points of the buildup curves into account. This iterative procedure is guided by the goal of minimizing χ^2. Therefore, the orientational search is intensified around the orientation which results in the lowest χ^2 values, by gradually refining the spacing of "microgrid" points and the rotation angles. Once a minimum χ^2 is determined for one grid point, the search is repeated for the next point, eventually producing a list of minimum χ^2 values, determined for each point on the search grid.

During the search procedure, two additional test criteria (red in Figure 4.2) are applied before the simulated buildup curves are calculated. The criteria are defined to ensure sufficient interatomic distances between molecules, avoiding the evaluation of structures in which neighbouring molecules would collide. The smallest allowed interatomic distance between molecules has been defined as 2.7 Å, including all atoms but hydrogen. The first test (“Collision test 1” in Figure 4.2) is performed after the molecule has been translated to a new point on the “microgrid”. It ensures that at least one orientation can be found for this point in which neighbouring molecules do not collide. This is achieved by determining the distances between the geometric centres of adjacent molecules. It has been determined in an independent test that if this distance is shorter than 5.2 Å, no molecular orientation can be found in which all interatomic distances between molecules are at least 2.7 Å. In such a case, no rotations are performed and the next point on the “microgrid” is probed.

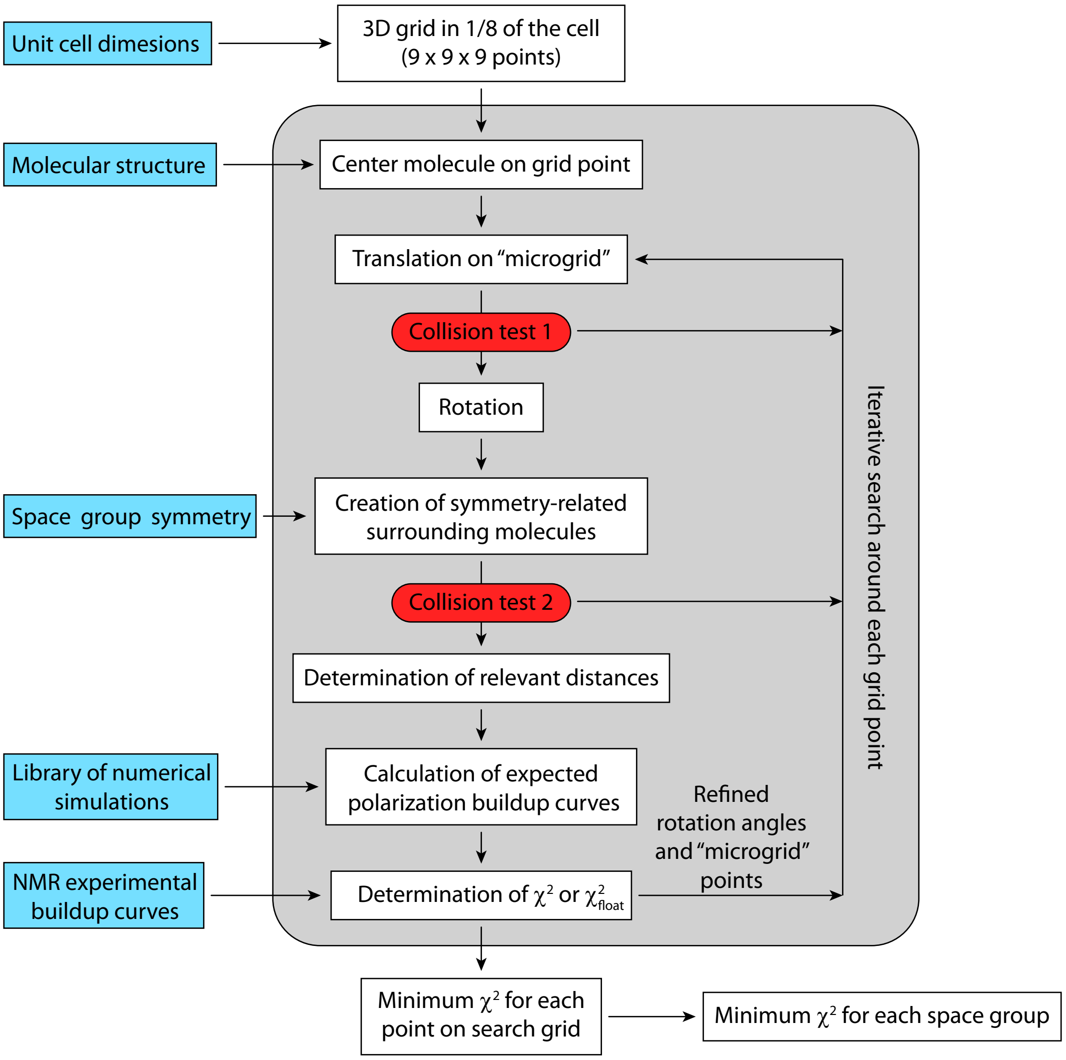

Figure 4.2: Schematic representation of the Fortran code used to determine the supramolecular structure of cyclo-FF. Input of external information is highlighted by blue rectangles and actions by the code are shown in white rectangles. Two “collision tests” are highlighted in red, designed to exclude structures in which neighbouring molecules would collide. The grey box highlights the iterative search procedure which is performed around each point of a three-dimensional grid created in one eighth of the unit cell.

If the first test is passed, the second test criterion ("Collision test 2" in Figure 4.2) is evaluated after a molecule has been rotated into a new orientation and its neighbouring molecules have been created. It is then tested whether all interatomic distances between two neighbouring molecules are at least 2.7 Å(not including hydrogen atoms). If this criterion is not met, the respective orientation is discarded and the next rotation step is performed. A χ^2 value is only determined if both tests are passed, meaning that some grid points or even whole space groups may not result in any possible solution. These two tests do not only exclude thermodynamically unstable structures, but also reduce the calculation time by for example not performing the time-consuming rotations if the first test is not passed.

Two options were tested for calculating the expected polarization buildup curves. They differed in the definition of the A value by which the simulation is scaled to the experimental data, and of the cutoff distance which is the longest distance taken into account for calculating the curves. For the first option, the cutoff distance was fixed to 7.0 Å (as in sections 3.3 and 3.4) and the A value was set to 1.0 for all buildup curves. For the second option, A was set to 1.0 as well, but the cutoff distance was adjusted individually for each buildup curve (between 3.0 and 9.0 Å) to achieve the best fit. This second option is based on the analysis carried out in section 3.3.4 where it was shown that an individual fitting of buildup curves is a reasonable approach due to effects of (partial) dipolar truncation at longer distances. The cutoff distance was optimized here instead of A which should roughly be equivalent to optimizing the A value (see Figure 3.4). However, this procedure may yield multiple structures with very similar χ^2 values because differing cutoff distances can compensate for slightly shorter or longer distances in the structures created. Two different χ^2 values were therefore determined for each space group (in separate runs of the code), one for the first option with a fixed cutoff distance, χ^2_{fixed}, and one for the second option with an individually determined ("floating") cutoff distance, χ^2_{floating}.

4.3.3 Results

As mentioned in section 4.3.1, the code was run using the unit cell dimensions and molecular structure of cyclo-FF as given in literature.[98,111] Experimental polarization buildup curves for $\mathrm{CO{-}C_{aromatic}}$, $\mathrm{C}\alpha_1{-}\mathrm{C}\beta_2$, $\mathrm{C}\alpha_2{-}\mathrm{C}\beta_1$, and $\mathrm{C}\beta_1$-$\mathrm{C}\beta_2$ were compared to the expected buildup curves, calculated for a proposed structure using a library of buildup curves created with SPINEVOLUTION. Fourteen potential space groups were probed (16−19 and 25−34), determining minimum χ^2_{fixed} and χ^2_{floating}

Table 4.2: Results from the Fortran code (χ^2_fixed and χ^2_floating) and DFT-GIPAW calculations (relative energy and ^{13}C chemical shift RMSD) for each space group. Among the 14 space groups evaluated, only those for which solutions were found are shown.

	Space group							
	18	19	28	29	31	32	33	34
χ^2_fixed	0.59	0.57	1.89	1.49	12.14	0.73	0.69	0.77
χ^2_floating	0.26	0.26	0.67	0.27	0.34	0.29	0.27	0.27
$E_\text{rel,DFT}$ / kcal/mol	0.0	9.2	47.8	173.2	206.3	199.9	14.6	210.2[a]
$\delta_\text{iso}(^{13}\text{C})$ RMSD / ppm	1.57	2.06	3.29	4.40	4.57	4.30	1.91	4.10

a. Value after 200 cycles of geometry optimization (not converged).

values (see section 4.3.2) for each space group.

For several space groups (16, 17, 25, 26, 27, 30), no possible structures could be found, meaning that no molecular orientation satisfied the two test criteria described in section 4.3.2. The results obtained for the other space groups are summarized in Table 4.2. As expected, the χ^2 values obtained with a fixed cutoff distance (χ^2_fixed) are higher and exhibit a stronger variation in between the different space groups than those obtained with individually optimized cutoff distances (χ^2_floating). Overall, space groups 18 and 19 have the lowest χ^2 values for both approaches, with the values for space group 19 being marginally smaller.

While the Fortran code does identify the structure for each space group which satisfies the NMR data best, it does not consider the energy of the proposed structures. Therefore, the geometries of the final structures, obtained by minimizing χ^2_floating, were optimized by plane-wave DFT with the Quantum ESPRESSO software package.[115] All atomic positions were optimized while the cell dimensions were held fixed. The final energies (Table 4.2) show that the structure with space group 18 has by far the lowest energy, notably also compared to the structure of space group 19 which has the lowest χ^2 values. For an additional evaluation of the final structures, the ^{13}C chemical shift were computed for the DFT-optimized structures, using the GIPAW approach[72] in its implementation in Quantum ESPRESSO. The RMSD between these calculated and the experimental ^{13}C chemical shifts (Table 4.2) has again its lowest value for the structure of space group 18.

χ^2 values, calculated energy and calculated ^{13}C chemical shifts indicate that the structure with space group 18 corresponds to the supramolecular structure of cyclo-FF. Figure 4.3 shows this structure as determined by the Fortran code (a, purple) and after geometry optimization with DFT (b, blue), and compares both to the crystal structure of cyclo-FF (orange). Respective RMSDs of 0.560 Å (a) and 0.189 Å (b) are obtained when comparing atomic position (not including hydrogen atoms) in the computed structures to those in the crystal structure, taking into account all four molecules in the unit cell. Overall, the final structure (b) is in excellent agreement with the crystal structure of cyclo-FF.

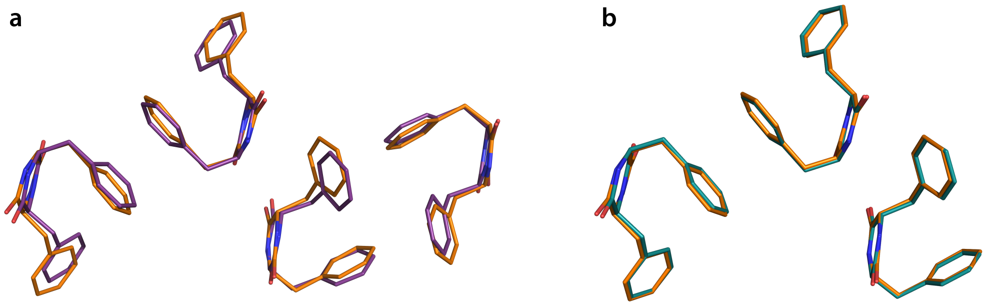

Figure 4.3: Overlay of the crystal structure of cyclo-FF[98] (orange) and the structures which were obtained with the Fortran code for space group 18 before (a, purple) and after (b, blue) geometry optimization with plane-wave DFT. The four formula units of cyclo-FF which are found in each unit cell are shown.

The calculation of χ^2 with a fixed A value and cutoff distance leads to similar results as optimizing these parameters individually. Interestingly though, the use of χ^2_{fixed} makes the "correct" result stand out more clearly, and also roughly reflects the trend observed for the calculated energies and ^{13}C chemical shift RMSDs. A similar observation was made for the determination of the molecular structure (section 4.2). This suggests that fixed A and cutoff values lead to very reasonable results and that they may be even preferable for identifying the more likely structures.

Overall, this section has demonstrated that the buildup curves presented in the previous chapter are not only sensitive to intermolecular distances, but are also a powerful resource for supramolecular structure determination. Among a very large number of candidate structures evaluated, a structure could be selected which is in very good agreement with the crystal structure. In addition to this great accuracy, evaluating candidate structures by comparing experimental and expected polarization buildup curves is extremely fast. This constitutes an important advantage over the "traditional" NMR crystallography approach which uses time-consuming GIPAW-based chemical shift calculations for this step.[75,76]

4.4 Conclusions

This chapter has shown that the polarization buildup curves presented and analyzed in chapter 3 can be used to determine both the molecular and the supramolecular structure of cyclo-FF. For this purpose, structural models were created and evaluated by comparison of experimental data to simulated polarization buildup curves based on these models.

Following this approach, a conformation which exhibits the same features as cyclo-FF in the crystal structure could be chosen from several models created by molecular mechanics and molecular DFT. This can provide a very good entry point for structural studies and enable supramolecular structure determination as presented in the second part of this chapter.

For this purpose, a Fortran code has been presented. It uses the molecular structure (here from the crystal structure) and the unit cell dimensions to sample all possible molecular orientations within the unit cell, employing a given space group symmetry. Again based on comparing simulated and experimental buildup curves and a final DFT geometry optimization step, a structure was obtained which is in excellent agreement with the crystal structure of cyclo-FF.

The wealth of information contained in the ensemble of polarization buildup curves therefore proves very powerful in directing a structural search. Treating all buildup curves together with one “global” χ^2 value is the preferable strategy in case of cyclo-FF and other small molecules. An individual treatment and fitting of buildup curves would be very ambiguous due to the large number of distance contributions, and in addition due to their dependence on CSA tensor orientations when carbons with large CSA are involved (see section 3.3.2). While these orientations had to be computed with DFT to obtain the best fit in section 3.3, a use of random CSA orientations for the structure searches presented in this chapter (using a global χ^2) was indeed sufficient to obtain a very good result.

Two more reasons make this approach to structure determination very efficient. Firstly, expected buildup curves can be calculated from a previously generated library of simulated buildup curves for each distance, making this step very fast and allowing the evaluation of hundreds of models within a reasonable time. This is a clear advantage over the common NMR crystallography approach which uses chemical shift calculations with DFT-GIPAW that can last several days for just one structure.[75,76]

Secondly, experimental data obtained with the 1D approach (sections 3.3 and

3.4) is not only very accurate, but can also be scaled very precisely with respect to the polarization transfer efficiency. Only this well-defined amplitude of the experimental signal makes it possible to use fixed A and cutoff values or to constrain them over a narrow range. This essentially removes one fit variable when comparing experiment and simulation, avoiding "false fits" in which a large amplitude factor compensates for a simulated curve which does not match experiment. Indeed, the example in section 4.3 only used buildup curves obtained with the 1D approach (nine in total), providing an impressive demonstration of their utility for structure determination.

Of course, the integration of the remaining buildup curves presented in chapter 3 into the structure determination protocol will be desirable for the future. The major challenge here can be expected to be the scaling of 2D data, as it is less uniform than that of the 1D data. In this respect, it will be interesting to see how much improvement to the structure determination procedure this data can provide.

4.5 Perspectives

The evaluation of structural models by comparison to polarization buildup curves recorded at NA has been shown to be reliable and fast, and opens up a new avenue to crystal structure determination. Therefore, future research should focus on the computational aspects of this approach, identifying efficient ways of creating model structures and integrating the experimental data.

The Fortran code presented in section 4.3 is one possible approach. It executes a systematic grid search of the unit cell and has been shown to be a powerful method when molecular structure and unit cell dimensions can be obtained beforehand. It determines a very good structure even without including energetic considerations, but does require DFT calculations as a final step to select the best structure among different space groups.

As an alternative, force field based energy calculations can be integrated directly into the structure search, and may easily exclude high-energy structures like those of space groups 29, 31, and 32 in section 4.3. Numerous programs exist for such energy calculations which may be modified according to the current problem. In this context, the molecular and supramolecular structure could also be optimized in one protocol instead of determining them consecutively as shown in this chapter.

One computational option are algorithms developed for crystal structure prediction (CSP, see also section 1.3.2).[73,74] They probe the whole lattice energy landscape and will eventually create the correct structure (provided enough trials are made), which could be identified reliably with the NMR buildup curves. However, the computational cost can become prohibitive when large and flexible structures are analyzed. The successful combination of CSP, ^{1}H-NMR and (time-consuming) DFT chemical shift calculations for crystal structure determination has indeed been demonstrated.[75,76]

Another option can be the use of the existing framework of a program like XPLOR-NIH, which is a popular software for biomolecular structure determination.[140,141] The software package comprises a variety of structure optimization procedures for the minimization of a target function that includes both experimental NMR restraints and information on the geometry of the molecule in question. By integrating experimental NMR buildup curves into the target function, the power of this well-established code could be combined with the high information content of the buildup curves. A similar approach has been demonstrated a while ago by integrating proton spin diffusion curves into the XPLOR-NIH program for crystal structure determination.[142,143]

The ideal approach for molecular modeling will always depend on the structure under investigation. The properties of the respective structure, especially its size and rigidity, and the amount of available experimental data will require a smart choice of the structure determination procedure in order to avoid exceedingly long computational times.

Any such procedure should benefit from including more experimental data, both in terms of speed and reliability. If available, powder XRD data will be a very useful extension, providing unit cell parameters and possibly the space group. This would greatly reduce the search space and hence speed up calculations.

Moreover, depending on the characteristics of the sample under investigation, it may be possible to obtain additional constraints which accelerate the evaluation of candidate structures. Similar to the “collision tests” in the Fortran code, structures which do not satisfy these constraints could be discarded immediately. Such constraints could be distance information obtained from NMR data, for example by extracting distances from simpler polarization buildup curves, or from the presence or absence of certain cross-peaks in 2D spectra. However, such criteria should be applied with care in order to not exclude plausible structures.

While one strength of the present approach is that it does not require time-consuming DFT calculations for each step, a final DFT step should still be part of the structure determination protocol. As also done in section 4.3, it serves both for geometry optimization and as a means of structure validation by comparing the calculated chemical shifts to experimental ones.

Overall, this chapter illustrates great perspectives for NMR crystallography at NA. The use of polarization buildup curves recorded at NA for evaluating structural models constitutes a very powerful approach to *de novo* structure determination. Future challenges lie in the development of efficient structure determination protocols with these buildup curves and in the validation of this approach on systems other than cyclo-FF.

4.6 Materials and methods

Optimization of the molecular structure

The molecular mechanics software TINKER[137] (version 7.1) was used for conformational search of the potential energy surface of one cyclo-FF molecule, employing the AMBER99 force field.[144] Six local minima were found. Their geometries were refined using DFT-based geometry optimization as implemented in the ORCA software package (version 3.0.2).[138] The optimizations were done in two steps, first using the TZVP basis set[145] and the BP86 functional,[146,147] and subsequently with the def2-TZVP basis set[148] and the B3LYP hybrid functional,[149–151] including atom-pairwise dispersion correction with Becke-Johnson damping (DFT-D3).[152,153] The three lowest energy structures are presented in Figure 4.1a.

DFT-GIPAW calculations

DFT-GIPAW calculations on the final structures obtained with the Fortran code for each space group were performed with the same parameters as given in section 3.8. All atom positions were allowed to vary during structure optimization, while the unit cell dimensions were held fixed. Chemical shielding tensors were then calculated using the GIPAW approach. For the calculation of the ^{13}C chemical shift RMSD, $\sigma_{\mathrm{iso,ref}}$ was first determined by fitting a straight line with slope -1 to a plot of calculated isotropic chemical shieldings ($\sigma_{\mathrm{iso,calc}}$) versus experimental isotropic chemical shifts ($\delta_{\mathrm{iso,expt}}$). The RMSD between the referenced calculated chemical shifts ($\delta_{\mathrm{iso,calc}} = \sigma_{\mathrm{iso,ref}} - \sigma_{\mathrm{iso,calc}}$) and the experimental chemical shifts ($\delta_{\mathrm{iso,expt}}$) was then determined. The RMSD values and the relative energies of the final structures are summarized in Table 4.2.

Chapter 5

Improvements for supercycled recoupling sequences

5.1 Introduction

5.1.1 Symmetry-based pulse sequences

Dipolar recoupling sequences are necessary for recording correlation spectra and measuring distances.[70,71] The design of such sequences is a challenging task because they should not only efficiently reintroduce the dipolar interaction at experimentally feasible conditions, but should also be robust with respect to interfering interactions, such as CSA, heteronuclear couplings (^{1}H$-$^{13}C), resonance offsets, and pulse imperfections.

Symmetry-based principles introduced by Levitt and co-workers offer a simple way to design pulse sequences which selectively recouple some spin interactions while suppressing others.[104] The spin interactions are classified by quantum numbers l, m, λ, and μ, which describe the rotational properties of the considered interaction with respect to rotations of the sample (spatial part) and of the nuclear spins (spin part). These rotational properties can be described as irreducible spherical tensors of rank l with components of index $m = -l, -l+1, ..., +l$ for the spatial part, and of rank λ with components of index $\mu = -\lambda, -\lambda+1, ..., +\lambda$ for the spin part. For example, the homonuclear dipole-dipole interaction has space rank $l = 2$ and spin rank $\lambda = 2$.

Two different classes of symmetry-based sequences have been introduced: CN_n^ν and RN_n^ν sequences, where N, n, and ν are called the symmetry numbers of the respective sequence. Simple schemes for constructing a sequence with a given set of symmetry numbers have been defined.[104] The power of symmetry-based pulse sequence design is that simple selection rules can be used for determining whether a spin interaction is symmetry-allowed or symmetry-forbidden under a particular RF pulse sequence. For the two classes of sequences, the following selection rules for the first-order average Hamiltonian $\overline{\mathcal{H}}^{(1)}_{lm\lambda\nu}$ of an interaction with quantum numbers $\{l, m, \lambda, \mu\}$ apply:[154,155]

$$\text{For } CN_n^\nu \text{ sequences:} \qquad \overline{\mathcal{H}}^{(1)}_{lm\lambda\nu} = 0 \text{ if } mn - \lambda\nu \neq NZ \tag{5.1}$$

$$\text{For } RN_n^\nu \text{ sequences:} \qquad \overline{\mathcal{H}}^{(1)}_{lm\lambda\nu} = 0 \text{ if } mn - \lambda\nu \neq \frac{N}{2} Z_\lambda, \tag{5.2}$$

where Z is an integer including zero (equation 5.1), and Z_λ is an integer with the same parity as the spin rank λ (equation 5.2).

5.1.2 γ-encoding and supercycling

A popular concept for the design of dipolar recoupling sequences is so-called γ-encoding.[156] In γ-encoded pulse sequences, each spatial component with quantum numbers $\{l, m\}$ corresponds to only one spin component with quantum numbers $\{\lambda, \mu\}$. As a consequence, only the phase but not the amplitude of the recoupled Hamiltonian depends on the Euler angle γ_{MR} which relates the molecular frame to the rotor frame.[156] Consequently, the recoupling efficiency in powders has a reduced dependence on crystallite orientations.

For DQ recoupling, this results in a high maximum DQ filtering (DQF) efficiency of $\approx 73\,\%$, compared to $\approx 52\,\%$ in non-γ-encoded sequences.[156] Therefore, many DQ recoupling sequences were designed to be γ-encoded, starting from DQ-HORROR,[156] to sequences such as C7,[157] POST-C7,[158] SPC-5,[159] $\mathrm{R}14_2^6$,[155] and CMRR.[160] However, experimental imperfections and interfering interactions like CSA often lead to dramatically reduced efficiencies in practice, and the high theoretical values can usually not be achieved. This becomes a particularly critical problem over long recoupling times, and impairs the detection of long-distance correlations.[100]

Compensation for such deleterious influences can be achieved by supercycling, where the same sequence is repeated with cyclic RF phase shifts and/or permutations.[91,161] Even though this often leads to a loss of the γ-encoding property and associated reduced theoretical maximum efficiency, the increased robustness of supercycled sequences means that they frequently outperform γ-encoded sequences experimentally.[161]

5.1.3 The SR26 sequence

One important example of a supercycled recoupling sequence is the SR26 sequence.[78,91] It is based on the $\mathrm{R26}_4^{11}$ pulse scheme[104,155] and uses the basic element $[90_0 270_{180}]$, with RF pulses and their phases (subscripts) denoted in degrees.[78] Four cycles are executed overall, namely the basic cycle S_0, a π-shifted cycle in which all RF phases are shifted by 180° (S_π), a phase-inverted cycle in which the signs of all RF phases are inverted ($S'_0 \equiv \mathrm{R26}_4^{-11}$), and a π-shifted phase-inverted cycle which combines both operations (S'_π). The full SR26 sequence has the form $S_0 S'_0 S'_\pi S_\pi$ and can be written explicitly as:[78]

$$\begin{aligned}&[90_{76.15}270_{256.15}90_{283.85}270_{103.85}]^{13} \times [90_{283.85}270_{103.85}90_{76.15}270_{256.15}]^{13} \times \\ &[90_{103.85}270_{283.85}90_{256.15}270_{76.15}]^{13} \times [90_{256.15}270_{76.15}90_{103.85}270_{283.85}]^{13}\,,\end{aligned} \tag{5.3}$$

where each block is repeated 13 times, as indicated by the superscript. The full SR26 cycle spans 16 rotor periods (τ_r) and requires RF irradiation at an RF field strength that corresponds to 6.5 times the MAS frequency. The construction principle of SR26 is summarized in Figure 5.1.

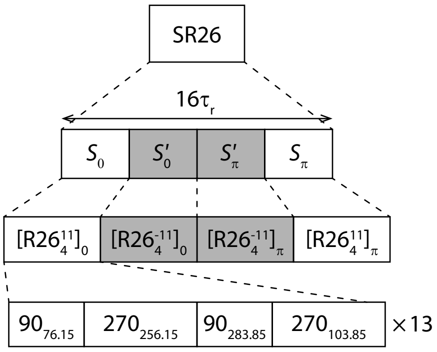

Figure 5.1: Construction scheme of the SR26 pulse sequence.[78] The sequence consists of four S elements based on the $\mathrm{R26}_4^{11}$ sequence. Overall RF phase shifts are indicated by subscripts, phase inversion by S' and gray boxes. The construction of one R-element is given in the bottom boxes, with flip angles and phases (subscripts) in degrees.

First-order selection rule analysis (equation 5.2) shows that the $\mathrm{R26}_4^{11}$ sequence (S_0 and S_π) only allows dipole-dipole coupling terms with the quantum numbers $\{l, m, \lambda, \mu\} = \{2, \pm 1, 2, \mp 2\}$. The related $\mathrm{R26}_4^{-11}$ sequence (S'_0 and S'_π) allows dipole-dipole terms with $\{l, m, \lambda, \mu\} = \{2, \pm 1, 2, \pm 2\}$. Each separate cycle hence creates a pure DQ average Hamiltonian to first order (ignoring the homonuclear J-coupling) and is γ-encoded. However, the full SR26 sequence is not γ-encoded because different terms are recoupled during the different cycles (see also section 5.3.2).

The SR26 sequence allows robust and broad-band dipolar recoupling. It has enabled for example the acquisition of ^{29}Si$-^{29}$Si DQ build-up curves of zeolite and silicate samples at NA, which were sensitive to silicon$-$silicon distances of up to 8 Å[113] and played an important role in structure elucidation of these systems.[114,162,163]

This chapter will revisit the supercycles of $R26_4^{11}$, addressing two aspects which are often regarded as disadvantages of non-γ-encoded encoded pulse sequences and supercycling.[161] First, 2D DQ-SQ correlation spectra can only be recorded with rotor-synchronized t_1 evolution, restricting the spectral width in the indirect dimension. Second, the maximum theoretical recoupling efficiency is limited to $\approx 52\,\%$. In the following, it will be shown how SR26 2D DQ-SQ correlation spectra can be recorded with large DQ spectral widths when appropriate phase shifts are applied (section 5.2), and how its DQF efficiency can be increased over 52 % when certain sequence block permutations are applied (section 5.3).

5.2 2D DQ-SQ spectra with large spectral widths

5.2.1 The problem

As explained in the previous section, supercycled pulse schemes are well suited for challenging recoupling experiments. However, a major drawback exists with regard to the acquisition of 2D homonuclear DQ-SQ correlation spectra, one of the most important applications of DQ recoupling.

When employing non-γ-encoded DQ recoupling sequences and hence most supercycled ones, the indirect evolution time (t_1) has to be rotor-synchronized in order to record clean spectra. This means that the maximum spectral width in the indirect (F_1) dimension is limited to the MAS frequency, which is often insufficient for nuclei with a broad chemical shift range. This limitation becomes even more severe at high magnetic fields, since the chemical shift dispersion in Hz is proportional to the magnetic field. For instance, a typical ^{13}C chemical shift range of 160 ppm requires a DQ chemical shift range of up to 320 ppm. This translates into a F_1 spectral width, and hence a required MAS frequency, of ≈ 32 kHz at 9.4 T, or ≈ 64 kHz at 18.8 T. Such high spinning frequencies are however incompatible with most DQ excitation schemes and/or the available probe hardware.

An insufficient F_1 spectral width results in signal folding in the DQ dimension whereas non-rotor-synchronized t_1 evolution gives rise to reconversion rotor-encoded DQ spinning sidebands,[164,165] in either way leading to difficulties in interpreting these more complex spectra. Note that this limitation can be circumvented for γ-encoded sequences by applying appropriate phase shifts to the DQ reconversion pulses (see the following section), allowing the choice of a t_1 increment of arbitrary length.[104,166–168]

This chapter will demonstrate that 2D DQ-SQ spectra with large F_1 spectral widths can be recorded with non-γ-encoded supercycled DQ recoupling sequences if they are derived from γ-encoded sequences. The method introduced here is based on Supercycle-Timing-Compensation (STiC) phase shifts. It enables 2D correlations in samples with a wide chemical shift range without limitations regarding the size of the DQ dimension, eliminating one of the biggest drawbacks of supercycling. This is of particular relevance for the recoupling of nuclei with large CSA and/or small dipolar couplings, where well-compensated sequences are required. A $^{13}\mathrm{C}-^{13}\mathrm{C}$ correlation spectrum recorded with the SR26 recoupling sequence and STiC phase shifts was thus also used to complete the assignment of dG(C3)$_2$ in section 2.2.2 (170 ppm ^{13}C chemical shift range, see Figure 2.2b). In the following, the concept and derivation of STiC phase shifts will be described, and its application will be demonstrated on the SR26 pulse scheme.

5.2.2 Large DQ spectral widths with γ-encoded recoupling sequences

The first-order average Hamiltonian of a spin interaction Λ with quantum numbers $\{l, m, \lambda, \mu\}$ can be written as

$$\overline{\mathcal{H}}^{\Lambda}_{lm\lambda\mu} = \kappa_{lm\lambda\mu} \left[A^{\Lambda}_{lm}\right]^{R} \exp\left[-im\left(\alpha^{0}_{RL} - \omega_r t^{0}\right)\right] T^{\Lambda}_{\lambda\mu}, \tag{5.4}$$

where $\kappa_{lm\lambda\mu}$ is the dipolar scaling factor, $\left[A^{\Lambda}_{lm}\right]^{R}$ represents the spatial tensor, expressed in the rotor-fixed frame, and $T^{\Lambda}_{\lambda\mu}$ represents the spin tensor, expressed in the laboratory frame. The complex phase factor describes the orientation of the rotor at the starting point t^0 of the recoupling sequence, with the Euler angle α^0_{RL} denoting the orientation of the rotor with respect to the laboratory frame at $t = 0$, and ω_r being the angular spinning frequency.

As it can be seen in equation 5.4, the phase of the average Hamiltonian varies due to sample rotation and therefore depends on the time point t^0. In addition, its phase also depends on the overall phase ϕ of the radiofrequency pulses of the recoupling sequence applied. These dependences can be expressed as

$$\overline{\mathcal{H}}^{\Lambda}_{lm\lambda\mu}(t^0, \phi) = \overline{\mathcal{H}}^{\Lambda}_{lm\lambda\mu}(0, 0) \exp\left[-i\left(\mu\phi - m\omega_r t^0\right)\right]. \tag{5.5}$$

From this equation, it follows that the dependence of $\overline{\mathcal{H}}^{\Lambda}_{lm\lambda\mu}$ on t^0 can be removed by applying an overall phase shift ϕ to the recoupling pulse sequence (if $\mu \neq 0$), as given by the phase-time-relationship[104,168]

$$\phi = \frac{m}{\mu}\omega_r t^0. \tag{5.6}$$

In general, the first-order average Hamiltonian of a given sequence is the sum of several allowed (non-zero) terms. Equation 5.6 can therefore only be applied if all of these terms possess the same ratio m/μ. This is for instance the case with γ-encoded DQ recoupling sequences, where $\{l, m, \lambda, \mu\} = \{2, m, 2, \pm 2\}$ and each spin term μ is only associated with one spatial term m (see also section 5.1.2).[156] For such sequences, the dependence on t^0 can be entirely removed by appropriate phase shifts.[104,168]

One of the most prominent applications of the relationship in equation 5.6 are 2D DQ-SQ homonuclear correlation experiments. A standard pulse sequence for recording such spectra consists of a DQ excitation block, followed by t_1 evolution and a DQ reconversion block, usually of the same length as the DQ excitation (Figure 5.2). The same Hamiltonian should ideally be created during DQ excitation and reconversion, in order to avoid MAS-induced modulation of signals in the indirect dimension:[164,165]

$$\overline{\mathcal{H}}_{\text{exc}} = \overline{\mathcal{H}}_{\text{rec}}, \tag{5.7}$$

and hence

$$\sum_{lm\lambda\mu} \overline{\mathcal{H}}^{\Lambda}_{lm\lambda\mu}\left(t^0_{\text{exc}}, \phi_{\text{exc}}\right) = \sum_{lm\lambda\mu} \overline{\mathcal{H}}^{\Lambda}_{lm\lambda\mu}\left(t^0_{\text{rec}}, \phi_{\text{rec}}\right), \tag{5.8}$$

where $t^0_{\text{rec}} = t^0_{\text{exc}} + t_1$. From equation 5.5, it is clear that this condition is fulfilled as long as the t_1 evolution is rotor-synchronized and ϕ_{rec} is only shifted by integer multiples of 180° with respect to ϕ_{exc} ($\mu = \pm 2$ in DQ recoupling).

If the t_1-evolution is not rotor-synchronized, equation 5.8 can still be fulfilled for γ-encoded recoupling sequences by shifting the phase of the DQ reconversion pulses according to equation 5.6:

$$\phi_{\text{rec}} = \phi_{\text{exc}} + \frac{m}{\mu}\omega_r\left(t^0_{\text{exc}} + t_1\right). \tag{5.9}$$

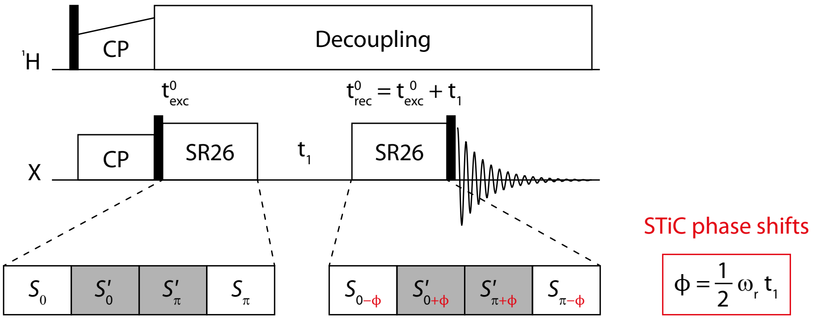

Figure 5.2: Pulse sequence for the acquisition of a 2D DQ-SQ correlation spectrum with SR26 used as dipolar recoupling sequence, with X being, e.g., ^{13}C, ^{15}N or ^{29}Si. STiC phase shifts ϕ (highlighted in red) have to be applied to the DQ reconversion RF pulses in order to allow the use of a t_1 increment of arbitrary length.

As explained above, this is only possible for γ-encoded recoupling sequences, because only these sequences have the same m/μ ratio in all allowed terms. In the following, it will be shown theoretically (section 5.2.3) and experimentally (section 5.2.4) that this concept can also be applied to recoupling sequences which are supercycles of γ-encoded sequences. DQ-SQ correlation spectra can then be recorded without restrictions regarding the length of the t_1-increments, and arbitrary spectral widths can be achieved in the DQ dimension. However, if a DQ recoupling sequence is neither γ-encoded nor a supercycle of a γ-encoded sequence, DQ-SQ experiments are restricted to rotor-synchronized t_1-evolution.

5.2.3 Large DQ spectral widths with non-γ-encoded recoupling sequences: STiC phase shifts

If two γ-encoded recoupling sequences A and B are combined to a non-γ-encoded supercycle AB, the effective Hamiltonian can be approximated as[91]

$$\overline{\mathcal{H}}^{AB} \cong \frac{1}{2}\left(\overline{\mathcal{H}}^{A} + \overline{\mathcal{H}}^{B}\right). \tag{5.10}$$

The average Hamiltonians of A and B are each a sum of their non-zero $\overline{\mathcal{H}}^{\Lambda}_{lm\lambda\mu}$ terms, with the dependence on t^0 and ϕ as given in equation 5.5:

$$\begin{aligned}\overline{\mathcal{H}}^{AB}\left(t^0,\phi^A,\phi^B\right) \cong \frac{1}{2}\Bigg(&\sum_{lm\lambda\mu}\overline{\mathcal{H}}^{\Lambda,A}_{lm\lambda\mu}(0,0)\exp\left[-i\left(\mu\phi^A - m\omega_r t^0\right)\right] + \\ &\sum_{lm\lambda\mu}\overline{\mathcal{H}}^{\Lambda,B}_{lm\lambda\mu}(0,0)\exp\left[-i\left(\mu\phi^B - m\omega_r t^0\right)\right]\Bigg).\end{aligned} \tag{5.11}$$

The same t^0 can be used for all terms, because sequences A and B are rotor-synchronized and therefore span an integer multiple of rotor periods. However, ϕ^A and ϕ^B can be different, because the two sequences are applied one after the other, i.e. not at the same point in time. For this reason, and because both sequences are γ-encoded (as defined above), $\overline{\mathcal{H}}^A$ and $\overline{\mathcal{H}}^B$ can both be made independent of t^0 by applying overall phase shifts ϕ^A and ϕ^B to the respective sequence blocks according to the phase-time relationship in equation 5.6. In consequence, $\overline{\mathcal{H}}^{AB}$ will be independent of t^0, too.

For the case of a 2D DQ-SQ correlation spectrum recorded with non-rotor-synchronized t_1 evolution, the phases of the DQ reconversion pulses therefore have to be shifted sequence-block-specifically in order to avoid MAS-induced signal modulations in the indirect dimension. These Supercycle-Timing-Compensation (STiC) phase shifts have to be

$$\Delta\phi^A = \phi^A_{\text{rec}} - \phi^A_{\text{exc}} = \frac{m_A}{\mu_A}\omega_r\left(t^0_{\text{exc}} + t_1\right), \tag{5.12}$$

$$\Delta\phi^B = \phi^B_{\text{rec}} - \phi^B_{\text{exc}} = \frac{m_B}{\mu_B}\omega_r\left(t^0_{\text{exc}} + t_1\right). \tag{5.13}$$

The SR26 sequence is one example where STiC phase shifts can be applied because each S element is γ-encoded. In a 2D DQ-SQ experiment with SR26 as dipolar recoupling sequence, the RF phases of the reconversion pulses have to be shifted according to equations 5.12 and 5.13, with S_0 and S_π being sequence A, and S'_0 and S'_π being sequence B. Based on the selection rule analysis in section 5.1.3 and defining $t^0_{\text{exc}} = 0$, the necessary STiC phase shifts are:

$$\Delta\phi\left(S_0\right) = \Delta\phi\left(S_\pi\right) = -\frac{1}{2}\omega_r t_1, \tag{5.14}$$

$$\Delta\phi\left(S'_0\right) = \Delta\phi\left(S'_\pi\right) = +\frac{1}{2}\omega_r t_1. \tag{5.15}$$

5.2.4 Experimental demonstration

Figure 5.3a demonstrates the successful application of STiC phase shifts in a ^{13}C$-^{13}$C DQ-SQ correlation experiment of a DNP-enhanced frozen solution of U-^{13}C,^{15}N-labeled L-histidine. The spectrum was taken at a spinning frequency of 7.8 kHz, employing the SR26 pulse sequence as given in Figure 5.2. A t_1 increment of 33.3 µs, which is much shorter than a rotor period ($\tau_r = 128.2$ µs), was used to achieve an F_1 spectral width of 30 kHz.

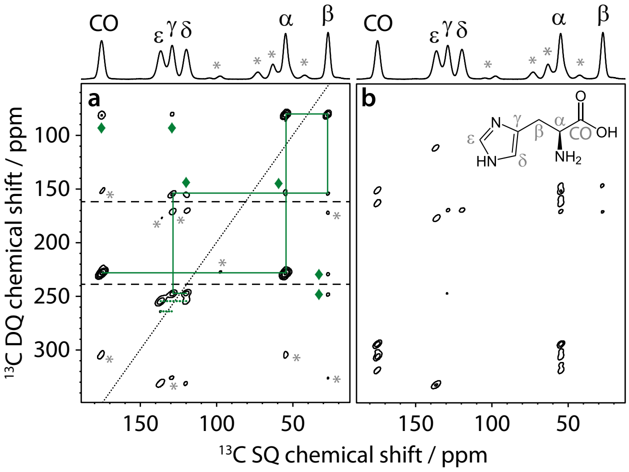

Figure 5.3: DNP-enhanced ^{13}C$-$^{13}C DQ-SQ correlation spectra of a frozen solution of U-^{13}C,^{15}N-L-histidine in 60:30:10 (v/v/v) D_8-glycerol/D_2O/H_2O, containing 10 mM AMUPol.[53] The pulse sequence shown in Figure 5.2 was used with (a) and without (b) STiC phase shifts. Spectra were acquired at 7.8 kHz MAS frequency (τ_r = 128.2 µs), using a t_1 dwell time of 33.3 µs (30 kHz F_1 spectral width) and a total recoupling time of 4.1 ms. Identical processing has been applied to both spectra, and the same contour levels are shown. Solid and dotted green lines in (a) illustrate direct one and two bond connections, respectively, and green diamonds indicate peaks originating from relayed transfers. Black horizontal dashed lines indicate the maximum F_1 spectral width feasible with rotor-synchronized t_1 evolution at the MAS frequency and magnetic field (9.4 T) used here. ^{13}C-CPMAS spectra are displayed above for illustrational purposes. Asterisks denote spinning sidebands and glycerol signals.

The spectrum is dominated by cross peaks between directly bonded carbons, located in F_1 at the sum of the chemical shifts of the respective correlated spins, and allows to establish carbon-carbon connectivities (green solid lines). In addition, peaks originating from relayed polarization transfer over two bonds can be observed (green diamonds), which is typical for dipolar recoupling experiments with longer mixing times in uniformly ^{13}C-labeled samples.[167] Direct polarization transfers over two bonds are only observed for correlations involving the isolated Cϵ with either Cγ or Cδ (green dotted lines).

For comparison, a spectrum taken with identical parameters, but without STiC phase shifts ($\Delta\phi = 0$), is shown in Figure 5.3b. Here, cross peaks are of lower intensity and do not appear at the expected DQ frequency, but rather at more than one DQ frequency for the same ^{13}C$-$^{13}C pair. The analysis of such a spectrum is practically impossible.

Due to its high robustness, the SR26 sequence is particularly well suited to the observation and measurement of long distances (> 3 Å), and thus the extraction of important structural information. As introduced before, such polarization transfer over long distances is greatly facilitated in samples with nuclei at low NA or with sparse isotopic labeling since dipolar truncation is greatly reduced. This case is exemplified in Figure 5.4 which shows a DNP-enhanced ^{13}C—^{13}C DQ-SQ correlation spectrum of the antibiotic ampicillin at its NA. The spectrum was recorded at a MAS frequency of 6 kHz, employing the SR26 sequence as shown in Figure 5.2. The large F_1 spectral width of 26.2 kHz was achieved by using a non-rotor-synchronized t_1 increment of 38.2 µs ($\tau_r = 166.7$ µs). Three repetitions of the full SR26 cycle were used for DQ excitation and reconversion each, resulting in a total recoupling time of 16 ms.

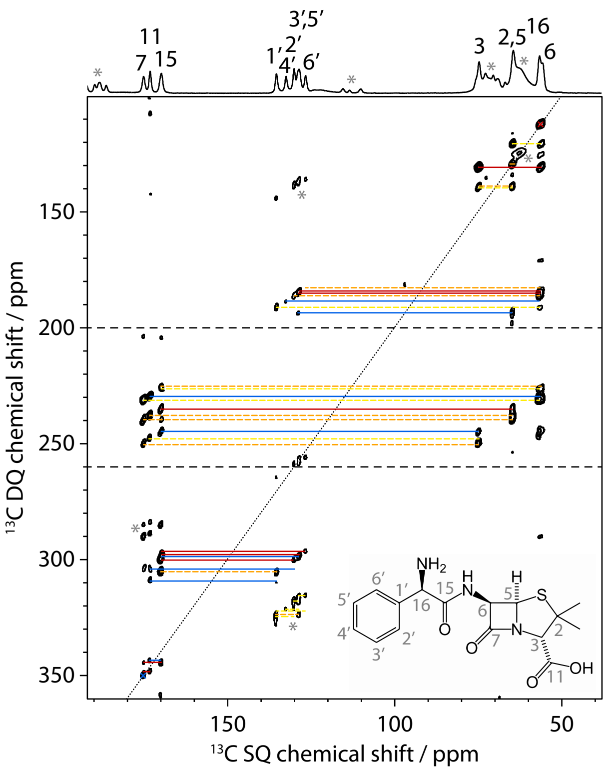

Figure 5.4: DNP-enhanced ^{13}C—^{13}C DQ-SQ correlation spectrum of NA ampicillin anhydrate, employing the SR26 sequence for dipolar recoupling as displayed in Figure 5.2. The spectrum was recorded at 6 kHz MAS frequency with a total recoupling time of 16 ms (see section 5.5 for experimental details). Yellow and orange dashed lines denote correlations corresponding to one and two bonds, respectively. Solid lines indicate longer intra- (red) and intermolecular (blue) correlations (3.1 to ≈ 4.3 Å).[169] Only the shortest distance contribution is marked for each pair of cross peaks. Black dashed lines indicate the maximum F_1 spectral width feasible with rotor-synchronized t_1 evolution at the MAS frequency and magnetic field (9.4 T) used here. A ^{13}C-CPMAS spectrum is displayed above for illustrational purposes, with resonance assignment taken from ref. 170. Asterisks denote spinning sidebands and signals from glycerol. The most intense aromatic-aromatic correlation peaks occur at the position of the $(\omega_{\mathrm{DQ}} + \omega_r)/2\pi$ spinning sideband in the indirect dimension, caused by insufficient averaging of their large CSA at 6 kHz MAS frequency. Correlations involving the methyl groups cannot be detected, which is often the case at measurement temperatures of ≈ 105 K.[171]

All expected correlations corresponding to one (≈ 1.5 Å) and two (≈ 2.5 Å) bond distances are present in the spectrum (yellow and orange dashed lines, respectively), but more importantly, numerous correlations over longer distances can be observed (red and blue solid lines). Comparison to the crystal structure[169] shows that they range from 3.1 Å to ≈ 4.3 Å. Notably, not only intramolecular contacts are detected (red), but also several intermolecular ones (blue), which provide information on the crystal packing of the substance. Many of these correlations involve carbonyl and/or aromatic carbons which is remarkable due to their large CSAs and demonstrates the good performance of the SR26 sequence.

In both examples presented here, the maximum F_1 spectral width that would have been attainable with rotor-synchronized t_1 evolution are marked by black horizontal dashed lines (Figure 5.3a and 5.4). It is obvious that a spectrum with such a small spectral width and hence folding of many cross peaks would be extremely difficult to interpret, even for the simple case of histidine. Furthermore, the spectra shown here were recorded at a relatively low magnetic field of 9.4 T. The available F_1 spectral width with rotor-synchronized t_1 evolution would be even smaller at higher magnetic fields.

5.3 DQ filtering efficiency above 52 %

5.3.1 DQF efficiency of different supercycles of R26

When different supercycles of the R26 sequence are applied for DQ recoupling experiments of large $^{13}\text{C}-^{13}\text{C}$ dipolar couplings, unexpected phenomena can be observed: The phase-inversion supercycle (S_0S_0') performs poorly compared to the single cycle S_0 or the full supercycle SR26 ($S_0S_0'S_\pi'S_\pi$). However, if the phases of all DQ reconversion pulses of the S_0S_0' sequence are inverted, its recoupling efficiency can be increased above 52 %, making it even more efficient than SR26. This is equal to inverting the order of cycles in the DQ reconversion, leading to a sequence which will in the following be denoted as $(S_0S_0')_{\text{exc}}(S_0'S_0)_{\text{rec}}$. This notation is short for $[(S_0S_0')_n]_{\text{exc}}[(S_0'S_0)_n]_{\text{rec}}$, meaning that n blocks of S_0S_0' are executed during DQ excitation, followed by n blocks of $S_0'S_0$ during DQ reconversion, with n being chosen according to the desired recoupling time.

The present section will show that these phenomena result from second-order terms between dipole-dipole interactions. These terms arise when supercycles are constructed by concatenating a regular cycle (S_0, S_π) with a phase-inverted one (S_0', S_π'), and can both reduce or increase the recoupling efficiency, depending on the order of cycles. A theoretical explanation along with numerical simulations and experimental demonstration will be given in the following.

5.3.2 Effective Hamiltonians of R26 supercycles

The effective Hamiltonian of a supercycle AB of sequences A and B can be approximated using the Baker-Campbell-Hausdorff (BCH) formula:[11]

$$\overline{\mathcal{H}}(AB) \cong \frac{1}{2}\left(\overline{\mathcal{H}}(A) + \overline{\mathcal{H}}(B)\right) + \frac{i}{4} n\tau_r \left[\overline{\mathcal{H}}(A), \overline{\mathcal{H}}(B)\right]. \tag{5.16}$$

This approximation is valid if all terms in A and B are small compared to the inverse of the cycle period $n\tau_r$. The first term in equation 5.16 is half the sum of the average Hamiltonians of the separate cycles, and will in the following be referred to as the first-order BCH term $\mathcal{H}^{(1)}_{\mathrm{BCH}}$. A detailed analysis of this term for supercycles of R26 has been carried out by Kristiansen *et al.*,[91] demonstrating how supercycling improves the robustness of the R26 sequence to chemical shift interactions and instrumental phase errors.

The first-order average Hamiltonians (ignoring the homonuclear J-coupling) of the different R26 cycles can be given as follows for two spins j and k:[91]

$$\overline{\mathcal{H}}^{(1)}(S_0) = \overline{\mathcal{H}}^{(1)}(S_\pi) = \overline{\mathcal{H}}_{\mathrm{DQ}}(S_0) = \frac{1}{2}\overline{\omega}^{jk}_{2-122} I_j^+ I_k^+ + \frac{1}{2}\overline{\omega}^{jk}_{212-2} I_j^- I_k^-, \tag{5.17}$$

$$\overline{\mathcal{H}}^{(1)}(S_0') = \overline{\mathcal{H}}^{(1)}(S_\pi') = \Pi_x \overline{\mathcal{H}}_{\mathrm{DQ}}(S_0)\Pi_x^\dagger = \frac{1}{2}\overline{\omega}^{jk}_{2122} I_j^+ I_k^+ + \frac{1}{2}\overline{\omega}^{jk}_{2-12-2} I_j^- I_k^-, \tag{5.18}$$

where $\overline{\omega}^{jk}_{lm\lambda\mu}$ denotes the complex amplitude of the respective symmetry-allowed term (equation 5.4), and $\Pi_x \overline{\mathcal{H}}_{\mathrm{DQ}}(S_0)\Pi_x^\dagger$ means that $\overline{\mathcal{H}}_{\mathrm{DQ}}(S_0)$ is rotated by π about the I_x^{DQ}-axis. To first order of the BCH expansion, the effective Hamiltonian of the SR26 sequence is therefore[91]

$$\mathcal{H}^{(1)}_{\mathrm{BCH}}(S_0 S_0') \cong \mathcal{H}^{(1)}_{\mathrm{BCH}}(\mathrm{SR26}) \cong \frac{1}{2}\left(\overline{\mathcal{H}}_{\mathrm{DQ}}(S_0) + \Pi_x \overline{\mathcal{H}}_{\mathrm{DQ}}(S_0)\Pi_x^\dagger\right) = \overline{\omega}_{\mathrm{SR26}} I_x^{\mathrm{DQ}}, \tag{5.19}$$

with the complex amplitude

$$\overline{\omega}_{\mathrm{SR26}} = -\frac{3}{2} b_{jk} |\kappa_{2-122}| \sin(2\beta^{jk}_{MR}) \cos(\gamma^{jk}_{MR} + \alpha^0_{RL} - \omega_r t^0), \tag{5.20}$$

and the DQ x-operator

$$I_x^{\mathrm{DQ}} = \frac{1}{2}\left(I_j^+ I_k^+ + I_j^- I_k^-\right). \tag{5.21}$$

The first-order BCH term of SR26 is identical to those of the supercycles S_0S_0', $S_0'S_0$, and their π-shifted equivalents.

The second term in equation 5.16 represents a correction to the first-order BCH term and will be denoted here as $\mathcal{H}^{(2)}_{\mathrm{BCH}}$. It involves commutators of the average Hamiltonians of sequences A and B and scales inversely with the MAS frequency. Assuming an ideal spin system without any interference from, e.g., chemical shift interactions, such a second-order BCH term only occurs for a phase-inversion supercycle because the first-order average Hamiltonians of S_0 (equation 5.17) and S_0' (equation 5.18) are not identical and the $I_j^+I_k^+$ and $I_j^-I_k^-$ operators do not commute:

$$\left[I_j^+I_k^+, I_j^-I_k^-\right] = 2I_z^{\mathrm{DQ}}, \tag{5.22}$$

with the DQ z-operator

$$I_z^{\mathrm{DQ}} = \frac{1}{2}\left(I_{jz} + I_{kz}\right). \tag{5.23}$$

Therefore, the second-order BCH term of S_0S_0' is

$$\mathcal{H}^{(2)}_{\mathrm{BCH}}(S_0S_0') \cong \frac{i}{4}n\tau_r\left[\overline{\mathcal{H}}(S_0), \overline{\mathcal{H}}(S_0')\right] \cong \frac{i}{8}n\tau_r\omega^{(2)}_{\mathrm{BCH}}I_z^{\mathrm{DQ}}, \tag{5.24}$$

with the amplitude

$$\omega^{(2)}_{\mathrm{BCH}} = \overline{\omega}^{jk}_{2-122}\overline{\omega}^{jk}_{2-12-2} - \overline{\omega}^{jk}_{212-2}\overline{\omega}^{jk}_{2122}. \tag{5.25}$$

The effective Hamiltonians of the S_0S_0', $S_0'S_0$, and $S_0S_0'S_0'S_0$ (equivalent to SR26 in an ideal spin system) sequences can then be approximated to the second order of the BCH expansion as

$$\overline{\mathcal{H}}(S_0S_0') \cong \overline{\mathcal{H}}(S_\pi S_\pi') \cong \overline{\omega}_{\mathrm{SR26}}I_x^{\mathrm{DQ}} + \frac{i}{8}n\tau_r\omega^{(2)}_{\mathrm{BCH}}I_z^{\mathrm{DQ}}, \tag{5.26}$$

$$\overline{\mathcal{H}}(S_0'S_0) \cong \overline{\mathcal{H}}(S_\pi'S_\pi) \cong \overline{\omega}_{\mathrm{SR26}}I_x^{\mathrm{DQ}} - \frac{i}{8}n\tau_r\omega^{(2)}_{\mathrm{BCH}}I_z^{\mathrm{DQ}}, \tag{5.27}$$

$$\overline{\mathcal{H}}(S_0S_0'S_0'S_0) \cong \overline{\mathcal{H}}(S_0S_0'S_\pi'S_\pi) \cong \overline{\omega}_{\mathrm{SR26}}I_x^{\mathrm{DQ}}. \tag{5.28}$$

Hence, the effective Hamiltonians of phase-inversion supercycles (S_0S_0' and $S_0'S_0$) receive a second-order contribution in the form of an effective field along the z-axis whose sign depends on the order of the sequence blocks. This can be expected to lead to reduced recoupling efficiencies. The size of this contribution increases with increasing dipolar coupling and decreasing MAS frequency. Concatenation of the two different phase-inversion supercycles to the $S_0S_0'S_0'S_0$ supercycle eliminates the second-order BCH terms (equation 5.28). This explains why the sequence order of SR26 ($S_0S_0'S_\pi'S_\pi$) is preferable over $S_0S_0'S_\pi S_\pi'$.

When a phase-inversion supercycle is inverted during DQ reconversion (as described for $(S_0S_0')_{\mathrm{exc}}(S_0'S_0)_{\mathrm{rec}}$ in section 5.3.1), different effective recoupling fields act during DQ excitation and reconversion. The BCH formula can no longer be safely applied over the whole cycle (DQ excitation plus reconversion) if the S_0S_0' and $S_0'S_0$ cycles are executed more than once, as results from experiment and simulation will show in the following sections. The consequences of this unusual situation will be illustrated in the following, demonstrating how increased recoupling efficiency can be achieved.

5.3.3 Visualization in the DQ subspace

The influence of the effective Hamiltonians in equations 5.26−5.28 on the DQ recoupling dynamics can be analyzed in the DQ subspace (Figure 5.5)[172,173] which is defined by the DQ spin operators I_x^{DQ} (equation 5.21), I_y^{DQ}, and I_z^{DQ} (equation 5.23), with

$$I_y^{\mathrm{DQ}} = \frac{1}{2i}\left(I_j^+ I_k^+ - I_j^- I_k^-\right). \tag{5.29}$$

These operators follow the rules of cyclic commutation:

$$\left[I_x^{\mathrm{DQ}}, I_y^{\mathrm{DQ}}\right] = iI_z^{\mathrm{DQ}}. \tag{5.30}$$

Figure 5.5 illustrates the DQ recoupling dynamics under three different recoupling sequences: The SR26 sequence (a), the S_0S_0' supercycle (b), and the $(S_0S_0')_{\mathrm{exc}}(S_0'S_0)_{\mathrm{rec}}$ supercycle (c). For each sequence, the first and second-order BCH terms as well as the effective Hamiltonians ($\overline{\mathcal{H}}_{\mathrm{eff}}$, dotted lines) are shown. For the SR26 sequence (Figure 5.5a), the effective field is along the I_x^{DQ}-axis because the second-order BCH term is eliminated by supercycling (equation 5.28). The S_0S_0' supercycle (Figure 5.5b) experiences an additional field along the I_z^{DQ}-axis which originates from the second-order BCH term (equation 5.26). The effective recoupling Hamiltonian is therefore the sum of the first- and second-order BCH terms and is tilted away from the transverse plane into the upper hemisphere (assuming a positive sign of the second-order contribution).

For both sequences discussed above, the same effective field is applied during DQ excitation and reconversion, which is the normal case in DQ recoupling experiments.

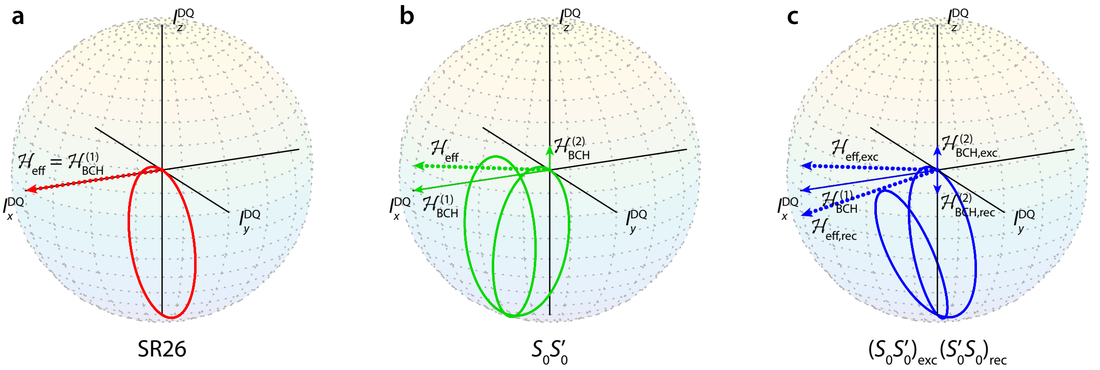

Figure 5.5: Visualization of DQ-filtered recoupling with the sequences SR26 (a), $S_0S'_0$ (b), and $(S_0S'_0)_{\mathrm{exc}}(S'_0S_0)_{\mathrm{rec}}$ (c) in the DQ subspace.[172,173] The first-order and second-order BCH terms ($\mathcal{H}_{\mathrm{BCH}}^{(1)}$, $\mathcal{H}_{\mathrm{BCH}}^{(2)}$) are shown as solid lines along the I_x^{DQ} and I_z^{DQ} axis, respectively, and the effective Hamiltonians ($\overline{\mathcal{H}}_{\mathrm{eff}}$) are shown as dotted lines. Thick solid lines denote the different positions of the spin vector after the full DQ-filtered experiment with different recoupling times.

In the $(S_0S'_0)_{\mathrm{exc}}(S'_0S_0)_{\mathrm{rec}}$ sequence (Figure 5.5c), however, the effective fields differ between excitiation and reconversion because the sign of the second-order BCH term is inverted during DQ reconversion (equation 5.27). Therefore, the effective Hamiltonians for DQ excitation ($\overline{\mathcal{H}}_{\mathrm{eff,exc}}$) and reconversion ($\overline{\mathcal{H}}_{\mathrm{eff,rec}}$) are tilted into the upper and lower hemisphere, respectively (again assuming a positive sign of the second-order term of $S_0S'_0$).

The process during a DQ-filtered recoupling experiment can be understood as follows. Before the start of the sequence, the spin vector is at $+1$ along the I_z^{DQ}-axis. When the effective recoupling field is applied, the spin vector rotates about $\overline{\mathcal{H}}_{\mathrm{eff}}$. After the DQ excitation period, it is projected onto the xy-plane by the DQ filtration process, and this transverse component is again rotated about $\overline{\mathcal{H}}_{\mathrm{eff}}$ during DQ reconversion. The DQF efficiency is obtained by projecting the spin vector at the end of this period onto the I_z^{DQ}-axis. 100 % efficiency is achieved when the vector is completely inverted, i.e. at -1 along the I_z^{DQ}-axis.

The position of the spin vector at the end of the DQ reconversion period is illustrated in Figure 5.5 by thick solid lines. Each point on the lines corresponds to a different recoupling time, i.e. to rotations through angles given by $|\omega_{\mathrm{eff}}\tau_{\mathrm{exc}}|$, with the same recoupling time used during DQ excitation and reconversion. In the case of SR26 (Figure 5.5a), a perfect circle in the lower hemisphere (with every point in the yz-plane) is obtained, meaning that the average DQF efficiency is 50 %. For the $S_0S'_0$ supercycle (Figure 5.5b), maximum recoupling efficiency is never achieved and part of the trajectory runs through the upper hemisphere. This indicates that a lower recoupling efficiency will be obtained. In contrast, the trajectory of the

$(S_0S_0')_{\mathrm{exc}}(S_0'S_0)_{\mathrm{rec}}$ sequence (Figure 5.5c) is tilted more into the lower hemisphere, and an increased recoupling efficiency can be expected compared to SR26. Note that these plots are meant to visualize the impact of different effective recoupling fields on the DQ recoupling dynamics and would correspond to only one crystallite orientation in a (real) powdered sample. Other crystallites would have different amplitudes of $\mathcal{H}^{(1)}_{\mathrm{BCH}}$ and $\mathcal{H}^{(2)}_{\mathrm{BCH}}$ due to their dependence on β^{jk}_{MR} and γ^{jk}_{MR}.

The average DQF efficiency $\overline{E}_{\mathrm{DQF}}$ for each sequence is obtained from projecting each point on the thick lines in Figure 5.5 onto the I_z^{DQ}-axis and taking the average of these values. For S_0S_0' and $(S_0S_0')_{\mathrm{exc}}(S_0'S_0)_{\mathrm{rec}}$, $\overline{E}_{\mathrm{DQF}}$ depends on the size of $\omega^{(2)}_{\mathrm{BCH}}$, i.e. on the size of the angle θ at which the effective recoupling axis is tilted away from the transverse plane:

$$\theta = \arctan\left(\frac{\left|\frac{in\tau_r}{8}\omega^{(2)}_{\mathrm{BCH}}\right|}{|\overline{\omega}_{\mathrm{SR26}}|}\right). \tag{5.31}$$

The average DQF efficiency for both sequences and its dependence on θ can then be calculated as

$$\overline{E}_{\mathrm{DQF}}(S_0S_0') = -\cos^2(\theta) + \frac{3}{2}\cos^4(\theta), \tag{5.32}$$

$$\overline{E}_{\mathrm{DQF}}((S_0S_0')_{\mathrm{exc}}(S_0'S_0)_{\mathrm{rec}}) = 2\cos^2(\theta) - \frac{3}{2}\cos^4(\theta). \tag{5.33}$$

Figure 5.6 plots $\overline{E}_{\mathrm{DQF}}$ as a function of θ (with constant $\overline{\omega}_{\mathrm{SR26}}$) for the sequences SR26, S_0S_0', and $(S_0S_0')_{\mathrm{exc}}(S_0'S_0)_{\mathrm{rec}}$. For SR26 (red line), there is no second-order contribution, meaning that $\overline{E}_{\mathrm{DQF}}$ does not depend on θ and is always 50 %. As expected, the efficiency drops below 50 % for the S_0S_0' supercycle (green line) as soon as $\theta \neq 0$, meaning that the influence of the second-order BCH term always decreases the recoupling efficiency. The most interesting case is the $(S_0S_0')_{\mathrm{exc}}(S_0'S_0)_{\mathrm{rec}}$ supercycle (blue line). Within a certain range of θ-angles ($0° < \theta < 54.7°$), the average efficiency does indeed exceed 50 %, reaching a maximum of 66.7 % for $\theta \approx 35.3°$. If θ becomes larger than 54.7°, the recoupling efficiency drops below 50 %.

While the situation in a powdered sample will be more complex owing to different θ values for each crystallite, Figure 5.6 does demonstrate that it is possible to exceed average recoupling efficiencies of 50 % when the DQ recoupling fields applied during DQ excitation and reconversion have different orientations and the θ angles lie within a certain range. Considering the R26 supercycles, this means that sequences with increased DQF efficiencies can be constructed by appropriate use of the phase

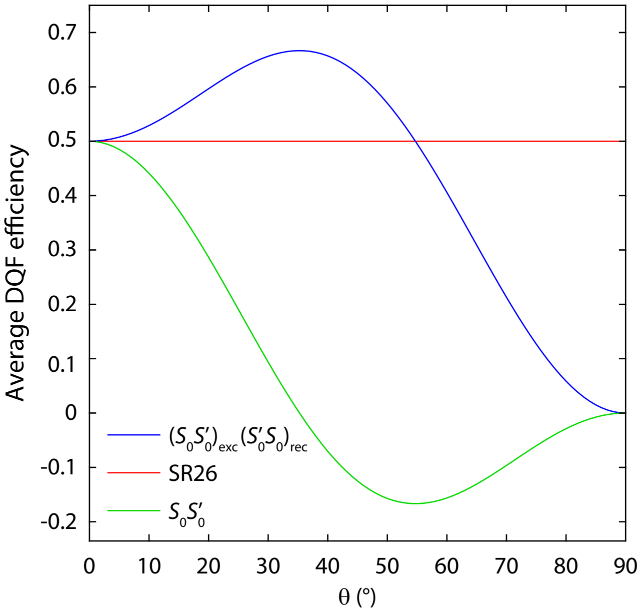

Figure 5.6: Theoretical average DQF efficiency of recoupling sequences $(S_0S'_0)_{\mathrm{exc}}(S'_0S_0)_{\mathrm{rec}}$ (blue), SR26 (red), and $S_0S'_0$ (green), depending on the angle θ between the effective recoupling field and the transverse plane in the DQ subspace. The efficiences of $S_0S'_0$ and $(S_0S'_0)_{\mathrm{exc}}(S'_0S_0)_{\mathrm{rec}}$ were calculated from equation 5.32 and 5.33, respectively.

inversion supercycle. More precisely, the $S_0S'_0$ and the $S_\pi S'_\pi$ supercycle each create an effective recoupling field in one hemisphere of the DQ subspace, whereas their permuted forms S'_0S_0 and $S'_\pi S_\pi$ create an effective field in the other hemisphere. Accordingly, increased DQF efficiencies can be achieved with the $(S_0S'_0)_{\mathrm{exc}}(S'_0S_0)_{\mathrm{rec}}$ supercycle described above, and also by rearranging the elements of the SR26 supercycle into $(S_0S'_0S_\pi S'_\pi)_{\mathrm{exc}}(S'_0S_0S'_\pi S_\pi)_{\mathrm{rec}}$. The latter sequence does not only profit from increased DQF efficiency, but also from the good compensation of chemical shift terms which is achieved by the full supercycle.

5.3.4 Numerical simulations

The performance of the different supercycles proposed above was evaluated by numerical simulations with SPINEVOLUTION,[112] simulating the DQF efficiency which can be obtained in a ^{13}C$-$^{13}C spin pair. The S_0 (R26) sequence and its supercycles $S_0S'_0$ and $S_0S'_0S'_\pi S_\pi$ (SR26) were tested along with the sequences with phase-inverted DQ reconversion, $(S_0S'_0)_{\mathrm{exc}}(S'_0S_0)_{\mathrm{rec}}$ and $(S_0S'_0S_\pi S'_\pi)_{\mathrm{exc}}(S'_0S_0S'_\pi S_\pi)_{\mathrm{rec}}$.

Figure 5.7 compares the buildups of DQF efficiency for a short distance which corresponds to a carbon-carbon one-bond distance (1.5 Å: a,c) and for a longer distance (4.0 Å: b,d). For both distances, simulations were run with (c,d) and without (a,b) chemical shift interactions (see Figure caption for details).

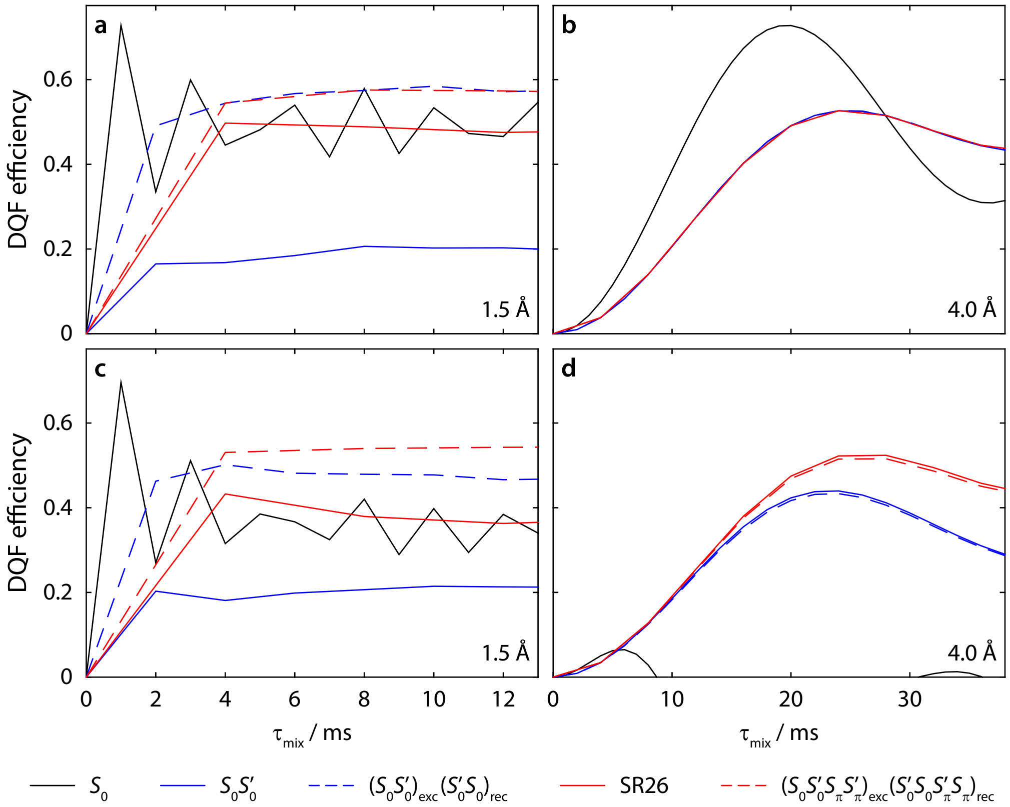

Figure 5.7: SPINEVOLUTION[112] simulations of DQF efficiency in a ^{13}C$-^{13}$C spin system, using dipolar recoupling sequences S_0 (black), S_0S_0' (blue solid lines), $(S_0S_0')_{\text{exc}}(S_0'S_0)_{\text{rec}}$ (blue dashed lines), SR26 (red solid lines), and $(S_0S_0'S_\pi S_\pi')_{\text{exc}}(S_0'S_0S_\pi'S_\pi)_{\text{rec}}$ (red dashed lines). Simulations were run for a short (1.5 Å: a,c) and a long (4.0 Å: b,d) carbon-carbon distance, comparing an ideal spin system (a,b) to a spin system with chemical shift interactions in the form of resonance offset Ω and CSA (c,d). Further simulation parameters: $\omega_r/2\pi = 8\,\text{kHz}$, $B_0 = 9.4\,\text{T}$, $\Omega_1 = 50\,\text{ppm}$, $\sigma_{\text{aniso},1} = 180\,\text{ppm}$, $\eta_1 = 0.3$, $\Omega_2 = -50\,\text{ppm}$, $\sigma_{\text{aniso},2} = 135\,\text{ppm}$, $\eta_2 = 0.9$.

The single cycle S_0 (black solid lines) shows the expected behavior of a γ-encoded recoupling sequence.[156] In an ideal spin system, the maximum DQF efficiency is $\approx 73\,\%$ and strong oscillations can be observed (a, b). The recoupling performance of the sequence deteriorates when chemical shift interactions are present (c,d), which is particularly obvious for the longer distance (d).

The full SR26 sequence (red solid lines) also shows the expected behavior. Its maximum recoupling efficiency is $\approx 52\,\%$ in an ideal spin system (a,b), and is still very high when strong chemical shift interactions are present (c,d), notably also over longer distances (d).

As predicted, the phase-inversion supercycle S_0S_0' (blue solid line) is very inefficient for the short distance, with DQF efficiencies only reaching $\approx 20\,\%$, both with and without chemical shift interactions (a, b). At longer distances however, it performs much better, being equivalent to SR26 in an ideal spin system (c). This shows that the dipolar coupling for a 4.0 Å distance is so small that it does not lead to a sizable second-order contribution to the effective Hamiltonian. When chemical shift interactions are present (d), the S_0S_0' supercycle still performs well, but not as well as the full supercycle of SR26.

Following the considerations above, the supercycles with phase-inverted reconversion ($(S_0S_0')_{\mathrm{exc}}(S_0'S_0)_{\mathrm{rec}}$, blue dashed lines, and $(S_0S_0'S_\pi S_\pi')_{\mathrm{exc}}(S_0'S_0S_\pi'S_\pi)_{\mathrm{rec}}$, red dashed lines) are expected to increase the recoupling efficiency at short distances, but not at long ones. Indeed, both sequences exhibit higher recoupling efficiencies than SR26 for the 1.5 Å distance (a,c, up to ≈ 58 %). Even when chemical shift interactions are included, recoupling efficiencies above 50 % can be achieved with the full $(S_0S_0'S_\pi S_\pi')_{\mathrm{exc}}(S_0'S_0S_\pi'S_\pi)_{\mathrm{rec}}$ cycle.

For the 4.0 Å distance, the curves obtained with sequences that have phase-inverted DQ reconversion ($(S_0S_0')_{\mathrm{exc}}(S_0'S_0)_{\mathrm{rec}}$ and $(S_0S_0'S_\pi S_\pi')_{\mathrm{exc}}(S_0'S_0S_\pi'S_\pi)_{\mathrm{rec}}$) are nearly identical to those obtained with the regular S_0S_0' and SR26 sequences in which DQ excitation and reconversion are the same. This again supports the theory that second-order BCH terms, resulting from cross terms of dipole-dipole interactions, lead to increased DQF efficiency at short distances, but become too small to have an effect at longer distances.

To further confirm this explanation, the same simulations as in Figure 5.7a were performed at faster MAS frequencies of 20 kHz and 40 kHz. Since the size of the second order BCH term decreases with increasing spinning frequency (equation 5.16), the differences between the sequences can be expected to become smaller. Indeed, they are reduced at 20 kHz MAS frequency (Figure 5.8a). At 40 kHz, all sequences except the γ-encoded S_0 cycle exhibit almost the same buildup of DQF efficiency (Figure 5.8b).

5.3.5 Experiments

The theoretical considerations and numerical simulations were verified experimentally on DNP-enhanced frozen solutions of U-^{13}C,^{15}N-labeled glycine and on 1,6-^{13}C-labeled D-glucose. U-^{13}C,^{15}N-glycine represents a molecule with a one-bond carbon-carbon distance of ≈ 1.5 Å. The distance between the labeled carbons in 1,6-^{13}C-D-glucose is much longer with ≈ 3.7 Å. Owing to the low concentration of analyte in the respective solutions, the molecules can be considered to be isolated

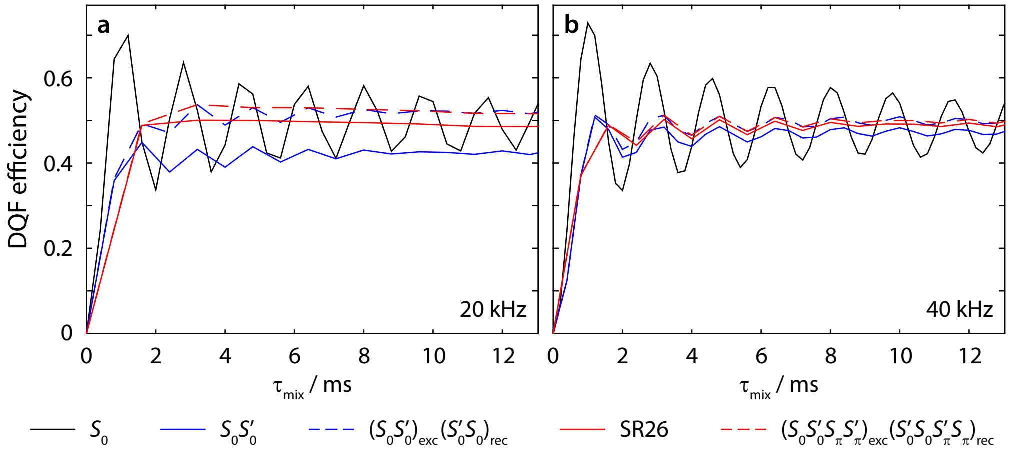

Figure 5.8: SPINEVOLUTION simulations of DQF efficiency in a ^{13}C$-^{13}$C spin system ($r_{jk} = 1.5\,\text{Å}$), using dipolar recoupling sequences S_0 (black), S_0S_0' (blue solid lines), $(S_0S_0')_{\mathrm{exc}}(S_0'S_0)_{\mathrm{rec}}$ (blue dashed lines), SR26 (red solid lines), and $(S_0S_0'S_\pi S_\pi')_{\mathrm{exc}}(S_0'S_0S_\pi'S_\pi)_{\mathrm{rec}}$ (red dashed lines). The MAS frequency was set to 20 kHz (a) or 40 kHz (b), respectively. All other parameters are identical to the ones used for simulations in Figure 5.7a.

and no intermolecular polarization transfer is expected. However, different molecular conformations are present as a consequence of freezing the solution, meaning that a certain distribution of distances may occur. This is however not an issue for the experiments shown here because all sequences were applied on the same sample, meaning that the same distance distributions were present.

Figures 5.9a and b show the DQF spectra obtained on U-^{13}C,^{15}N-glycine and on 1,6-^{13}C-D-glucose, respectively, with the sequences S_0 (black), S_0S_0' (light blue), $(S_0S_0')_{\mathrm{exc}}(S_0'S_0)_{\mathrm{rec}}$ (blue), SR26 (orange), and $(S_0S_0'S_\pi S_\pi')_{\mathrm{exc}}(S_0'S_0S_\pi'S_\pi)_{\mathrm{rec}}$ (red). All glycine spectra were acquired with a total recoupling time of 4 ms, at which a one-bond distance is fully built-up. The glucose spectra shown in Figure 5.9b were recorded with a recoupling time of 12 ms, corresponding to three full cycles of SR26. Splitting of the C1 and C6 resonances can be observed owing to the presence of α- and β-anomers of glucose.[174] The same data set as shown in Figure 5.9b was also recorded with shorter mixing times of 4 ms and 8 ms.

For an easier interpretation of the spectra, the corresponding peak integrals are plotted in Figures 5.9c and d, displaying the expected behaviour for both samples: The sequences with phase-inverted reconversion clearly perform better than SR26 in U-^{13}C,^{15}N-glycine, which has a short ^{13}C$-^{13}$C distance (Figure 5.9c). On the other hand, no such difference can be observed in 1,6-^{13}C-D-glucose in which only a long ^{13}C$-^{13}$C distance is present (Figure 5.9d). Here, the regular supercycles and the corresponding phase-inverted ones yield essentially the same signal intensities. More-

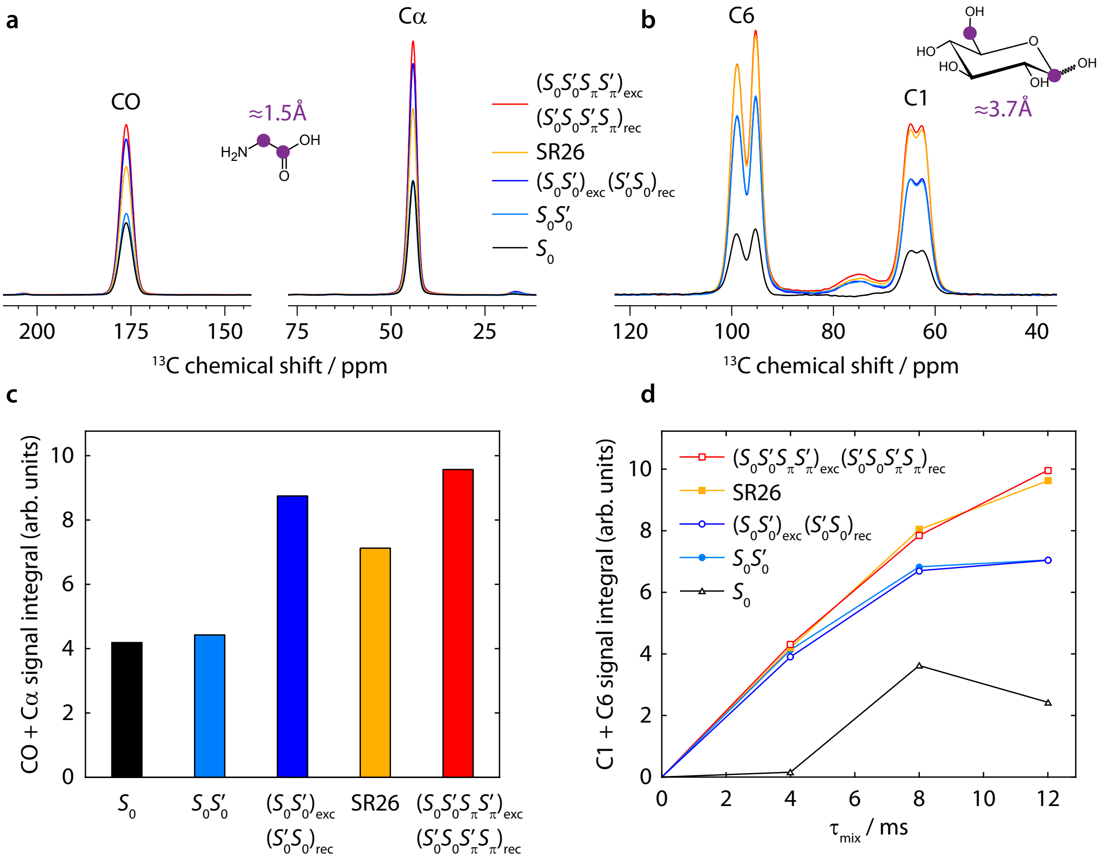

Figure 5.9: Experimental results obtained on DNP-enhanced frozen solutions of U-^{13}C,^{15}N-glycine (a,c) and 1,6-^{13}C-D-glucose (b,d) in 60:30:10 (v/v/v) D_8-glycerol/D_2O/H_2O, containing 10 mM AMUPol.[53] (a,b) ^{13}C spectra of glycine (a) and glucose (b) acquired in DQ-filtered recoupling experiments. The sequences $(S_0S'_0S_\pi S'_\pi)_{\text{exc}}(S'_0S_0S'_\pi S_\pi)_{\text{rec}}$ (red), SR26 (orange), $(S_0S'_0)_{\text{exc}}(S'_0S_0)_{\text{rec}}$ (blue), $S_0S'_0$ (light blue), and S_0 (black) were used with with total recoupling times of 4 ms (a) and 12 ms (b), respectively. The spectra were recorded at 8 kHz MAS frequency. (c,d) Signal integrals of the respective recoupling experiments shown above (a,b). The glucose experiments were repeated with recoupling times of 4 ms and 8 ms, the results of which are shown in (d), too.

over, in both samples, the full supercycles with phase-inversion and π-shifted cycles provide more efficient recoupling than the half-supercycles with phase-inversion only. The S_0 cycle is the least efficient in both samples, demonstrating the necessity of supercycling for robust recoupling.

Overall, simulations and experiments have shown that the sequences with phase-inverted reconversion ($(S_0S'_0)_{\text{exc}}(S'_0S_0)_{\text{rec}}$ and $(S_0S'_0S_\pi S'_\pi)_{\text{exc}}(S'_0S_0S'_\pi S_\pi)_{\text{rec}}$) yield significantly improved DQF efficiencies at short carbon-carbon distances, while still profiting from the same robustness as the original cycles. Consequently, the $(S_0S'_0S_\pi S'_\pi)_{\text{exc}}(S'_0S_0S'_\pi S_\pi)_{\text{rec}}$ sequence could be employed instead of SR26 without compromising its excellent compensation for chemical shift interactions. While the

$(S_0S'_0)_{\mathrm{exc}}(S'_0S_0)_{\mathrm{rec}}$ sequence is more susceptible to chemical shift interference than $(S_0S'_0S_\pi S'_\pi)_{\mathrm{exc}}(S'_0S_0S'_\pi S_\pi)_{\mathrm{rec}}$, it allows smaller sampling intervals due to its shorter cycle time. Hence, a single $(S_0S'_0)_{\mathrm{exc}}(S'_0S_0)_{\mathrm{rec}}$ cycle could be considered for recording $^{13}\mathrm{C}-^{13}\mathrm{C}$ correlation spectra for assignment purposes, because only cross-peaks of directly bonded carbons will be fully built-up at this relatively short recoupling time.

5.4 Conclusions

This chapter has presented improvements for supercycled symmetry-based recoupling sequences, exemplified on the SR26 sequence. It tackles some of the drawbacks which arise from supercycling of γ-encoded pulse sequences and the associated loss of the γ-encoding property.

Section 5.2 presented a method for recording 2D DQ-SQ correlation spectra with arbitrary F_1 spectral widths when employing the SR26 sequence. It is based on applying STiC phase shifts to the DQ reconversion pulses in order to compensate for non-rotor-synchronized t_1 evolution, extending the concept known for γ-encoded sequences. Consequently, all correlation peaks of samples with a large chemical shift range can be obtained without signal folding in the indirect dimension, but also experimental time can be saved when an F_1 spectral width smaller than the MAS frequency is sufficient. The recoupling performance of SR26 remains unchanged, meaning that all benefits of this well-compensated sequence can be exploited, as for example for the recoupling of nuclei with large CSA, and for the detection of long distance correlations for structural studies. This will be particularly useful for MAS-DNP applications involving the acquisition of 2D correlation spectra of dilute spins, as demonstrated here by a long-range $^{13}\mathrm{C}-^{13}\mathrm{C}$ correlation spectrum of NA ampicillin. The general principle of applying different t_1-dependent phase shifts to each element of a supercycle is applicable to any conventional supercycle of a γ-encoded sequence.

In section 5.3, the influence of second-order BCH terms which arise from creating phase-inversion supercycles has been investigated. They lead to reduced recoupling efficiency in the half-supercycles ($S_0S'_0$ or $S_\pi S'_\pi$), but can be eliminated by concatenation with a permuted cycle (S'_0S_0 or $S'_\pi S_\pi$), as it is the case in the SR26 sequence. In addition, the recoupling efficiency can even be increased over the theoretical maximum of a non-γ-encoded sequence ($\approx 52\,\%$) when phase-inversion is applied to the DQ reconversion pulses. This effect occurs because different effective recoupling fields are acting during DQ excitation and reconversion. Two sequences which take advantage of this effect were presented, the $(S_0S_0')_{\mathrm{exc}}(S_0'S_0)_{\mathrm{rec}}$ sequence and the $(S_0S_0'S_\pi S_\pi')_{\mathrm{exc}}(S_0'S_0S_\pi'S_\pi)_{\mathrm{rec}}$ sequence. The latter benefits not only from increased efficiency for recoupling ^{13}C spins at short distances, but also from the robustness of the SR26 sequence, which makes it a viable alternative to SR26. Of course, STiC phase shifts can also be applied for recording 2D DQ-SQ spectra with these modified cycles.

The influence of the second-order contribution to the effective Hamiltonian of the $(S_0S_0')_{\mathrm{exc}}(S_0'S_0)_{\mathrm{rec}}$ and $(S_0S_0'S_\pi S_\pi')_{\mathrm{exc}}(S_0'S_0S_\pi'S_\pi)_{\mathrm{rec}}$ supercycles can only be observed when large dipolar couplings and relatively slow MAS frequencies are involved. For example, it is very pronounced for directly bonded $^{13}\mathrm{C}-^{13}\mathrm{C}$ spins pairs at typical MAS frequencies employed in SR26 recoupling experiments ($\approx 8\,\mathrm{kHz}$), but cannot be observed when the carbon-carbon distance is increased to more than 3 Å. For experiments on nuclei other than ^{13}C, the increased recoupling efficiency can be expected to occur in a different range of distances and spinning frequencies that will depend on the gyromagnetic ratio of the recoupled nuclei.

Numerical simulations show that the use of phase-inverted DQ reconversion pulses is beneficial for phase-inversion supercycles of other γ-encoded recoupling sequences, too. Hence, more applications of this approach can still be explored. Moreover, the general concept of employing recoupling fields of different orientations during the first and second half of the recoupling period could offer a way to also turn the deleterious influence of other higher-order cross terms into positive effects.

5.5 Materials and methods

DNP sample preparation

A 10 mM solution of AMUPol[53] in 60:30:10 (v/v/v) D_8-glycerol/D_2O/H_2O was used for the preparation of all DNP samples used in this chapter.

For the histidine sample (section 5.2.4), 1.5 mg U-^{13}C,^{15}N-L-histidine · HCl · H_2O were dissolved in 30 µL of the AMUPol solution. 15 µL of this solution were transferred into a thick-wall zirconia rotor. For the ampicillin sample (section 5.2.4), ≈ 50 mg of ampicillin anhydrate were impregnated with 27 µL of the AMUPol solution and filled into a thin-wall zirconia rotor.

For the glycine sample used in section 5.3.5, 1.6 mg U-^{13}C,^{15}N-glycine were dissolved in 25 µL of the AMUPol solution, and ≈ 20 µL of this solution were transferred into a sapphire rotor. The glucose sample was prepared in the same way, employing 1.8 mg 1,6-^{13}C-D-glucose.

NMR experimental details

All DNP experiments were performed on the MAS-DNP system described in section 2.4. ^{1}H and ^{13}C $\pi/2$ pulses were applied at RF field strengths of 100 kHz and 50 kHz, respectively. The initial polarization transfer from ^{1}H to ^{13}C was achieved by cross polarization (CP), with an RF field strength of 50 kHz on ^{13}C and a $80-100\%$ linear ramp around the $n = +1$ Hartmann-Hahn condition on ^{1}H. Heteronuclear decoupling at $\approx$ ^{1}H RF field strengths of 100 kHz was achieved using SPINAL-64[21] during free evolution periods and CW[16] or CW-LG[96] decoupling during ^{13}C$-$^{13}C homonuclear recoupling periods

The 2D DQ-SQ spectra in section 5.2.4 were acquired with the pulse sequence shown in Figure 5.2. A 100 µs z-filter was inserted before the flip-down pulse for detection. Frequency discrimination in the indirect dimension was achieved using the States-TPPI method.[95]

The histidine spectra were recorded at a MAS frequency of 7.8 kHz and with a recycle delay of 2 s. The SR26 sequence was applied at an RF field strength of 50.7 kHz on ^{13}C. One full SR26 cycle was used for DQ excitation and reconversion each, resulting in a total mixing time of 4.1 ms. Acquisition times were 10 ms in the direct and 2.1 ms in the indirect dimension, and 64 complex t_1 points were recorded with 16 transients per point. The dwell time in the indirect dimension was set to 33.33 µs, resulting in a spectral width of 30 kHz (298 ppm). The spectrum in Figure 5.3a was recorded with STiC phase shifts, whereas the spectrum in Figure 5.3b was recorded without these phase shifts but with otherwise identical parameters. Prior to Fourier transform, data were zero-filled in both dimensions and apodized with 50 Hz exponential line-broadening in the direct dimension only. The total experimental time was $\approx$ 1 h 10 min per spectrum.

The ampicillin spectrum was recorded at a MAS frequency of 6 kHz and with a recycle delay of 11.7 s. The SR26 sequence was applied at an RF field strength of 39 kHz on ^{13}C, and three full cycles were used for DQ excitation and reconversion each, corresponding to a total mixing time of 16.0 ms. 67 complex t_1 points were acquired with 16 transients per point and the application of STiC phase shifts. Acquisition times were 20 ms in the direct and 2.6 ms in the indirect dimension. The dwell time in the indirect dimension was set to 38.2 µs, resulting in a spectral width of 26.2 kHz (260 ppm). Prior to Fourier transform, data were zero-filled and apodized with 50 Hz exponential line-broadening in both dimensions. The total experimental time was ≈ 7 h.

The spectra in section 5.3.5 were recorded with a 1D DQ-filtered ^{13}C$-$^{13}C recoupling experiment at a MAS frequency of 8 kHz. Experiments were run with the recoupling sequences shown in Figure 5.9, each applied at a ^{13}C RF field strength of 52 kHz. 32 transients were recorded for each spectrum with an acquisition time of 10 ms. The glycine spectra were recorded with a recycle delay of 3.25 s and with a total recoupling time of 4 ms. The glucose spectra were recorded with a recycle delay of 3.77 s. Three sets of spectra were acquired for this sample with total recoupling times of 4, 8, and 12 ms. All spectra were processed without any apodization.

Conclusions and outlook

This work has provided the framework for a novel concept of NMR-based 3D structure determination of organic solids. Its central point is the deliberate use of samples which contain ^{13}C and ^{15}N at their natural isotopic abundance (NA), while employing MAS-DNP to compensate for the reduced sensitivity.

The approach exploits the unique advantage of experiments on NA samples which is the almost full suppression of dipolar truncation effects. Consequently, long distance polarization transfers up to $\approx 7\,\text{Å}$ are possible as well as the simultaneous undisturbed observation of different distances for the same spin pair and the detection of intermolecular contacts. In addition, this work demonstrated that the theoretical treatment and simulation of the occurring spin dynamics can be reduced to isolated spin pairs and is therefore straightforward and simple.

^{13}C$-$^{13}C and ^{13}C$-$^{15}N polarization buildup curves obtained from dipolar recoupling experiments under such conditions are the heart of this approach to NMR crystallography. They fully benefit from the factors described above, meaning that they contain a large number of intra- and intermolecular distance contributions which provide direct structural information. The numerical simulation of such curves is simple, accurate and fast. These properties make polarization buildup curves recorded at NA an ideal tool for evaluating structural models by comparing the experimental data to simulations based on the respective model. The combination of this evaluation step with an efficient structure optimization or search algorithm provides a very powerful protocol for structure determination.

This thesis has proven the feasibility of the concept described above, demonstrating the acquisition of polarization buildup curves with different strategies, their detailed analysis, and their combination with computational structural search. Ultimately, both the molecular and supramolecular structure of cyclo-FF were obtained by mainly relying on the NMR buildup curves. This underlines the power of MAS-DNP for structure determination and the great potential for NMR crystallography which lies in the approach described above.

For the future, this approach has of course to be validated on other samples to make it available for studies on samples with unknown structure. In this context, the development of the computational side should clearly be pursued. Different possibilities can be considered for structural optimization, be it a systematic search or a search driven by energy minimization. The goal should be to develop generalized computational strategies which can be applied efficiently to many different organic samples.

Exploiting more sources of structural information is also desirable to make structural search more efficient and reliable. One such source is of course powder XRD data which, if available, should certainly be integrated in structure determination protocols. In addition, further NMR experiments can be considered, such as the measurement of tensor orientations which can be exploited if the sensitivity is high enough. By correlating dipolar and/or CSA interaction tensors, information on the local conformation such as torsion angles can be obtained. Given that the discrimination of intra- and intermolecular distance contributions to polarization buildup curves is very challenging, such measurements could nicely complement the distance measurements and be a valuable resource for determining the molecular conformation.

Last but not least, the prerequisite of such studies is that efficient DNP and hence good enough sensitivity enhancement can be achieved in the sample of interest. This is not always straightforward, for instance owing to large particle sizes and/or unfavourable relaxation properties of the sample. Moreover, poor spectral resolution or altering of the investigated structure under DNP conditions can pose serious problems which require improvements in sample preparation protocols. Overall, the field of MAS-DNP is still developing rapidly and progress in all areas can be expected in the coming years, especially for further sensitivity enhancement. For example, the theoretical understanding and numerical simulation of the DNP process is still improving and can give inspiration for the development of more efficient radicals.[58] Moreover, hardware developments aim at enabling sustainable sample spinning with helium gas for reaching lower sample temperatures and/or faster spinning frequencies.[52,131] This can provide another boost for sensitivity.

In summary, the general concepts demonstrated in this thesis reveal a new avenue for NMR crystallography and can be expected to enable *de novo* structure determination based on distance information from NMR in the future.

Bibliography

[1] V. Ladizhansky. *Biochim. Biophys. Acta - Proteins Proteomics* 1865 (2017), 1577–1586.

[2] B. H. Meier, R. Riek, and A. Böckmann. *Trends Biochem. Sci.* 42 (2017), 777–787.

[3] P. Schanda and M. Ernst. *Prog. Nucl. Magn. Reson. Spectrosc.* 96 (2016), 1–46.

[4] E. Ravera, T. Martelli, Y. Geiger, M. Fragai, G. Goobes, and C. Luchinat. *Coord. Chem. Rev.* 327-328 (2016), 110–122.

[5] C. Bonhomme, C. Gervais, and D. Laurencin. *Prog. Nucl. Magn. Reson. Spectrosc.* 77 (2014), 1–48.

[6] S. E. Ashbrook, D. M. Dawson, and V. R. Seymour. *Phys. Chem. Chem. Phys.* 16 (2014), 8223–8242.

[7] D. Massiot, R. J. Messinger, S. Cadars, M. Deschamps, V. Montouillout, N. Pellerin, E. Veron, M. Allix, P. Florian, and F. Fayon. *Acc. Chem. Res.* 46 (2013), 1975–1984.

[8] T. Bräuniger and M. Jansen. *Zeitschrift für Anorg. und Allg. Chemie* 639 (2013), 857–879.

[9] M. Levitt. *Spin Dynamics: Basics of Nuclear Magnetic Resonance.* 2nd ed. Chichester, UK: John Wiley & Sons, Ltd, 2008.

[10] M. J. Duer. *Solid-State NMR Spectroscopy Principles and Applications.* 1st ed. Oxford, UK: Blackwell Science Ltd, 2001.

[11] U. Haeberlen. *High Resolution NMR in Solids, Selective Averaging.* New York: Academic Press, 1976.

[12] E. Pretsch, P. Bühlmann, and M. Badertscher. *Structure determination of organic compounds : tables of spectral data.* 4th ed. Berlin, Heidelberg: Springer, 2009.

[13] S. K. Straus, T. Bremi, and R. R. Ernst. *Chem. Phys. Lett.* 262 (1996), 709–715.

[14] E. R. Andrew, A. Bradbury, and R. G. Eades. *Nature* 182 (1958), 1659–1659.

[15] I. J. Lowe. *Phys. Rev. Lett.* 2 (1959), 285–287.

[16] A. L. Bloom and J. N. Shoolery. *Phys. Rev.* 97 (1955), 1261–1265.

[17] A. Pines, M. G. Gibby, and J. S. Waugh. *J. Chem. Phys.* 56 (1972), 1776–1777.

[18] J. Schaefer and E. O. Stejskal. *J. Am. Chem. Soc.* 98 (1976), 1031–1032.

[19] R. Zhang, K. H. Mroue, and A. Ramamoorthy. *Acc. Chem. Res.* 50 (2017), 1105–1113.

[20] A. L. Bloom and J. N. Shoolery. *Phys. Rev.* 97 (1955), 1261–1265.

[21] B. M. Fung, A. K. Khitrin, and K. Ermolaev. *J. Magn. Reson.* 142 (2000), 97–101.

[22] R. S. Thakur, N. D. Kurur, and P. Madhu. *Chem. Phys. Lett.* 426 (2006), 459–463.

[23] S. R. Hartmann and E. L. Hahn. *Phys. Rev.* 128 (1962), 2042–2053.

[24] E. Stejskal, J. Schaefer, and J. Waugh. *J. Magn. Reson.* 28 (1977), 105–112.

[25] G. Metz, X. Wu, and S. Smith. *J. Magn. Reson., Ser. A* 110 (1994), 219–227.

[26] A. W. Overhauser. *Phys. Rev.* 92 (1953), 411–415.

[27] T. R. Carver and C. P. Slichter. *Phys. Rev.* 92 (1953), 212–213.

[28] M. Rosay, L. Tometich, S. Pawsey, R. Bader, R. Schauwecker, M. Blank, P. M. Borchard, S. R. Cauffman, K. L. Felch, R. T. Weber, R. J. Temkin, R. G. Griffin, and W. E. Maas. *Phys. Chem. Chem. Phys.* 12 (2010), 5850–5860.

[29] M. Rosay, M. Blank, and F. Engelke. *J. Magn. Reson.* 264 (2016), 88–98.

[30] L. R. Becerra, G. J. Gerfen, R. J. Temkin, D. J. Singel, and R. G. Griffin. *Phys. Rev. Lett.* 71 (1993), 3561–3564.

[31] V. Bajaj, C. Farrar, M. Hornstein, I. Mastovsky, J. Vieregg, J. Bryant, B. Eléna, K. Kreischer, R. Temkin, and R. Griffin. *J. Magn. Reson.* 160 (2003), 85–90.

[32] V. S. Bajaj, M. K. Hornstein, K. E. Kreischer, J. R. Sirigiri, P. P. Woskov, M. L. Mak-Jurkauskas, J. Herzfeld, R. J. Temkin, and R. G. Griffin. *J. Magn. Reson.* 189 (2007), 251–279.

[33] K.-N. Hu, H.-h. Yu, T. M. Swager, and R. G. Griffin. *J. Am. Chem. Soc.* 126 (2004), 10844–10845.

[34] C. Song, K.-N. Hu, C.-G. Joo, T. M. Swager, and R. G. Griffin. *J. Am. Chem. Soc.* 128 (2006), 11385–11390.

[35] D. Lee, S. Hediger, and G. De Paëpe. *Solid State Nucl. Magn. Reson.* 66 (2015), 6–20.

[36] T. Kobayashi, F. A. Perras, I. I. Slowing, A. D. Sadow, and M. Pruski. *ACS Catal.* 5 (2015), 7055–7062.

[37] A. S. Lilly Thankamony, J. J. Wittmann, M. Kaushik, and B. Corzilius. *Prog. Nucl. Magn. Reson. Spectrosc.* 102-103 (2017), 120–195.

[38] H. Takahashi, D. Lee, L. Dubois, M. Bardet, S. Hediger, and G. De Paëpe. *Angew. Chem., Int. Ed.* 51 (2012), 11766–11769.

[39] A. J. Rossini, A. Zagdoun, F. Hegner, M. Schwarzwälder, D. Gajan, C. Copéret, A. Lesage, and L. Emsley. *J. Am. Chem. Soc.* 134 (2012), 16899–16908.

[40] H. Takahashi, B. Viverge, D. Lee, P. Rannou, and G. De Paëpe. *Angew. Chem., Int. Ed.* 52 (2013), 6979–6982.

[41] G. Mollica, M. Dekhil, F. Ziarelli, P. Thureau, and S. Viel. *Angew. Chem., Int. Ed.* 54 (2015), 6028–6031.

[42] A. V. Kessenikh, V. I. Luschikov, A. A. Manenkov, and Y. V. Taran. *Sov. Phys.-Solid State* 5 (1963), 321–329.

[43] C. F. Hwang and D. A. Hill. *Phys. Rev. Lett.* 18 (1967), 110–112.

[44] A. Abragam and W. Proctor. *Comptes Rendus Hebd. des Seances l'Academie des Sci.* 246 (1958), 2253–2256.

[45] T. V. Can, M. A. Caporini, F. Mentink-Vigier, B. Corzilius, J. J. Walish, M. Rosay, W. E. Maas, M. Baldus, S. Vega, T. M. Swager, and R. G. Griffin. *J. Chem. Phys.* 141 (2014), 064202.

[46] A. B. Barnes, G. De Paëpe, P. C. A. Van Der Wel, K.-N. Hu, C. G. Joo, V. S. Bajaj, M. L. Mak-Jurkauskas, J. R. Sirigiri, J. Herzfeld, R. J. Temkin, and R. G. Griffin. *Appl. Magn. Reson.* 34 (2008), 237–263.

[47] K. R. Thurber and R. Tycko. *J. Chem. Phys.* 137 (2012), 084508.

[48] F. Mentink-Vigier, U. Akbey, Y. Hovav, S. Vega, H. Oschkinat, and A. Feintuch. *J. Magn. Reson.* 224 (2012), 13–21.

[49] T. Can, Q. Ni, and R. Griffin. *J. Magn. Reson.* 253 (2015), 23–35.

[50] F. Mentink-Vigier, S. Paul, D. Lee, A. Feintuch, S. Hediger, S. Vega, and G. De Paëpe. *Phys. Chem. Chem. Phys.* 17 (2015), 21824–21836.

[51] K. R. Thurber and R. Tycko. *J. Chem. Phys.* 140 (2014), 184201.

[52] E. Bouleau, P. Saint-Bonnet, F. Mentink-Vigier, H. Takahashi, J.-F. Jacquot, M. Bardet, F. Aussenac, A. Purea, F. Engelke, S. Hediger, D. Lee, and G. De Paëpe. *Chem. Sci.* 6 (2015), 6806–6812.

[53] C. Sauvée, M. Rosay, G. Casano, F. Aussenac, R. T. Weber, O. Ouari, and P. Tordo. *Angew. Chem., Int. Ed.* 52 (2013), 10858–10861.

[54] A. Zagdoun, G. Casano, O. Ouari, M. Schwarzwälder, A. J. Rossini, F. Aussenac, M. Yulikov, G. Jeschke, C. Copéret, A. Lesage, P. Tordo, and L. Emsley. *J. Am. Chem. Soc.* 135 (2013), 12790–12797.

[55] A. Zagdoun, G. Casano, O. Ouari, G. Lapadula, A. J. Rossini, M. Lelli, M. Baffert, D. Gajan, L. Veyre, W. E. Maas, M. Rosay, R. T. Weber, C. Thieuleux, C. Coperet, A. Lesage, P. Tordo, and L. Emsley. *J. Am. Chem. Soc.* 134 (2012), 2284–2291.

[56] S. Chaudhari, P. Berruyer, D. Gajan, C. Reiter, F. Engelke, D. Silverio, C. Copéret, M. Lelli, A. Lesage, and L. Emsley. *Phys. Chem. Chem. Phys.* 18 (2016), 10616–10622.

[57] G. Mathies, M. A. Caporini, V. K. Michaelis, Y. Liu, K.-N. Hu, D. Mance, J. L. Zweier, M. Rosay, M. Baldus, and R. G. Griffin. *Angew. Chem., Int. Ed.* 54 (2015), 11770–11774.

[58] F. Mentink-Vigier, S. Vega, and G. De Paëpe. *Phys. Chem. Chem. Phys.* 19 (2017), 3506–3522.

[59] D. A. Hall, D. C. Maus, G. J. Gerfen, S. J. Inati, L. R. Becerra, F. W. Dahlquist, and R. G. Griffin. *Science* 276 (1997), 930–932.

[60] A. Lesage, M. Lelli, D. Gajan, M. A. Caporini, V. Vitzthum, P. Miéville, J. Alauzun, A. Roussey, C. Thieuleux, A. Mehdi, G. Bodenhausen, C. Copéret, and L. Emsley. *J. Am. Chem. Soc.* 132 (2010), 15459–15461.

[61] H. Takahashi, S. Hediger, and G. De Paepe. *Chem. Commun.* 49 (2013), 9479–81.

[62] A. H. Linden, W. T. Franks, Ü. Akbey, S. Lange, B.-J. van Rossum, and H. Oschkinat. *J. Biomol. NMR* 51 (2011), 283–292.

[63] R. K. Harris, R. E. Wasylishen, and M. J. Duer, eds. *NMR Crystallography.* Chichester: WILEY, 2009.

[64] C. Martineau, J. Senker, and F. Taulelle. "NMR Crystallography". *Annu. Reports NMR Spectrosc.* Vol. 82. 2014, pp. 1–57.

[65] D. L. Bryce. *IUCrJ* 4 (2017), 350–359.

[66] S. E. Ashbrook and D. McKay. *Chem. Commun.* 52 (2016), 7186–7204.

[67] C. Bonhomme, C. Gervais, F. Babonneau, C. Coelho, F. Pourpoint, T. Azaïs, S. E. Ashbrook, J. M. Griffin, J. R. Yates, F. Mauri, and C. J. Pickard. *Chem. Rev.* 112 (2012), 5733–79.

[68] T. Charpentier. *Solid State Nucl. Magn. Reson.* 40 (2011), 1–20.

[69] A. Lesage, M. Bardet, and L. Emsley. *J. Am. Chem. Soc.* 121 (1999), 10987–10993.

[70] G. De Paëpe. *Annu. Rev. Phys. Chem.* 63 (2012), 661–684.

[71] N. C. Nielsen, L. A. Strassø, and A. B. Nielsen. *Top. Curr. Chem.* 306 (2012), 1–45.

[72] C. J. Pickard and F. Mauri. *Phys. Rev. B* 63 (2001), 245101–245113.

[73] G. M. Day. *Crystallogr. Rev.* 17 (2011), 3–52.

[74] S. L. Price. *Chem. Soc. Rev.* 43 (2014), 2098–2111.

[75] M. Baias, C. M. Widdifield, J.-N. Dumez, H. P. G. Thompson, T. G. Cooper, E. Salager, S. Bassil, R. S. Stein, A. Lesage, G. M. Day, and L. Emsley. *Phys. Chem. Chem. Phys.* 15 (2013), 8069–8080.

[76] M. Baias, J.-N. Dumez, P. H. Svensson, S. Schantz, G. M. Day, and L. Emsley. *J. Am. Chem. Soc.* 135 (2013), 17501–17507.

[77] P. R. Costa. “Spins, Peptides, and Alzheimer’s Disease: Solid-State Nuclear Magnetic Resonance Investigations of Amyloid Peptide Conformation”. PhD thesis. Massachusetts Institute of Technology, 1996.

[78] P. E. Kristiansen, M. Carravetta, W. C. Lai, and M. H. Levitt. *Chem. Phys. Lett.* 390 (2004), 1–7.

[79] A. Lesage, P. Charmont, S. Steuernagel, and L. Emsley. *J. Am. Chem. Soc.* 122 (2000), 9739–9744.

[80] A. Lesage. *Phys. Chem. Chem. Phys.* 11 (2009), 6876–6891.

[81] P. K. Madhu. *Solid State Nucl. Magn. Reson.* 35 (2009), 2–11.

[82] R. K. Harris. *J. Pharm. Pharmacol.* 59 (2007), 225–239.

[83] I. Manet, L. Francini, S. Masiero, S. Pieraccini, G. P. Spada, and G. Gottarelli. *Helv. Chim. Acta* 84 (2001), 2096–2107.

[84] J. T. Davis. *Angew. Chem., Int. Ed.* 43 (2004), 668–698.

[85] J. T. Davis and G. P. Spada. *Chem. Soc. Rev.* 36 (2007), 296–313.

[86] S. Lena, S. Masiero, S. Pieraccini, and G. P. Spada. *Chemistry* 15 (2009), 7792–7806.

[87] F. Pu, L. Wu, X. Ran, J. Ren, and X. Qu. *Angew. Chem., Int. Ed.* 54 (2015), 892–896.

[88] T. Giorgi, F. Grepioni, I. Manet, P. Mariani, S. Masiero, E. Mezzina, S. Pieraccini, L. Saturni, G. P. Spada, and G. Gottarelli. *Chem. - Eur. J.* 8 (2002), 2143–2152.

[89] T. N. Pham, S. Masiero, G. Gottarelli, and S. P. Brown. *J. Am. Chem. Soc.* 127 (2005), 16018–16019.

[90] A. L. Webber, S. Masiero, S. Pieraccini, J. C. Burley, A. S. Tatton, D. Iuga, T. N. Pham, G. P. Spada, and S. P. Brown. *J. Am. Chem. Soc.* 133 (2011), 19777–19795.

[91] P. E. Kristiansen, M. Carravetta, J. D. van Beek, W. C. Lai, and M. H. Levitt. *J. Chem. Phys.* 124 (2006), 234510–234519.

[92] J. Schaefer, R. McKay, and E. Stejskal. *J. Magn. Reson.* 34 (1979), 443–447.

[93] M. Baldus, D. Geurts, S. Hediger, and B. Meier. *J. Magn. Reson., Ser. A* 118 (1996), 140–144.

[94] S. Hediger, B. Meier, and R. Ernst. *Chem. Phys. Lett.* 240 (1995), 449–456.

[95] D. Marion, M. Ikura, R. Tschudin, and A. Bax. *J. Magn. Reson.* 85 (1989), 393–399.

[96] M. Lee and W. I. Goldburg. *Phys. Rev.* 140 (1965), A1261–A1271.

[97] L. Adler-Abramovich, D. Aronov, P. Beker, M. Yevnin, S. Stempler, L. Buzhansky, G. Rosenman, and E. Gazit. *Nat. Nanotechnol.* 4 (2009), 849–54.

[98] M. Gdaniec and B. Liberek. *Acta Crystallogr. Sect. C* 42 (1986), 1343–1345.

[99] C. Ye, R. Fu, J. Hu, L. Hou, and S. Ding. *Magn. Reson. Chem.* 31 (1993), 699–704.

[100] T. Karlsson, J. M. Popham, J. R. Long, N. Oyler, and G. P. Drobny. *J. Am. Chem. Soc.* 125 (2003), 7394–7407.

[101] G. Teymoori, B. Pahari, B. Stevensson, and M. Edén. *Chem. Phys. Lett.* 547 (2012), 103–109.

[102] G. Teymoori, B. Pahari, and M. Edén. *J. Magn. Reson.* 261 (2015), 205–220.

[103] A. W. Hing, S. Vega, and J. Schaefer. *J. Magn. Reson.* 96 (1992), 205–209.

[104] M. H. Levitt. *Encycl. Nucl. Magn. Reson.* 9 (2002), 165–196.

[105] T. Gullion and J. Schaefer. *J. Magn. Reson.* 81 (1989), 196–200.

[106] T. Gullion and J. Schaefer. *Adv. Magn. Opt. Reson.* 13 (1989), 57–83.

[107] J. Schaefer. "REDOR and TEDOR". *Encycl. Magn. Reson.* Chichester, UK: John Wiley & Sons, Ltd, 2007.

[108] C. P. Jaroniec. "Dipolar Recoupling: Heteronuclear". *Encycl. Magn. Reson.* Chichester, UK: John Wiley & Sons, Ltd, 2009.

[109] T. Gullion. "Recent Applications of REDOR to Biological Problems". *Annu. Reports NMR Spectrosc.* Vol. 65. Academic Press, 2009, pp. 111–137.

[110] G. A. Morris and R. Freeman. *J. Am. Chem. Soc.* 101 (1979), 760–762.

[111] J. S. Lee, I. Yoon, J. Kim, H. Ihee, B. Kim, and C. B. Park. *Angew. Chem., Int. Ed.* 50 (2011), 1164–1167.

[112] M. Veshtort and R. G. Griffin. *J. Magn. Reson.* 178 (2006), 248–282.

[113] D. H. Brouwer, P. E. Kristiansen, C. A. Fyfe, and M. H. Levitt. *J. Am. Chem. Soc.* 127 (2005), 542–543.

[114] D. H. Brouwer, R. J. Darton, R. E. Morris, and M. H. Levitt. *J. Am. Chem. Soc.* 127 (2005), 10365–10370.

[115] P. Giannozzi, S. Baroni, N. Bonini, M. Calandra, R. Car, C. Cavazzoni, D. Ceresoli, G. L. Chiarotti, M. Cococcioni, I. Dabo, A. Dal Corso, S. de Gironcoli, S. Fabris, G. Fratesi, R. Gebauer, U. Gerstmann, C. Gougoussis, A. Kokalj, M. Lazzeri, L. Martin-Samos, N. Marzari, F. Mauri, R. Mazzarello, S. Paolini, A. Pasquarello, L. Paulatto, C. Sbraccia, S. Scandolo, G. Sclauzero, A. P. Seitsonen, A. Smogunov, P. Umari, and R. M. Wentzcovitch. *J. Phys. Condens. Matter* 21 (2009), 395502.

[116] B.-Q. Sun, P. R. Costa, D. Kocisko, P. T. Lansbury, and R. G. Griffin. *J. Chem. Phys.* 102 (1995), 702–707.

[117] A. Naito, S. Ganapathy, and C. McDowell. *J. Magn. Reson.* 48 (1982), 367–381.

[118] R. K. Harris and A. C. Olivieri. *Prog. Nucl. Magn. Reson. Spectrosc.* 24 (1992), 435–456.

[119] G. D. Scholes, G. R. Fleming, A. Olaya-Castro, and R. van Grondelle. *Nat. Chem.* 3 (2011), 763–774.

[120] A. Facchetti. *Chem. Mater.* 23 (2011), 733–758.

[121] H. Dong, H. Zhu, Q. Meng, X. Gong, and W. Hu. *Chem. Soc. Rev.* 41 (2012), 1754–808.

[122] C. Wang, H. Dong, W. Hu, Y. Liu, and D. Zhu. *Chem. Rev.* 112 (2012), 2208–2267.

[123] S. P. Brown. *Solid State Nucl. Magn. Reson.* 41 (2012), 1–27.

[124] M. R. Hansen, R. Graf, and H. W. Spiess. *Chem. Rev.* 116 (2016), 1272–1308.

[125] L. B. Krivdin and G. A. Kalabin. *Prog. Nucl. Magn. Reson. Spectrosc.* 21 (1989), 293–448.

[126] R. Romano, D. Paris, F. Acernese, F. Barone, and A. Motta. *J. Magn. Reson.* 192 (2008), 294–301.

[127] C. P. Jaroniec, C. Filip, and R. G. Griffin. *J. Am. Chem. Soc.* 124 (2002), 10728–10742.

[128] T. Gullion, D. B. Baker, and M. S. Conradi. *J. Magn. Reson.* 89 (1990), 479–484.

[129] H. Saitô, I. Ando, and A. Ramamoorthy. *Prog. Nucl. Magn. Reson. Spectrosc.* 57 (2010), 181–228.

[130] K. Mueller. *J. Magn. Reson., Ser. A* 113 (1995), 81–93.

[131] D. Lee, E. Bouleau, P. Saint-Bonnet, S. Hediger, and G. D. Paëpe. *J. Magn. Reson.* 264 (2016), 116–124.

[132] H. Geen and R. Freeman. *J. Magn. Reson.* 93 (1991), 93–141.

[133] F. Delaglio, S. Grzesiek, G. Vuister, G. Zhu, J. Pfeifer, and A. Bax. *J. Biomol. NMR* 6 (1995), 277–293.

[134] N. Troullier and J. L. Martins. *Phys. Rev. B* 43 (1991), 1993–2006.

[135] J. P. Perdew, K. Burke, and M. Ernzerhof. *Phys. Rev. Lett.* 77 (1996), 3865–3868.

[136] H. J. Monkhorst and J. D. Pack. *Phys. Rev. B* 13 (1976), 5188–5192.

[137] J. W. Ponder and F. M. Richards. *J. Comput. Chem.* 8 (1987), 1016–1024.

[138] F. Neese. *Wiley Interdiscip. Rev. Comput. Mol. Sci.* 2 (2012), 73–78.

[139] C. J. E. Kempster and H. Lipson. *Acta Crystallogr. Sect. B* 28 (1972), 3674–3674.

[140] C. D. Schwieters, J. J. Kuszewski, N. Tjandra, and G. Marius Clore. *J. Magn. Reson.* 160 (2003), 65–73.

[141] C. D. Schwieters, J. J. Kuszewski, and G. Marius Clore. *Prog. Nucl. Magn. Reson. Spectrosc.* 48 (2006), 47–62.

[142] B. Elena, G. Pintacuda, N. Mifsud, and L. Emsley. *J. Am. Chem. Soc.* 128 (2006), 9555–9560.

[143] E. Salager, R. S. Stein, C. J. Pickard, B. Elena, and L. Emsley. *Phys. Chem. Chem. Phys.* 11 (2009), 2610–2621.

[144] J. Wang, P. Cieplak, and P. A. Kollman. *J. Comput. Chem.* 21 (2000), 1049–1074.

[145] A. Schäfer, H. Horn, and R. Ahlrichs. *J. Chem. Phys.* 97 (1992), 2571–2577.

[146] J. P. Perdew. *Phys. Rev. B* 33 (1986), 8822–8824.

[147] A. D. Becke. *Phys. Rev. A* 38 (1988), 3098–3100.

[148] F. Weigend and R. Ahlrichs. *Phys. Chem. Chem. Phys.* 7 (2005), 3297–3305.

[149] C. Lee, W. Yang, and R. G. Parr. *Phys. Rev. B* 37 (1988), 785–789.

[150] A. D. Becke. *J. Chem. Phys.* 98 (1993), 5648–5653.

[151] P. J. Stephens, F. J. Devlin, C. F. Chabalowski, and M. J. Frisch. *J. Phys. Chem.* 98 (1994), 11623–11627.

[152] S. Grimme, J. Antony, S. Ehrlich, and H. Krieg. *J. Chem. Phys.* 132 (2010), 154104–154119.

[153] S. Grimme, S. Ehrlich, and L. Goerigk. *J. Comput. Chem.* 32 (2011), 1456–1465.

[154] M. Edén and M. H. Levitt. *J. Chem. Phys.* 111 (1999), 1511–1519.

[155] M. Carravetta, M. Edén, X. Zhao, A. Brinkmann, and M. H. Levitt. *Chem. Phys. Lett.* 321 (2000), 205–215.

[156] N. C. Nielsen, H. Bildsøe, H. J. Jakobsen, and M. H. Levitt. *J. Chem. Phys.* 101 (1994), 1805–1812.

[157] Y. Lee, N. Kurur, M. Helmle, O. Johannessen, N. Nielsen, and M. Levitt. *Chem. Phys. Lett.* 242 (1995), 304–309.

[158] M. Hohwy, H. J. Jakobsen, M. Edén, M. H. Levitt, and N. C. Nielsen. *J. Chem. Phys.* 108 (1998), 2686–2694.

[159] M. Hohwy, C. M. Rienstra, C. P. Jaroniec, and R. G. Griffin. *J. Chem. Phys.* 110 (1999), 7983–7992.

[160] G. De Paëpe, J. R. Lewandowski, and R. G. Griffin. *J. Chem. Phys.* 128 (2008), 124503–124526.

[161] M. Edén. “Advances in Symmetry-Based Pulse Sequences in Magic-Angle Spinning Solid-State NMR”. *eMagRes.* Chichester, UK: John Wiley & Sons, Ltd, 2013, pp. 351–364.

[162] D. H. Brouwer, S. Cadars, J. Eckert, Z. Liu, O. Terasaki, and B. F. Chmelka. *J. Am. Chem. Soc.* 135 (2013), 5641–5655.

[163] S. Cadars, M. Allix, D. H. Brouwer, R. Shayib, M. Suchomel, M. N. Garaga, A. Rakhmatullin, A. W. Burton, S. I. Zones, D. Massiot, and B. F. Chmelka. *Chem. Mater.* 26 (2014), 6994–7008.

[164] H. Geen, J. Titman, J. Gottwald, and H. Spiess. *J. Magn. Reson., Ser. A* 114 (1995), 264–267.

[165] U. Friedrich, I. Schnell, S. P. Brown, A. Lupulescu, D. E. Demco, and H. W. Spiess. *Mol. Phys.* 95 (1998), 1209–1227.

[166] T. Karlsson, A. Brinkmann, P. Verdegem, J. Lugtenburg, and M. Levitt. *Solid State Nucl. Magn. Reson.* 14 (1999), 43–58.

[167] A. Brinkmann, M. Edén, and M. H. Levitt. *J. Chem. Phys.* 112 (2000), 8539–8554.

[168] A. Brinkmann. "Dipolar recoupling in Magic-Angle-Spinning Nuclear Magnetic Resonance". PhD thesis. Stockholm University, 2001.

[169] M. O. Boles and R. J. Girven. *Acta Crystallogr. Sect. B* 32 (1976), 2279–2284.

[170] O. N. Antzutkin, Y. K. Lee, and M. H. Levitt. *J. Magn. Reson.* 135 (1998), 144–155.

[171] V. S. Bajaj, P. C. van der Wel, and R. G. Griffin. *J. Am. Chem. Soc.* 131 (2009), 118–128.

[172] A. Wokaun and R. Ernst. *Chem. Phys. Lett.* 52 (1977), 407–412.

[173] S. Vega. *J. Chem. Phys.* 68 (1978), 5518–5527.

[174] P. E. Pfeffer, K. B. Hicks, M. H. Frey, S. J. Opella, and W. L. Earl. *J. Carbohydr. Chem.* 3 (1984), 197–217.